UNIVERSITÀ DEGLI STUDI DI PADOVA

Dipartimento di Fisica e Astronomia "Galileo Galilei"

Master Degree in Physics

Final Dissertation

Experimental investigation of the ^{7}Li Cosmological Problem by means of the Trojan Horse Method applied to the ^{7}Be(n,α)^{4}He reaction

Thesis supervisor

Prof. Marco Mazzocco

Thesis co-supervisor

Prof. Livio Lamia

Candidate

Andrea Lagni

Academic Year 2020/2021

To my mother Daniela,
to my father Alberto,
to my sister Anna,
to my brother Davide
and to all those who love me.

Contents

Foreword

With the term "^{7}Li Cosmological Problem" we refer to the discrepancy between the primordial abundance of ^{7}Li, observed in metal-poor halo stars, and the abundance predicted by the Big Bang Nucleosynthesis (BBN) [1; 2].
The cosmological theory of the Big Bang is so far supported by three observational evidences: the Hubble expansion of the universe, the presence of the Cosmic Microwave Background (CMB) radiation and the primordial or BBN. Of the three, the BBN gives information about the universe down to the earliest times, from a fraction of a second to hundreds of seconds, in an radiation-dominated epoch [3; 4; 5; 6]. During this period, large amounts of light elements as D, ^{3}He, ^{4}He and ^{7}Li were produced and their primordial abundances are today investigated in different astrophysical scenarios. By varying only the baryon-to-photon ratio $\eta = \frac{nb}{n\gamma}$ parameter, the theory of BBN allows us to predict these primordial abundances once the neutron life time (τ_n), the neutrino families (N_η), and the nuclear reaction network have been fixed. The comparison between the BBN primeval abundances and the observed ones might allow the determination the cosmic baryonic density, which is very important for the chemical evolution of the universe. However, while there is a substantial agreement between the predicted and observed primordial abundances for ^{2}H and ^{4}He, there is a large discrepancy regarding the ^{7}Li primordial abundance. Lithium abundances are derived from metal-poor halo-star observations; an averaged value of $(\mathrm{Li/H})_{obs} = 1.58\times10^{-10}$ [7; 8] is currently accepted. The comparison between the $(\mathrm{Li/H})_{obs}$ with the most recent inferred lithium abundances $(\mathrm{Li/H})_{BBN} \sim 5.623\times 10^{10}$ [9; 10] shows a discrepancy of a factor ~ 3.

The controversy between the observed $(\mathrm{Li/H})_{obs}$ and the inferred primordial $(\mathrm{Li/H})_{BBN}$ lithium abundances has not been explained yet and represents one of the most critical and challenging open problems for cosmology, astrophysics and nuclear astrophysics. ^{7}Li is mainly produced from ^{7}Be that undergoes the electron capture process: $e^- + {}^7\mathrm{Be} \rightarrow {}^7\mathrm{Li} + \eta_e$. We thus expect the primordial ^{7}Li abundance to be essentially determined by the ^{7}Be production and destruction rates at the temperatures T = 20-70 keV when ^{7}Be is synthesized in the early Universe. The dominant ^{7}Be production mechanism is through the capture reaction ^{3}He(α,γ)^{7}Be [11; 12]. As a consequence, a relevant reduction of the ^{7}Li primordial abundance can occur only if a large increase of the ^{7}Be destruction rate is allowed. To explore this possibility, several measurements have been recently performed for charged particle induced reactions on ^{7}Be The results ruled out the possibility that proton-, deuteron-, ^{3}He- and ^{4}He-induced reactions could be responsible for the destruction of ^{7}Be during BBN.

At the same time, additionally to charged particle induced reactions, the unstable ^{7}Be isotope is destroyed at BBN temperatures mainly by neutron induced reactions via the two channels: ^{7}Be(n,p)^{7}Li [13; 14; 15; 16] and ^{7}Be(n,α)^{4}He. The ^{7}Be(n,α)^{4}He reaction, contrary to the (n,p) process, has not been measured in the energy range relevant for primordial nucleosynthesis. The only available experimental information was derived by P. Bassi et al. at ISPRA in 1963 [17] by using thermal neutrons, leading to an upper limit of 0.1 mb. Additional cross section values can be calculated from the ^{4}He(α,n)^{7}Be

measurements of [18; 19], although they considered ^{7}Be-n centre of mass energies greater than 600 keV, thus leaving great uncertainties at the BBN energy range.

The reaction ^{7}Be(n,α)^{4}He cannot proceed via an s-wave collision, and thus is suppressed by centrifugal barrier penetration. It is, however, the second most important contribution to the ^{7}Be destruction rate, accounting for $\sim$ 2.5% of the total cross section [20]. At present, due to the large uncertainty assigned, it provides one of the dominant contributions to the theoretical errors in the ^{7}Li abundance evaluations [21]. Even a low accuracy new measurement for the ^{7}Be(n,α)^{4}He cross section would reduce the present uncertainty of the estimated rate, thus permitting on one hand to exclude the possibility that ^{7}Be(n,α)^{4}He is underestimated by the large factor required to solve the ^{7}Li cosmological problem and, on the other hand, to reduce its contribution to the primordial ^{7}Li error budget.

An additional complication in the business of the ^{7}Be(n,α)^{4}He reaction is that it involves the interaction of neutrons with a radioactive beam at the same time. Studying interactions of radioactive ions with neutrons is particularly demanding from an experimental point-of-view and has been performed only in a few cases (Novae stars, Cosmic Rays astrophysics). In the present work, the case of the ^{7}Be destruction induced by the (n,α) reaction is investigated at the energies typical of the primordial nucleosynthesis by means of the Trojan Horse Method applied to the ^{2}H(^{7}Be,$\alpha\alpha$)p QF reaction. The ^{7}Be(n,α)He cross-section has been measured in a single experiment from $\sim$ 2 MeV down to cosmological energies.

CHAPTER 1

Introduction

1.1 Big Bang Nucleosynthesis

The process of primordial nucleosynthesis, along with the cosmic microwave background radiation, is one of the fundamental confirmations to the theory of the Big Bang. The term primordial nucleosynthesis (BBN, i.e. Big Bang Nucleosynthesis) [22; 23] describes the evolution of the universe from a few instants after the Big Bang, with the formation of the first light nuclei, mainly D, ^{4}He and ^{7}Li.

At the beginning of the primordial nucleosynthesis, every elementary particle present in the cosmic nest is immersed in a bath of photons, in perfect thermodynamic equilibrium. In these conditions, if the temperature of the fluid is greater than $kT = mc^2$, collisions between photons, or between photons and particles, can form a particle-antiparticle pair, while a particle-antiparticle pair can annihilate forming an energetic photon. In a situation of thermodynamic equilibrium, the processes of creation and destruction compensate each other. After $t \sim 10^{-5}$ s, quarks are conjugated into hadrons (neutrons, protons and pions) in the so-called hadronic era, while after $t \sim 10^{-4}$, during the leptonic era, light particles are in perfect creation and annihilation equilibrium with photons, and heavy particles are kept in equilibrium by the following reactions mediated by weak interactions:

$$\begin{aligned} n + \nu_e &\leftrightarrow p + e^- \\ n + e^+ &\leftrightarrow p + \bar{\nu}_e \\ n &\leftrightarrow p + e^- + \bar{\nu}_e \end{aligned} \tag{1.1}$$

As temperature decreases, due to the mass difference between neutrons and protons, the equilibrium shifts progressively in favor of protons following Boltzmann law [24]:

$$\frac{N_n}{N_p} = \exp \frac{m_n - m_e}{kT} \tag{1.2}$$

When the temperature drops below 10^{10} K, about one second after the Big Bang, photons are no longer energetic enough to create matter, which then annihilates to almost total exhaustion. At the end of the leptonic epoch, when most of electrons and anti-electrons have annihilated, the above mentioned reactions can no longer occur. As a consequence, the ratio of neutrons to protons freezes at the value of 0.88 [22]. The only reaction that can still take place is $n + p \leftrightarrow e^- + \bar{\nu}_e$. This reaction would lead

to complete destruction of neutrons, but they remain incorporated in the light nuclei that begin to form at a temperature of $T = 10^9$ K: most of them are ^{4}He, but also D, ^{3}He, and ^{7}Li. In general, heavier elements are not formed because nuclei of atomic masses 5 and 8 are unstable and reactions that could create heavier nuclei are extremely rare.

The first nuclear reaction to occur ($T \sim 2.5 \cdot 10^{10}$ K) is the one that produces the deuterium: p(n,γ)d. This reaction is hindered by photodissociation by photons with energy higher than $E > 2.22$ MeV, i.e. the deuterium binding energy. Only at lower temperatures ($T \sim 10^9$ K) the deuterium is produced in sufficient quantities to allow the nucleosynthetic chain to proceed according to the reactions:

$$\begin{gathered} d + n \leftrightarrow^3 H + \gamma \\ d + p \leftrightarrow^3 He + \gamma \\ d + d \leftrightarrow^3 He + n \\ d + d \leftrightarrow^3 H + p \\ {}^3H + p \leftrightarrow^4 He + \gamma \\ {}^3He + n \leftrightarrow^4 He + \gamma \end{gathered} \tag{1.3}$$

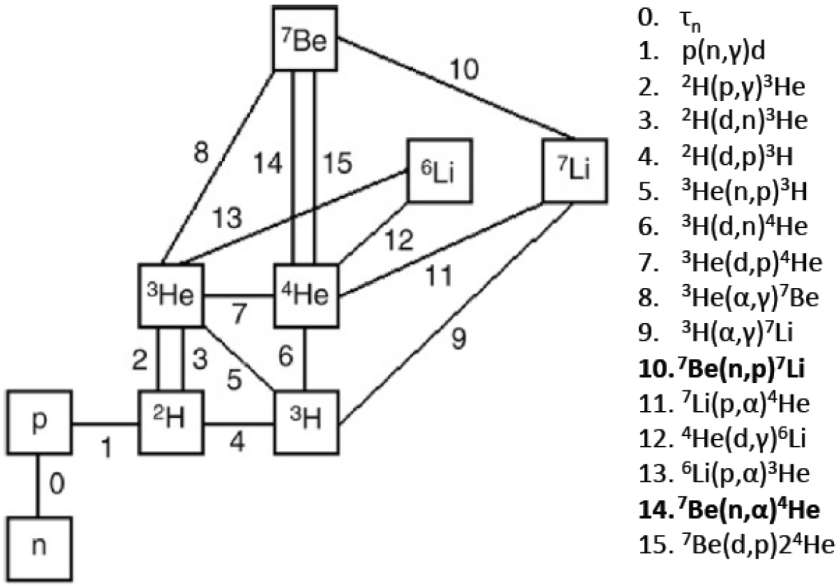

Figure 1.1: The BBN reaction network for BBN. Figure taken from Nollett and Burles [25].

1.2 Matter density parameter

The main outcomes of the BBN are essentially two:

- it succeeds in placing limits on the matter density parameter, Ω_b,
- it succeeds in explaining the observed abundance of ^{4}He in the universe [26].

Once the neutron life time (τ_n), the neutrino families (N_η), and the nuclear reaction network have been fixed [22; 27] the formation of light nuclei depends crucially on the baryon-to-photon ratio, and in particular on the matter density parameter. In fact we can rewrite η as:

$$\eta = \frac{N_b}{N_\gamma} = 2.74 \cdot 10^{-8} \Omega_b h^2, \tag{1.4}$$

where Ω_b is the matter density parameter.

The coefficient η represents the main free parameter in the theory of the BBN [28], but if we combine it with the precision measurements of the missions WMAP and Planck, we can constrain it, thus finding accurate predictions about the abundance[1] of light elements from the theory [4]. As can be seen from Fig. 1.2, the behaviour of η for the various elements formed during the primordial nucleosynthesis are different: while the abundance of helium does not depend in a significant way on the density of plasma at the time the of nucleosynthesis [22], both deuterium and lithium show a very strong dependence.

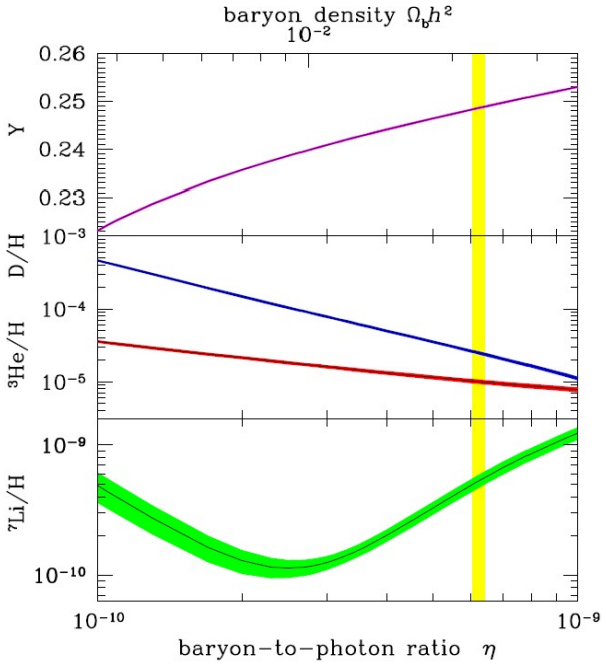

Figure 1.2: Predictions for the light nuclei abundances from BBN theory. Y represents the abundance of ^{4}He relative to hydrogen. The width of the curves represents 1σ-uncertainties, while the yellow vertical band reproduces the η parameter as determined by WMAP. Figure taken from [4].

If the plasma density is higher, in fact, nuclear reactions proceed with more efficiency, converting all neutrons into deuterons and then all deuterons into helium. A low plasma density, on the other hand, would lead to important residues of deuterium and ^{4}He, which could not interact and thus would remain intact from that epoch. The measurement of the abundance of these elements in astronomical sites as primordial as possible, and therefore uncontaminated by stellar activity, leads to an estimate of the density of baryons present at the time of primordial nucleosynthesis, and therefore also of the average total density of the universe today. In fact, placing ourselves in a reference system with the expansion of the universe, the density of baryonic matter is conserved.

Regarding the abundance of ^{3}He [26; 29; 30], there are no convincing observations of primordial $\frac{^3He}{H}$. All observations of ^{3}He are in fact made at near-solar metallicity, and thus are not primordial measurements. Since $\frac{^3He}{H}$ increases greatly over time due to stellar nucleosynthesis, and all measurements of $\frac{^3He}{H}$ are made within the galactic environment, they do not provide solid constraints on the measurement of the density parameter. The deuterium measurement, on the other hand, is particularly constraining, as $\frac{D}{H} =\propto \rho_b^{-1.6}$. The abundance of deuterium closest to the primordial abundance can be determined from the observation of cosmological clouds on the line of sight of distant quasars at high red-shift [10]. Deuterium is, in turn, only destroyed inside stars, thus its abundance is due only

[1]The abundance ratio is the common logarithm of the ratio of a star's iron abundance compared to that of the Sun and is calculated in this way:

$$\left[\frac{Fe}{H}\right] = \log_{10}\left(\frac{N_{Fe}}{N_H}\right) - \log_{10}\left(\frac{N_{Fe}}{N_H}\right)_{Sun} \tag{1.5}$$

where N_{Fe} and N_H are the number of iron and hydrogen atoms per unit of volume respectively.

to primordial ashes. This leads to a density parameter [31]:

$$\Omega_b h^2 = 0.02273 \pm 0.00062 \tag{1.6}$$

Where h is related to the Hubble constant. Thanks to the theory of primordial nucleosynthesis and the measurement of the deuterium abundance, it is possible to obtain essential information which, together with other constraints and parameters, makes it possible to deduce the total amount of baryonic matter in the universe.

1.2.1 The role of the Cosmic Microwave Background

Theorized in 1948 by George Gamow as a consequence of the decoupling of matter from radiation, the CMB represented a decisive observational test for the confirmation of the Big Bang theory. The actual discovery was made in 1965 by Arno Penzias and Robert Wilson [32]. The CMB represents a direct channel of information about the early Universe, and is therefore of crucial importance for modern cosmology. The CMB radiation is one of the best understood physical phenomena in cosmology and allows to determine, with a very good precision, the parameters of the cosmological standard model. The CMB is the dominant photonic component in the Universe, constituting a very high percentage of the total radiation energy at all wavelengths, as shown in Fig. 1.3. The CMB spectrum is characterized by an accurate spectrum of black-body radiation with temperature T = 2.725 ± 0.001 K and peaked at $\lambda \sim 2$ mm [33].

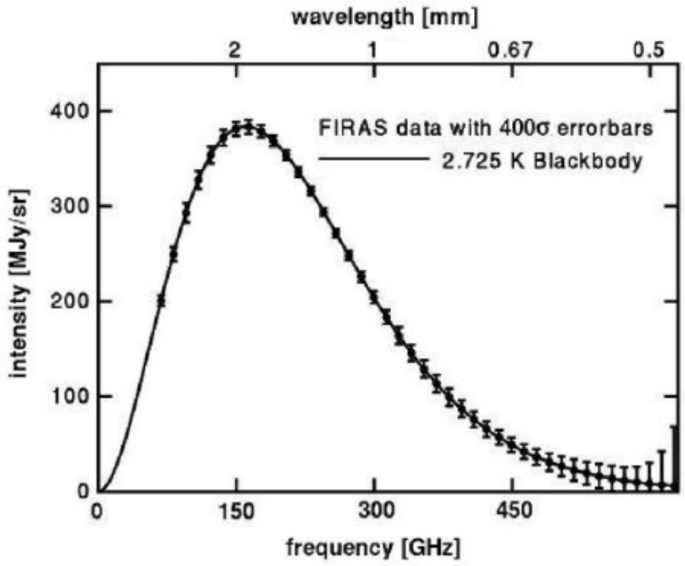

Figure 1.3: CMB spectrum with the frequency, intensity and wavelength in the axes.

In 2001, after the COBE mission [34], the satellite known as the Microwave Anisotropy Probe (WMAP) [35] was launched into orbit in 2001 to measure with high resolution temperature anisotropies in the cosmic background radiation. The anisotropies then detected were used to test the main cosmological models, such as the BBN. The measurement of the cosmic baryonic density, and thus of η, is one of the most precise results obtained by WMAP.

Before the WMAP measurements, η was the only free parameter in the BBN model. The only way to know the baryonic density was to derive it from the observed abundances of D, ^{4}He and ^{7}Li. The abundance of each of these three isotopes ideally provided us a value of η which was in a range where all the baryonic density values agreed. Now, the new baryonic density value, based on the CMB [33], is much more accurate and allows us to eliminate the last remaining free parameter in the BBN, giving us a new opportunity to check the validity of this model.

Using the BBN as an input and propagating the errors, the correlations with observations for all light elements can be calculated. Fig. 1.4 displays the results based on the WMAP data [36], superimposing

them on the measurements of the primordial abundances discussed above. The figure shows the light element abundance predictions as a function of the baryon-to-photon ratio η. From top to bottom are the light element abundances: the mass fraction of baryons in ^{4}He, the mole fraction of D, ^{3}He and ^{7}Li relative to hydrogen. The outlined green boxes describe observational constraints. The vertical band represents the baryon density constraint from WMAP ([35; 37; 38] and references therein). Observing the intersection of the yellow line and the green area, we note that the observations for deuterium and ^{4}He [31] are in perfect agreement with the predictions. Considering the lithium, the BBN and WMAP predictions and the measurements are in complete disagreement.

1.3 The ^{7}Li Cosmological Problem

Although the Big Bang theory is in excellent agreement with observational data of both deuterium and ^{4}He [26; 31], it is not as consistent with the measurements of the abundance of ^{7}Li, which turns out to be about three times lower than expected [31]. This is what is called **the Cosmological Lithium Problem**. This can be observed in fig. 1.4:

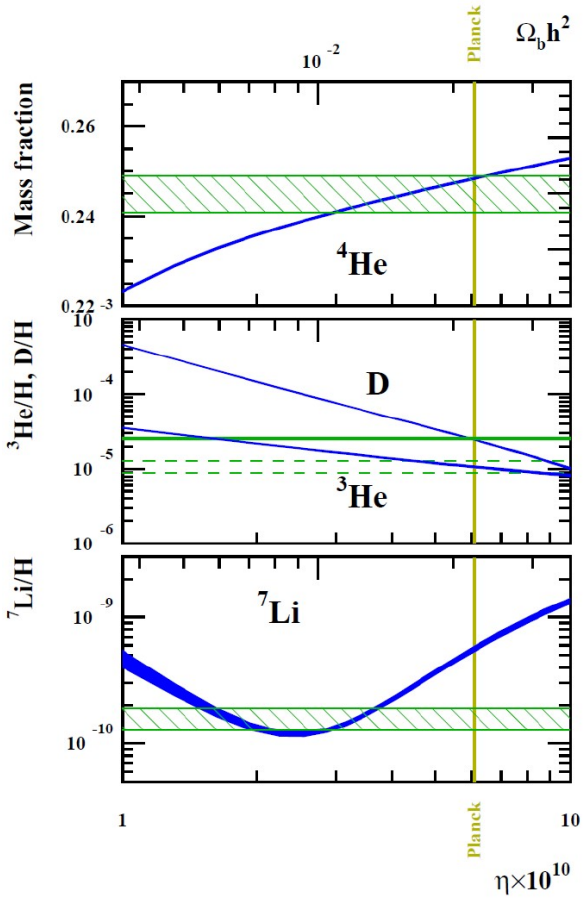

Figure 1.4: The blue lines represent the theoretical abundances in helium mass fraction (top panel) and in number of atoms with respect to hydrogen for deuterium, ^{3}He [6] (medium panel) and ^{7}Li [10] (bottom panel) as a function of the baryonic density parameter. The vertical band represents the parameter obtained from the Planck mission, while the horizontal lines represent the observed primordial abundances. As can be seen, the observations for the lithium abundance are much lower than the theoretical estimate.

1.3.1 Origin of the problem

By focusing our attention on the need of BBN investigations, astronomers have to select proper "primordial" stellar sites [20]. For this reason, low-metallicity stars are routinely selected, since their low metallicity is a typical "fingerprint" of their old age. As a consequence, lithium is measured in the

atmosphere of metal-poor stars in the galactic halo (type II stars population) with mass lower than the Sun and life time estimated to be longer than the age of the Universe [39; 40; 41].

Besides BBN, lithium can be either created (e.g. by novae stars, galactic cosmic rays and spallation) or destroyed (by nucleosynthesis within stars) and therefore, in order to infer that the observed lithium, e.g. in metal-poor dwarf stars, is primordial lithium, it is possible to study its dependence on metallicity and temperature in a certain sample of stars. Heavy metals such as iron are produced during stellar nucleosynthesis, and thus increase with time. If there were a strong variation in the abundance of lithium from star to star, dependent on metallicity or temperature, it could be argued that the observed lithium is not primordial, but related to galactic nucleosynthesis [31; 39; 41]. It was Spite in 1982 [42] who demonstrated that the abundance of lithium in metal-poor stars is independent of both the metallicity of the star and its temperature. This behaviour is very different from that of other elements, whose abundance usually decreases with decreasing metallicity. What is found instead for for lithium is the so-called Spite Plateau [7]. They therefore interpreted this plateau as a sign of the primordiality of the observed lithium [10].

If, however, this really represents the primordial lithium created during the BBN and the theory of primordial nucleosynthesis is correct, the observational data and theoretical data should agree. However, this is not the case, as the predicted theoretical abundance is much higher than the observed one.

1.3.2 Possible solution to the ^{7}Li problem

Besides the recently proposed stellar physics solutions of Fu et al. [39], Nordlander et al. [43] attributed the origin of the discrepancy to the interplay between depletion mechanisms and/or enrichment process due to interstellar gas which involve several nuclear reactions affecting the evolution of the ^{7}Li abundance [44]. On these bases, the search of nuclear physics solutions has triggered several works in the last years. Among these, nuclear physics processes involving the unstable ^{7}Be ($t_{1/2} = 53.22 \pm 0.06$ days) are of particular interest. In more detail, at η_{CMB} ^{7}Li is mainly produced from ^{7}Be that undergoes the electron capture process $e^- + {}^7\text{Be} \rightarrow {}^7\text{Li} + \nu_e$ at late times (i.e., long after the ^{7}Be synthesis).

One thus expects that the primordial ^{7}Li abundance is essentially determined by the ^{7}Be production and destruction rates at the temperatures T = 20–70 keV at which ^{7}Be is synthesized in the early universe [20]. The dominant BBN ^{7}Be production channel, i.e., the ^{3}He(α,γ)^{7}Be reaction, has been studied by Bemmerer et al. in 2006 [45] and in Leva et al. in 2009 [46], leading to an overall uncertainty of about 7% [20], thus making it a poor possible solution to the lithium problem. Furthermore, the destructive ^{7}Be(d,p)2α [47] channel has also been investigated without any significant impact on the lithium problem solution.

In the last 5 years many works have been published regarding the ^{7}Be destruction channels involving neutrons, i.e., the ^{7}Be(n,p)^{7}Li, and ^{7}Be(n,α)^{4}He reactions. In particular, the (n,α) reaction channel has been the subject of recent studies by Hou et al. [48], Barbagallo et al. [49], Kawabata et al. [50] and Lamia et al. [51]).

In this work I am going to present a new cross section measurement for the ^{7}Be(n,α)^{4}He performed via the Trojan Horse Method (THM) applied to the Quasi-Free (QF) ^{2}H + ^{7}Be reaction. In the following, the details about the method, the experiment, and the data analysis will be presented together with the implications for BBN.

CHAPTER 2

Basic features of thermo-nuclear reactions

2.1 Basic features of astrophysical nuclear reactions

Let us consider a nuclear reaction

$$x + A \rightarrow y + B, \tag{2.1}$$

or in the synthetic form, $A(x, y)B$ where A indicates the target nucleus, x the projectile, y the ejectile and B the residual nucleus [23]. From the law of conservation of energy, it is possible to introduce the reaction Q_{value} given by:

$$Q_{value} = (m_x + m_A - m_y - m_B)c^2 \tag{2.2}$$

where m are the masses of the participant nuclei. A positive Q_{value} indicates an exo-energetic reaction, i.e. one that produces energy. Vice versa, a negative Q_{value} indicates reactions that need a minimum amount of energy to be expended for them to take place [52]. Another important quantity to be

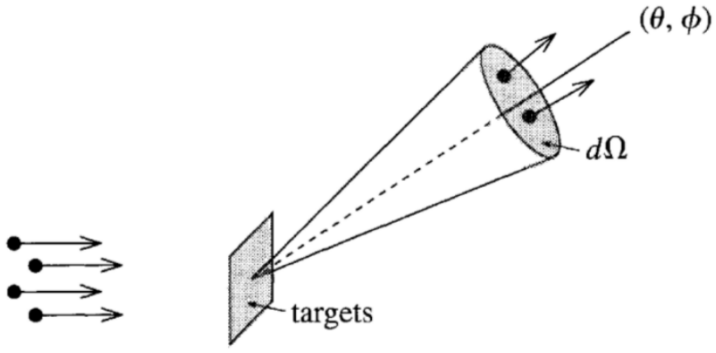

Figure 2.1: Schematization of the concept of differential cross section.

considered in the study of nuclear reactions is the probability that a given reaction takes place. Experimentally, the study of a nuclear reaction can generally be carried out by making the nuclear species of interest interact directly. Once the reaction products are detected, it is possible to obtain the value of the cross section $\sigma(E)$. For this reason, the concept of cross section (σ) is introduced 2.1: given a flux I_0 of nuclei x incident on a target containing N nuclei of type A per unit of surface and y being the number of particles emitted, it will be [24]:

$$\sigma = \frac{num.\ of\ nuclei(y)\ emitted/t}{(num.\ of\ incident\ particles\ (x)/t)(\frac{num.\ of\ atoms\ A}{surface\ unit})}. \tag{2.3}$$

In this case we have considered that the particles are emitted isotropically. In practice, it is necessary to consider the particles actually detected in the detector. In the case of an ideal detector, the differential cross section can be defined as:

$$\frac{d\sigma}{d\Omega} = \frac{N_y(\theta)}{N_x \rho_A \Delta\Omega}, \tag{2.4}$$

where $N_y(\theta)$ indicates the number of nuclei y emitted at a certain polar angle θ, N_x the number of incident particles of type x, ρ_A the density of nuclei A contained in the target and $\Delta\Omega$ the solid angle subtended by the detector [53]:

$$\Delta\Omega = \frac{A_r}{d^2}, \tag{2.5}$$

where A_r is the area of the detector and d is the distance between the detector itself and the target. The cross section has therefore the dimensions of a surface and its unit of measurement is the barn (1 barn = 10^{-24} cm^2) and it depends on the energy or, equivalently, on the relative speed between the incident nuclei.

In nuclear astrophysics, besides the cross section, it is essential to define another parameter: the reaction rate. It expresses the number of reactions per unit of time and volume at a given plasma density. The reaction rate, r, is related to the cross section by the relation:

$$r = N_x N_A v \sigma(v), \tag{2.6}$$

where N_x and N_A represent the number of incident and target nuclei per unit of volume, respectively, while v is the relative velocity between the colliding partners. The stellar plasma under quiescent burning conditions can be described as a non-degenerate and non-relativistic gas of particles. The velocity distribution of particles with mass m is described by a Maxwellian distribution [52]:

$$\phi(v) = 4\pi^2 \left(\frac{m}{2\pi kT}\right)^{3/2} exp\left(-\frac{mv^2}{2kT}\right). \tag{2.7}$$

Substituting the 2.7 in 2.6 and taking the average on the velocities, it is possible to obtain the total reaction rate:

$$r = N_x N_A v < \sigma(v)v >, \tag{2.8}$$

where $< \sigma(v)v >$ is the reaction rate for a particles pair, and can be expressed as:

$$< \sigma(v)v > = \int_0^\infty \phi(v) v \sigma(v) dv. \tag{2.9}$$

Since it is not possible to distinguish between identical particles, in the expression of the total rate the Kronecker delta function δ_{Ax} is introduced, so that [52]:

$$r = N_x N_A v < \sigma(v)v > (1 + \delta_{Ax})^{-1}. \tag{2.10}$$

Once the rate is known, it is possible to derive the information on the time evolution of the abundances of the nuclei involved in a certain nuclear reaction. Considering a generic reaction $A(x, y)B$, the abundance variation N_A due to the bombardment of nuclei x is given by:

$$\left(\frac{dN_A}{dt}\right)_x = - < \sigma v > N_x N_A. \tag{2.11}$$

The average lifetime of nuclei A depends, therefore, on the density N_x and the reaction rate per particle pair. This last quantity depends on the temperature of the astrophysical environment. Moreover, the cross section depends on the energy, which in turn reflects the dependence of the abundance variation on the mechanism through which the reaction proceeds.

In the following paragraphs I will illustrate the general concept of astrophysical reactions and the theoretical formalism specific for this type of reactions.

2.1.1 Centrifugal barrier

Nucleons are subject to the nuclear strong force. This force is short-range (of the order of Fermi) and has an attractive behaviour at distances comparable to the size of the nucleus and repulsive at small distances. This interaction is often approximated with a central potential $V(\vec{r})$, a potential that depends only on the modulus of the vector $\vec{r}$ and not by its direction [24]. In the simple case of a scattering process of a neutral nucleon, i.e. a neutron, it is possible to write the Schrodinger equation as:

$$\left[-\frac{\hbar^2}{2m} + V(\vec{r})\right]\psi(\vec{r}) = E\psi(\vec{r}) \tag{2.12}$$

Since the potential $V(\vec{r})$ is central and the angular momentum is a constant of the motion, the wave function can be factorized into a radial and an angular part:

$$\psi_{lm}(\vec{r}) = u_l(\vec{r})\Psi^l_m(\theta,\phi). \tag{2.13}$$

Consequently, Eq. 2.12 can be divided into an angular and radial part. In particular, the radial part is expressed as:

$$-\frac{\hbar^2}{2m}\frac{d^2u_l}{d\vec{r}^2} + \left[V(\vec{r}) + \frac{\hbar^2}{2m}\frac{l(l+1)}{\vec{r}^2}\right]u_l = E_{u_l} \tag{2.14}$$

where the term $\frac{\hbar^2 l(l+1)}{\vec{r}^2}$ represents the energy associated with the orbital motion of a particle in an orbit with angular momentum l. This term behaves as a repulsive potential and increases as l increases. For this reason, it is called centrifugal potential or centrifugal barrier and has the main effect of inhibiting the nuclear reactions induced by neutrons with high l. It is possible to extract the expression for the effective potential from the formula above:

$$V(\vec{r})_1 = V(\vec{r}) + \frac{\hbar^2 l(l+1)}{2\mu\vec{r}^2} \tag{2.15}$$

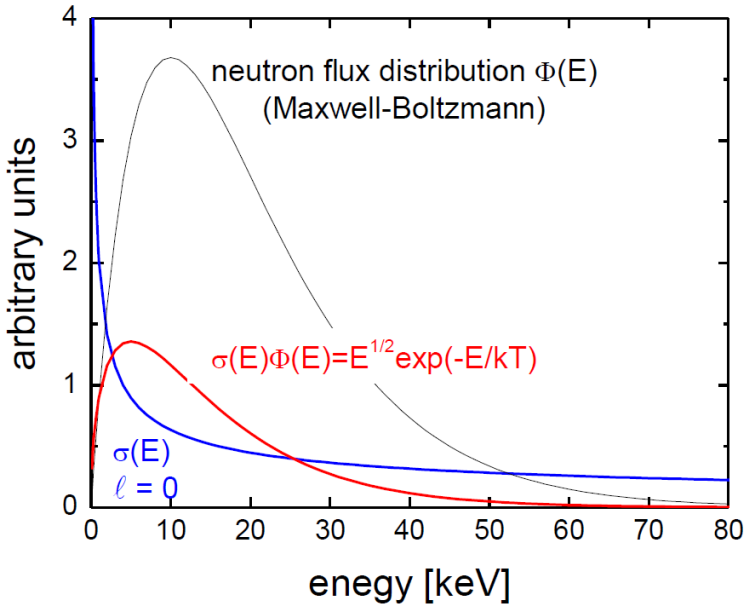

Figure 2.2: Maxwell-Boltzmann neutron flux distribution (black line), s-wave neutrons cross section (blue line) and product of neutron flux and neutron cross section (red line).

It is possible to calculate the probability of penetration of such a barrier for a free particle (wave function calculated at infinity) by means of the equation [24]:

$$P_l(E,R_A) = \left|\frac{w_l(\infty)}{w_l(R_A)}\right|^2 = \frac{kR_A}{F_l^2(kR_A) + G_l^2(kR_A)} \tag{2.16}$$

where R_A is the radius of the target nucleus, k is the wave number (defined as $p/\hbar$) and F_l and G_l depend on the Bessel ($j_l(kR)$) and Neumann ($n_l(kR)$) spherical functions, respectively.

2.2 Reaction mechanisms

2.2.1 Resonant reactions

A resonant reaction is characterized by the fact that the energy of the entrance channel is equal (or very close) to the energy of an exited level of the intermediate nucleus. This process can be described as:

$$A + x \rightarrow C^* \rightarrow B + y \tag{2.17}$$

Defining Q as the threshold energy in order to populate the $C*$ states with the reaction and E_r as the excitation energy of the $C*$ i-level, it is possible to define a resonant reaction [54] if the following condition is satisfied:

$$E_{c.m.} + Q = E_r \tag{2.18}$$

where $E_{c.m.}$ is the energy of the system $A+x$ in the centre of mass frame. Together with the resonant energy, it is possible to define the resonant cross section using the Breit-Wigner expression as described in [52]:

$$\sigma_{BW}(E) = \pi\lambda_{DB}^2 \frac{2J+1}{(2J_A+1)(2J_x)}(1+\delta_{Ax})\frac{\Gamma_a\Gamma_b}{(E-E_R)^2+(\Gamma/2)^2}, \tag{2.19}$$

where the last term is strongly energy dependent. In Eq. 2.19:

- Γ_a is the partial width for decay as "entrance channel configuration", i.e. the probability of compound nucleus formation via entrance channel;
- Γ_b is the partial width for decay as "exit channel configuration", i.e. the probability of compound nucleus decay via exit channel;
- Γ is the total width, i.e. sum of the partial widths of all open (energetically allowed), decay channels of the compound nucleus $\Gamma = \Gamma_1 + \Gamma_2 + ...$
- the term $\frac{2J+1}{(2J_A+1)(2J_x)}$ is a spin factor term ω, where J is the spin of the compound nucleus state, J_A is the spin of the projectile and J_x is the spin of the target;
- finally, the first term is the geometrical fraction term proportional to $\frac{1}{E}$.

We have to keep in mind that partial widths are not constant but energy dependent.

In the case of single isolated and narrow resonances ($\Gamma << E_r$) (see Fig. 2.3), the resonance must be near energy of astrophysical interest to contribute to stellar rate. Moreover, we can assume the Maxwell-Boltzmann distribution to be constant over the resonance region. The partial widths can also be considered constant, i.e. $\Gamma_i(E) \leq \Gamma_i(E_r)$.

From the equation of the reaction rate [52]:

$$< \sigma v >_{12} = \left(\frac{2\pi}{\mu_{12}kT}\right)^{3/2} \hbar^2(\omega\gamma)_R exp\left(\frac{E_R}{kT}\right) \tag{2.20}$$

the exponential dependence on energy indicates that the rate is strongly dominated by low-energy resonances ($E_R \rightarrow kT$), if any. Even small uncertainties in E_R may imply large uncertainties in reaction rate.

2.2.2 Sub-threshold resonances

A sub-threshold reaction is defined as a reaction where the energy E_R associated to the excited state C of the compound nucleus of reaction 2.17 is lower than the energy necessary to form the same nucleus C (E_{thr}). If E_R is less than the reaction Q_{value} then we speak of sub-threshold resonance. As shown

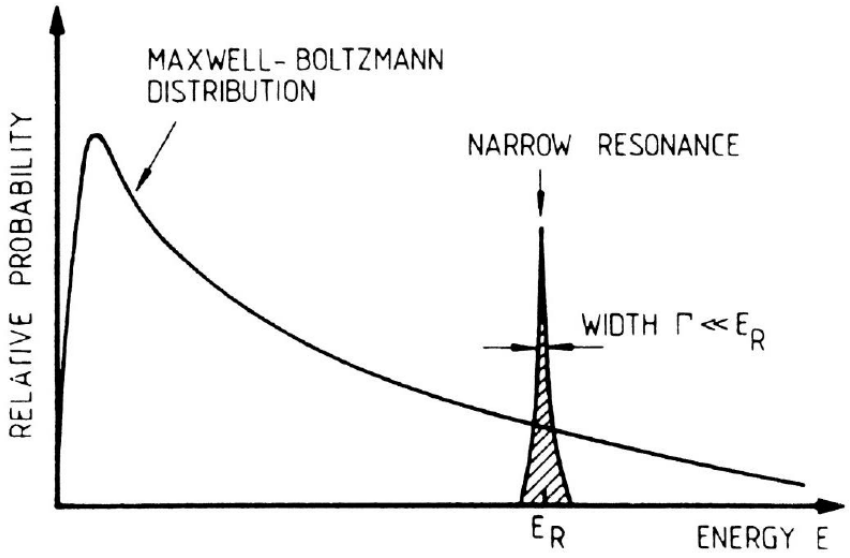

Figure 2.3: Isolated narrow resonance near the energy range of astrophysical interest. The Maxwell-Boltzman distribution is assumed constant over resonance region. The Partial widths are also constant $\Gamma_i(E) \leq \Gamma_i(E_r)$. Figure taken from [52].

in Fig. 2.4, even if it is below the reaction threshold, it is possible that the energy level E_R contributes to the cross section of the reaction because the energy width of the level could extend beyond this threshold and, consequently, give a non-negligible contribution to the development of the cross section or, equivalently, to the astrophysical S-factor (Fig. 2.4). In the presence of a sub-threshold resonance, the analytical expression for the cross section is given once again by the Breit-Wigner formula 2.19.

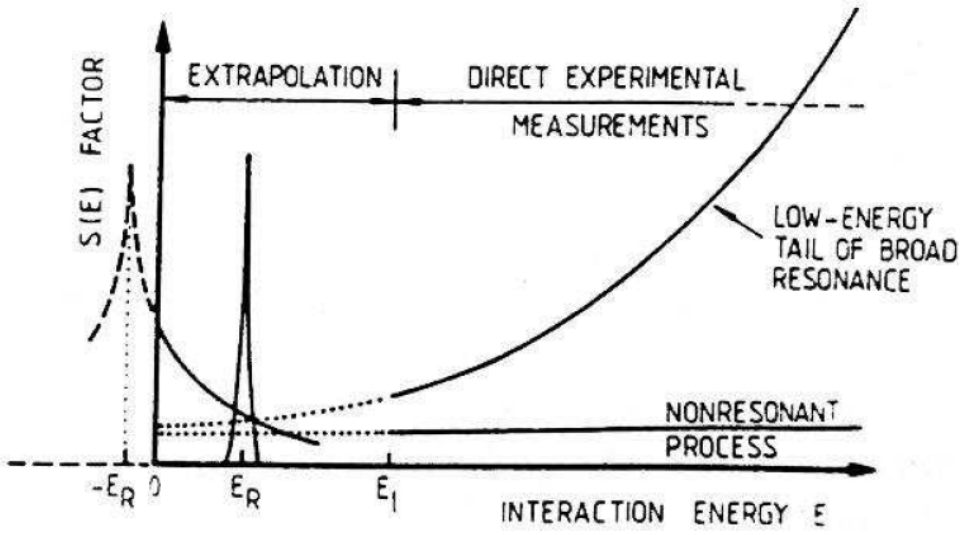

Figure 2.4: Sub-threshold resonance: possible effects on the cross section in the energy range of astrophysical interest, taken from [52].

2.2.3 Non-resonant reactions between charged particles

Non-resonant reactions are direct transitions from the initial state to the final state without the formation of an intermediate excited state. In the specific case of non-resonant reactions between charged particles, let us consider two nuclei x and X with charge respectively Z_x and Z_X. If these nuclei are at distances larger than a few Fermi, i.e. at distances greater than the nuclear dimensions $r_n = R_X + R_x$, they experience a Coulomb repulsion force and therefore the Coulomb potential energy

is equal to:

$$E_C(r)_{Coul} = \frac{1}{4\pi\epsilon_0}\frac{Z_X Z_x e^2}{r_n} \tag{2.21}$$

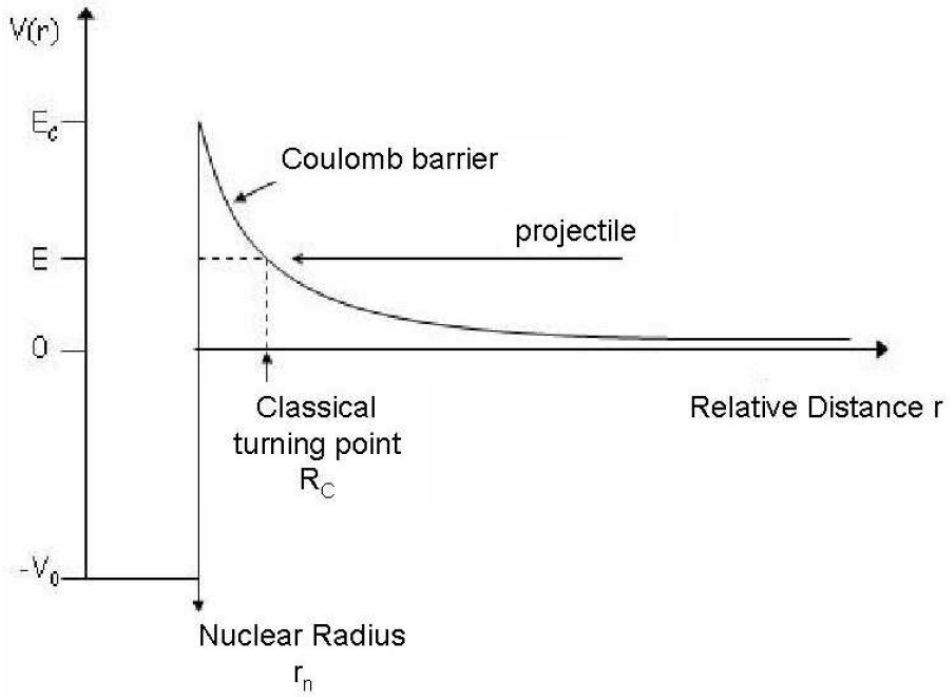

Figure 2.5: Behavior of the total potential between two interacting nuclei as function of their relative distance r. The sharp shape of the Coulomb barrier around the nuclear radius r_n must be considered as only indicative.

At large distances ($r >> r_n$) the interaction between the two nuclei is essentially governed only by the electromagnetic force, while at distances comparable or smaller than the nuclear dimensions the interaction between the two nuclei is governed only by the strong nuclear force. The net result is a total potential whose trend is shown in Fig. 2.5. In a classical picture, in order for the nuclear reaction to occur it is necessary that the distance between the colliding nuclei is smaller than r_n, that is to say that the incident energy has to overcome the threshold value of:

$$E_C = 1.44\frac{Z_X Z_x}{r_n} MeV \tag{2.22}$$

Considering both stellar and primordial nucleosynthesis processes, the energy E of the incident nucleus can vary from 10^{-1} keV to 10^2 keV. This value is typically much lower than the Coulomb barrier between the two interacting nuclei. Therefore, from a classical point of view, the reaction could proceed only when the energy between the reacting nuclei is greater than the Coulomb barrier acting between them. In a classical framework, crossing the Coulomb barrier is not permitted. In the conditions previously described, from a quantum point of view there exists a probability, small but finite, that such a crossing occurs also in the conditions in which the relative energy between the interacting nuclei is smaller than the Coulomb potential energy. This phenomenon of penetration of the Coulomb barrier, known as the "tunnel effect", is of fundamental importance for stellar processes. In the case of non-resonant reactions between charged particles and for energies $E << E_C$, the probability P of crossing the barrier decreases exponentially with the kinetic energy as:

$$P \propto e^{-2\pi\eta} \tag{2.23}$$

where

$$\eta = \frac{Z_x Z_X e^2}{\hbar v} \tag{2.24}$$

it is called Sommerfeld parameter where Z_x and Z_X are the charges of the interacting nuclei. For non-resonant reactions of the type $a + X \rightarrow b + Y$, the cross section can be written as:

$$\sigma \propto \pi\lambda^2 \cdot P_l(E) \cdot | < b + Y|H|a + X > |^2 \tag{2.25}$$

where $\pi\lambda^2$ is the geometrical factor, $P_l(E)$ is the penetrability probability which depends on projectile angular momentum l and energy E, whereas $| < b+Y|H|a+X > |$ is the interaction matrix element. The determination of the cross section for direct nuclear reactions between charged particles at energies of astrophysical interest is often very difficult if not even impossible. The presence of the Coulomb barrier between the interacting nuclei in fact reduces exponentially the value of the cross section as the energy decreases, making it difficult to determine $\sigma(E)$ or equivalently of the astrophysical factor $S(E)$ linked to the cross section through the following relation [52]:

$$\sigma(E) = \frac{S(E)}{E} e^{-2\pi\eta} \tag{2.26}$$

where

$$\eta = \frac{Z_x Z_X e^2}{\hbar v} \tag{2.27}$$

where $S(E)$ is the so-called astrophysical factor and contains all nuclear effects. Using 2.26 into 2.9 we obtain the final expression for the non-resonant reaction rate:

$$< \sigma v >= \left(\frac{8}{\mu\pi}\right)^{1/2} \frac{1}{(k_b T)^{3/2}} \int_0^\infty S(E) exp\left(- \frac{E}{k_b T} - \left(\frac{E_G}{E}\right)^{1/2}\right) dE \tag{2.28}$$

where

$$E_G = 0.978(Z_X X_x)^2 \mu(MeV) \tag{2.29}$$

is the already mentioned Gamow energy. Since for non-resonant reactions the astrophysical factor $S(E)$ varies little with energy (as shown in Fig. 2.6) [55], the behaviour of the rate 2.28 depends on the exponential term in the integral function. This term is given by the product of two factors that represent respectively the trend of the Maxwell-Boltzmann distribution and the tunneling probability through the Coulomb barrier. As shown in Fig. 2.7, this product develops a peak, called Gamow peak, where the probability that the reaction can proceed is maximum.

In an astrophysical environment characterised by a certain temperature T, the reactions take place in a narrow energy window centred around the energy value E_0 corresponding to the Gamow peak [52].

$$E_0 = (E_G)^{1/3} (k_b T/2)^{2/3} \tag{2.30}$$

Thermonuclear reactions in the stellar interior, as described up to this point, most likely occur within an energy window centred around the Gamow energy peak, whose width depends on the nuclear species involved in the process. This energy region remains much lower than the value of the Coulomb barrier (in the case of quiescent burning $\frac{E_0}{E_C} \sim 0.01 - 0.1$), making a direct measurement of reaction cross sections at energies of astrophysical interest extremely challenging and difficult and leading to severe uncertainties in the evaluation of $\sigma(E)$. The most common solution to such a problem is to measure $S(E)$ over a wide energy range down to the lowest energies obtainable in the laboratory and then, using the theory of nuclear reactions, extrapolating the values at the energies of astrophysical interest.

2.2.4 Electron screening

Up to this point we considered reactions, both resonant and non-resonant, that take place between nuclei that are affected only by the effects due to the presence of the Coulomb barrier. In reality, for nuclear reactions studied in the laboratory, the target and the projectile are respectively neutral atoms or molecules and ions. This implies the presence of an electronic cloud around the interacting

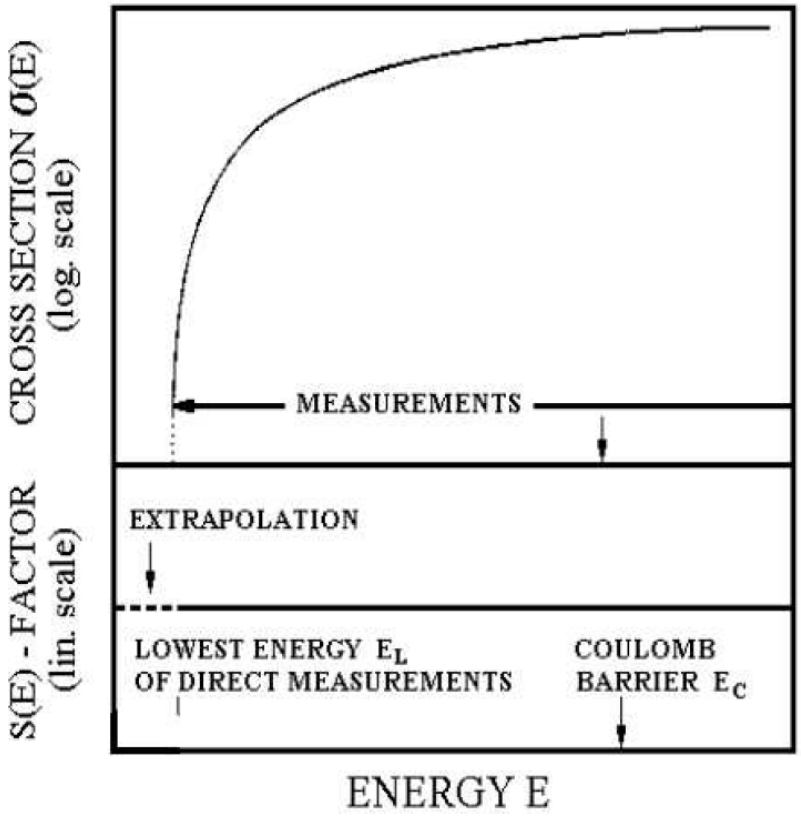

Figure 2.6: Development of the cross-section and astrophysical S-factor as energy varies. Figure taken from [52].

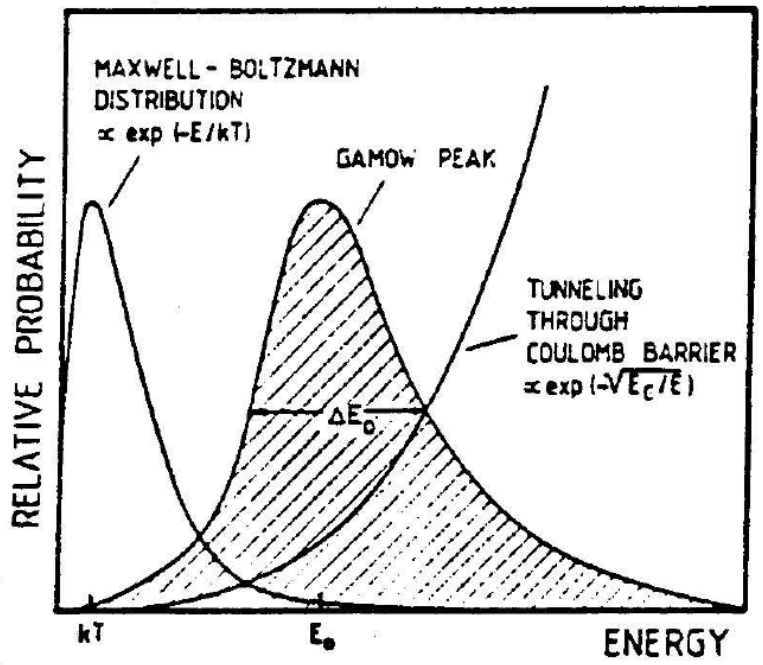

Figure 2.7: Maxwell-Boltzmann distribution and tunneling probability: the convolution of these two functions leads to the energy region relevant for the astrophysical investigation, around the so-called Gamow-peak. Figure taken from [52].

nuclei and therefore of an electronic shielding potential (see Fig. 2.8). This potential is called electron screening [55; 56]. The presence of a negative electronic potential reduces the height of the Coulomb barrier between the two interacting nuclei, making it zero outside the atomic radius R_a [55]. In other words, the incident nucleus begins to feel the Coulomb repulsion as soon as it penetrates into the region where $r < R_a$. In this region the electrostatic potential, produced by the electron cloud at distance R_a, is about constant and is equal to [52]:

$$\phi_a = \frac{Z_X e}{R_a} \tag{2.31}$$

The projectile therefore suffers from an effective potential energy E_{eff} whose height is less than the height of the Coulomb barrier and is equal to:

$$E_{eff} = \frac{Z_1 Z_2 e^2}{R_n} - \frac{Z_1 Z_2 e^2}{R_a} \tag{2.32}$$

Since the presence of the electron shielding reduces the height of the Coulomb barrier, the probability of interaction between the two nuclei increases and so does the reaction cross section.

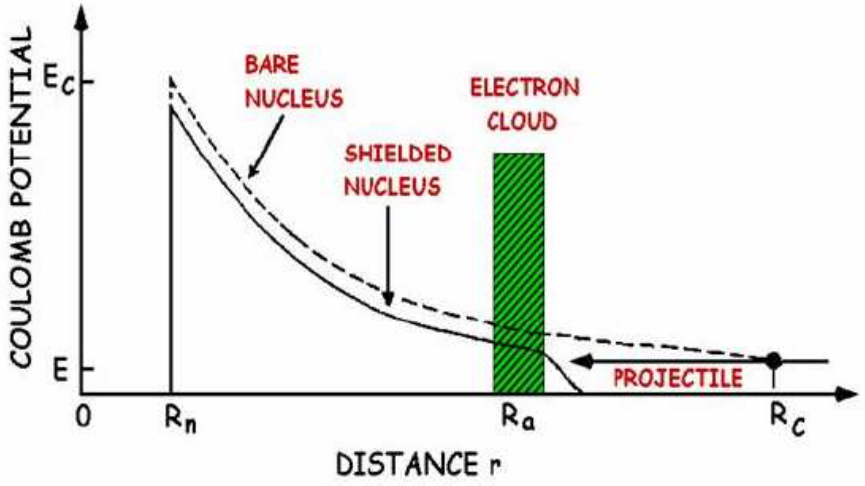

Figure 2.8: Behavior of the potential between charged particles: the presence of the electron cloud reduces the Coulomb barrier between the interacting nuclei. The "electron screening effects" cause an enhancement of the $S(E)$-factor [52].

2.3 Reactions induced by neutrons

2.3.1 Non-resonant reactions with neutrons

Most neutron induced reactions involve only two particles in the exit channel. If we schematize reactions of the type $A(n,x)B$ as two-step processes, that is, in which there is the formation of an excited state of the intermediate compound nucleus C, that subsequently decays into the emerging nuclei $B + x$. It is possible to rewrite the semiclassical form of the cross section in the following manner:

$$\sigma_{An} \propto \lambda_{DB}^2 | < B + x|H_2|C >< C|H_1|A + n > |^2 \tag{2.33}$$

where the matrix elements indicate the probability of transition for each single step, while H_1 and H_2 indicate the Hamiltonian of the system in the initial and final states, respectively [52]. These elements can be expressed in terms of the partial widths, which define the probability of the core C to be populated through the two channels of interest $A + n$ and $B + x$ [24; 52]. In the case of reactions of the type 2.17, the input channel depends only on the energy E_n of the incident neutron, while the output channel is related to the sum of the neutron energy and the reaction Q_{value}, $E_n + Q$. The cross section therefore becomes:

$$\sigma(E_n) \propto \lambda_{DB}^2 \Gamma_n(E_n)\Gamma_x(E_n + Q). \tag{2.34}$$

In the case of neutron energies lower than 500 keV (astrophysical case), we have $Q >> E_n$ and therefore Γ_x is not sensibly dependent on the energy and can be approximated to a constant: $\Gamma_x(Q)$. The remaining terms dependent on the energy are the De Broglie wavelength, which is inversely proportional to the energy of the incident neutron or, equivalently, the square of its velocity, and the partial width of the formation channel, which in a first approximation can be parametrized as:

$$\Gamma_n(E_n) \propto v_n P_{ln}(E_n) \tag{2.35}$$

where P_n represents the penetration function through the centrifugal barrier and is given by Eq. 2.16 and l_n indicates the orbital angular momentum of the incident neutron.

For thermal neutrons, i.e. with $E_n = k_B T$, where T is the temperature of the astrophysical site under examination, the contribution due to neutrons with a value of $l_n > 0$ is completely negligible [52]. Nuclear reactions are strongly favoured, therefore, only in the case of $l_n = 0$ or, equivalently, in the case of neutrons in s-wave. In this case the probability of penetration is equal to 1 and the cross section can be, therefore, expressed by [52]:

$$\sigma(E_n) \propto \frac{1}{v_n^2} v_n = \frac{1}{v_n}. \tag{2.36}$$

Under these conditions, it can be seen that the product $\sigma(v_n)$ is constant, and therefore also the reaction rate for pairs of particles is constant. The obtained result is strictly valid only for non-resonant reactions induced by thermal neutrons, where the cross section decreases with increasing velocity of the incident neutron. The case of resonant reactions will be discussed later. As the neutron energy increases, the contribution of partial waves with $l_n > 0$ becomes more and more important, therefore the rate becomes slightly velocity dependent.

In the case of reactions induced by neutrons, it is possible to define a generic reaction as:

$$A + n \rightarrow x + B \tag{2.37}$$

or, using the compact notation, $A(n, x)B$ where A and B are the target nucleus and the residual nucleus, respectively, and x is a generic emerging particle. As neutrons are particles with a neutral electric charge, they are not subject to the field generated by the protons in the nuclei involved in the reaction so they are more penetrating in the matter and subject only to the strong nuclear force generated by the other nucleons. Neutrons can travel within matter even for a few centimeters without being detected. Neutrons interact with atomic nuclei giving origin to [24]:

- Emission of secondary radiation (n, α), (n, γ), (n, p) or (n,fission), in particular for slow neutrons ($E_n < 0.5$ eV);
- Change in energy and direction of the neutrons, especially in the case of elastic scattering for fast neutrons ($E_n > 0.5$ eV).

2.3.2 Neutron beams

The main experimental difficulty in studying neutron-induced reactions is the production of neutron beams, as they are not subject to the electromagnetic force and therefore they are not easily transportable and/or accelerated. Moreover, it is not possible to use pure neutron targets because of the short average life. In this paragraph the main methods used to produce neutron beams are presented. By convention, it is possible to divide neutrons according to their energy [24]:

- thermal neutrons, $E_n = k_B T \sim 0.025$ eV;
- epithermal neutrons, 1 eV $< E_n <$ 1 keV;
- slow neutrons, 1 keV $< E_n <$ 100 keV;
- fast neutrons, 100 keV $< E_n <$ 10 MeV.

Since it is not possible to accelerate them and therefore increase their energy, the only thing that can be done is to slow them down in a process called moderation. The following part is a brief description of the methods of production of neutron beams and their achievable energies:

α-Be source. The ^{9}Be (stable isotope of beryllium) has in his fundamental state a weakly bound neutron (1.7 MeV). This neutron is released through this reaction:

$$\alpha +^{9} Be \rightarrow^{12} C + n \tag{2.38}$$

In this case, the emerging neutrons are not mono-energetic because the α particles themselves are not necessarily mono-energetic since they are produced by a radioisotope decay. Moreover, the ^{12}C could be formed in an excited state.

Photoneutron source. The ^{9}Be is bombarded with photons trough this reaction

$$\gamma +^{9} Be \rightarrow^{8} Be + n \tag{2.39}$$

where a neutron is produced. The advantage of this method is that of having emerging mono-energetic neutrons.

Spontaneous fission (^{252}Cf). Some transuranic elements decay spontaneously via the fission channel and releasing in this process a few neutrons. These sources must be shielded because fission fragments, in these cases, often further decay by β or α emission. The emerging neutrons have a Maxwellian distribution in energy, with a maximum at about 3 MeV.

Nuclear reactor. A high neutron flux is produced in the core of a nuclear fission reactor, typically of the order of 10^{14} neutrons (cm^2/s). These neutrons have a Maxwellian energy spectrum extending up to 5-7 MeV, peaked at around 1-2 MeV, and are usually moderated within the reactor itself. However, it is possible to extract these neutrons directly to the experimental chamber by drilling a suitable hole in the reactor.

Reaction with charged particles. Using a proton beam impinging on a ^{7}Li target, neutrons can be produced through the reaction

$$p +^{7} Li \rightarrow n +^{7} Be \tag{2.40}$$

.

In most methods of production of neutrons, the emerging neutrons have a Maxwellian energy distribution. It is therefore necessary the use of some kind of technique to determine the energy of each individual neutron participating in the reaction of interest. In the case of two-body reactions in the final state, by exploiting the conservation of impulse and energy, it is possible to select a certain neutron energy by choosing a precise angle of emission.

Another very used method is the Time-of-Flight (ToF) technique. This technique consists in measuring the time taken by a particle to cover a known distance, using the simple relation between kinetic energy and speed ($E = \frac{1}{2}mv^2$). In order to have high precision in the measurement of time, flight bases of the order of several tens of metres are often used.

2.3.3 Final considerations on neutron induced reactions

The methods described so far make it possible to measure the quantities introduced in the first part of the chapter for nuclear reactions induced by neutrons. However, it is necessary to point out that these methods imply several difficulties, mainly due to the production of the neutron beams needed for the reactions:

- these beams, in fact, have a Maxwellian energy distribution, making it necessary to use complex apparatuses dedicated to the tagging of the reacting neutrons in order to select the desired energy and to eliminate the contribution of background neutrons;

- in the case of mono-energetic beams deriving, as said, from binary reactions, long accumulation times are often necessary to obtain good statistics for the subsequent data analysis;
- in the use of ToF, the possibility of having a good determination of the energy of the incident neutron is directly linked to the need of having long flight bases;
- in an experimental set-up, neutrons can seriously activate all the surrounding materials making them a source of radiation. As a consequence, radio-protection is a very important issue.

In this context, as we will see in detail in the next chapter, the THM provides the possibility to use a plastic target as a source of virtual neutrons. The most important advantages of using this method are:

- THM allows to investigate directly the nuclear process of interest at astrophysical energies overcoming barrier penetration effects and/or electron screening effects;
- there is no need for the production of a neutron beam, since neutron are present in the target and the reaction can be studied in inverse kinematics;
- only one beam energy is used to cover a large fraction of the $E_{c.m.}$;
- a normalization procedure is then adopted in order to compare direct and indirect data.

CHAPTER 3

The Trojan Horse Method

3.1 Indirect methods

In order to overcome the problems listed in the previous chapter, several alternative methods have been proposed in recent years [57]: the reaction of interest is not studied directly, but different methods are used in order to derive the cross section of the astrophysical reaction of interest. These methods are called indirect methods. Each indirect method is based on a given reaction mechanism and it is linked to the reaction cross section of astrophysical interest through a given theoretical formalism. The three most important are [58]:

- the **Asymptotic Normalization Coefficient** (ANC) approach, where a transfer reaction to a bound state is measured to deduce the normalization constant of the bound state wave function, which is proportional to the reaction cross section [59];
- the **Coulomb Dissociation** (CD), where a virtual photon beam is used to photo-disintegration reaction; the detailed balance principle is then used to recover the cross section of the relevant radiative capture reaction. CD is used to extract the radiative capture cross section from the photon induced breakup in the filed of a heavy nucleus;
- the **Trojan Horse Method** (THM), where a transfer reaction to an unbound system is used to measure the cross section of a two-body process. It is used mainly for charged particle bare nucleus cross section measurement at astrophysical energies. It is possible to extract the astrophysical relevant two-body cross section from the QF contribution of an appropriate three-body reaction.

For charged particle induced reaction, the THM [60; 61] is a powerful indirect technique that allows the study of an astrophysically relevant two-body reaction from the selection of the QF channel of a suitable three-body reaction. By inducing the three-body reaction at energies higher than the Coulomb barrier in the entrance channel, the THM allows to investigate directly the nuclear process of interest at astrophysical energies overcoming barrier penetration effects and/or electron screening effects [58].

Coulomb barrier and the effect of the electronic clouds surrounding the interacting nuclei make difficult the determination of the S-factor from direct measurements in the ultra low energy region. Usually this task is achieved with the extrapolation of experimental data measured at much higher energies. Thanks to its theoretical framework, the indirect THM allows to extract the S-factor in the Gamow energy region without extrapolation; since the method does not permit to extract absolute values of the cross-section, a normalization procedure on the direct data is needed, making the THM a

complementary instruments to direct measurements for the investigation of nuclear reaction involved in astrophysics.

In particular, this method, whose extension to the study of neutron-induced reactions has been introduced in recent years, allows the use of deuterium as a virtual neutron source, making it easier to carry out experiments to study such reactions.

3.2 Quasi-free breakup mechanism

In the study of the interaction between two nuclear systems, it is possible to distinguish two extreme cases: direct and compound nucleus reaction. In the latter case there is the formation of an intermediate excited state following the collision the interacting nuclei. The kinetic energy of their relative motion is transformed into excitation energy of the compound nucleus following nucleon-nucleon collisions. If, as a result of these collisions, sufficient energy is concentrated in a nucleon or in a cluster, it is emitted. This event is quite rare so that the lifetime of the compound nucleus is orders of magnitude longer than the typical transit time of peripheral collisions. Vice versa, in the case of direct processes, the interacting nuclei do not form any intermediate state, the reactions take place very rapidly (10^{-22} s), so that no energy redistribution takes place, but only the exchange of a few nucleons between projectile and target. Examples of this type or reactions are inelastic scattering, stripping or pick-up reactions [54].

The THM is based on the theory of direct nuclear reactions and in particular of QF breakup mechanisms [61; 62], that can be carried out using the Impulsive Approximation (IA) [60; 61; 62; 63]. Let us consider the reaction $A + a \rightarrow c + C + s$, where A can be described as a cluster structure and let these clusters be x and s (in short $A = x \oplus s$). This IA is essentially based on the following three hypotheses:

- the incident particle a never interacts at the same time with the two clusters of the target;
- the interaction of the projectile a with x is the same as if x were a free particle, therefore the presence of s does not influence the interaction;
- the binding energy of the clusters in A is negligible with respect to the interaction energy between a and x.

Let us further suppose, for the sake of simplicity, that the intercluster motion $x - s$ occurs predominantly in s-wave. This implies that the pulse distribution for this motion will have its maximum at 0 MeV/c. The breakup of A into x and s is considered QF if s keeps in the output channel the same distribution of impulses that it had in A before the breakup itself [54]. Under these conditions, then, s acts as a spectator of the virtual process $a(x, c)C$.

This mechanism can be sketched through the polar diagram shown in Fig. 3.1. The upper pole

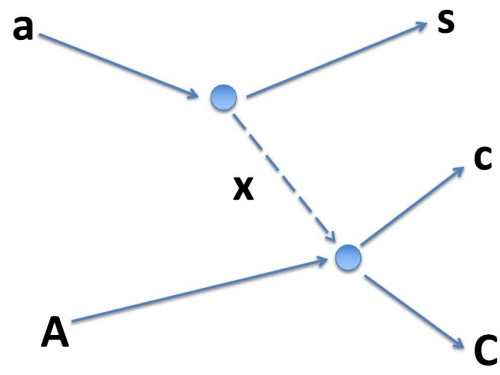

Figure 3.1: Pole diagram for the QF $a(A, cC)s$ reaction, s being the so called spectator [61], while x represents the participant to the astrophysically relevant $A(x, c)C$ reaction.

represents the QF breakup process for nucleus A, while the lower vertex represents the two-body reaction $a(x,c)C$. However, it must be underlined that the method remains valid also in the case of the breakup in the incident nucleus or if the relative motion $x-s$ does not take place in the s-wave[1].

The nucleus a (the so called "Trojan Horse nucleus") is chosen because of:

- its large amplitude in the $a = x \oplus s$ cluster configuration;
- its relative low binding energy;
- its known $x-s$ momentum distribution $|\Phi(\vec{p_s})|$ in a.

3.3 Sequential mechanism

The same products present in the exit channel of the mechanism shown in Fig. 3.1 could be, however, due to reaction mechanisms other than the QF: for example, the same particles (s,c,C) could have been produced by the formation and subsequent decay of a compound nucleus intermediate state (see Fig. 3.2).

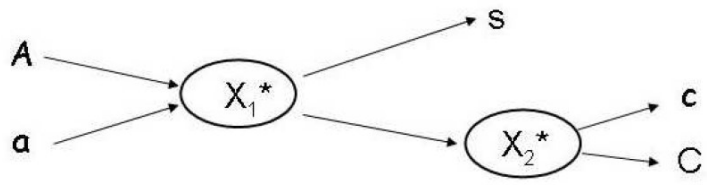

Figure 3.2: Formation and decay of intermediate states during the $A-a$ interaction: these kind of sequential mechanisms, leading to the same particles in the exit channel, cause a sort of background for the selection and the further analysis of the QF breakup process.

In this case, the nucleus comes from the decay of the nucleus X_1, therefore the corresponding pulse distribution does not coincide with that of the $x-s$ inter-cluster motion. This type of processes, called sequential processes, are not of interest in the study of QF processes. They rather represent a background which must be properly eliminated during the off-line analysis of the process. Eliminating the contribution of sequential processes is possible, but not always easy, considering the precise kinematic and energetic conditions that the the QF mechanism satisfies.

3.4 Kinematical conditions

As already mentioned, it is possible to identify the kinematic conditions necessary for the discrimination of the QF process in the three-body reaction in the final state $A(a,cC)s$. The QF mechanism, in fact, is characterised by the condition that the spectator s maintains the momentum distribution originally present in A also after the interaction between a and A. If the distribution of momentum for the relative motion of s in A has its maximum at a certain value p_s, the basic condition on the THM is that the momentum distribution maintains the same maximum and FWHM also after the breakup of A. This results in a stringent kinematic condition for the reaction products c and C. These particles, in fact, will be emitted at pair of angles (θ_c, θ_C) which, by analogy with the process, is called a pair of *QF angles*. Experimentally, therefore, by detecting the reaction products at the pair of nearly QF angles, it is possible to select the kinematic properties of the spectator s in such a way as to cover the kinematic condition at which the QF process is expected to be dominant.

[1]From the experimental point of view, only experiments with cluster in s-wave has been performed so far using D, ^{3}He and ^{6}Li

3.5 Features of the Trojan Horse Method

The idea of the THM is to extract the cross section of the two-body reaction [58; 60; 61]:

$$a + x \longrightarrow c + C \tag{3.1}$$

by properly selecting the QF contribution on a suitable three-body reaction:

$$a + A \longrightarrow c + C + s \tag{3.2}$$

A being described as $x + s$. In the QF breakup hypothesis, the incident particle a interacts only with the participant x, while s behaves as a spectator of the process [61]. If, moreover, the energy in the input channel is fixed in such a way to overcome the Coulomb barrier, the reaction of interest $a+x$ takes place directly inside the nuclear interaction region. In this way the cross section will not be affected by the effects of crossing the Coulomb and the centrifugal barriers. In this work, in particular, since one of the two particles is a neutron, the cross section will be independent from the effects due to the centrifugal barrier only.

The idea of the extension of the QF mechanisms to reactions of astrophysical interest was proposed by [60]. However, in that idea, it was foreseen that the Fermi[2] velocity of the particle x in A could partly compensate the energy of the incident nucleus a (See Fig. 3.3), which implies a relative energy E_{ax} comparable to the energies at which thermonuclear reactions are triggered in the astrophysical environment.

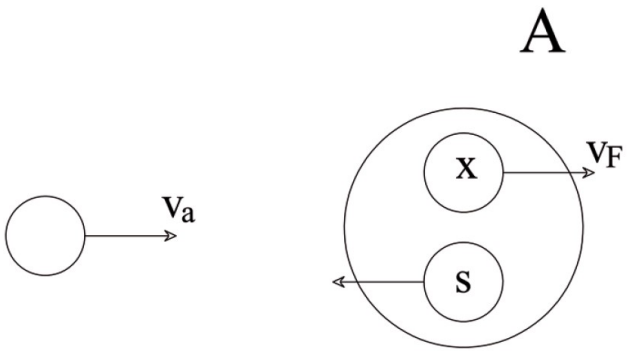

Figure 3.3: According to the initial idea of Baur [60], the relative motion of x in A could have compensated for the energy of the incident particle a. The role of the binding energy between particle x and s, B_{xs} has been underlined by Spitaleri et al. [61].

However, Baur's idea is very difficult to achieve experimentally. In order to overcome these problems, a measurement technique was devised using the low binding energy E_B of a nucleus to reach the astrophysical energies and exploiting the knowledge of QF mechanisms, developed in Catania in the 70s and 90s by researchers from Catania and Zagreb [61; 62]. In detail, it is possible to select the accessible energy region according to the relation [64]:

$$E_{c.m.} = E_{ax} - B_{xs} \tag{3.3}$$

where $E_{c.m.}$ is the centre of mass energy of the 2-body astrophysically relevant reaction, E_{ax} is the center of mass energy for the reaction of the lower pole in Fig.3.1 and B_{xs} represents the binding energy of the system $x - s$. From the law of conservation of energy and in the hypothesis of post-collision prescription suggested by [65], the value of $E_{c.m.}$ is:

$$E_{c.m.} = E_{Cc} - Q_{2bodies} \tag{3.4}$$

being $Q_{2bodies}$ the Q_{value} for the two-body reaction $a + x \rightarrow C + c$. In the present case, the three-body reaction chosen was ^{2}H(^{7}Be,$\alpha\alpha$)p, in which the deuteron acts as Trojan Horse nucleus while its clusters, proton and neutron, represent spectator and participant of the two-body process of interest, respectively.

[2]The Fermi velocity is the velocity associated with the relative motion of one of the particles in system A.

3.6 Trojan Horse Method formulation in Plane Wave Impulse Approximation

The THM was described so far with a theoretical description of QF mechanisms that can be carried out using the IA [60; 61; 62]. It was possible to consider as a typical case a simple particle (e.g. a nucleon) colliding with a complex system (a deuteron or light nucleus) having the cluster structure $A = x \oplus s$. Considering the assumptions of impulsive approximation and assuming that the incident and emerging particles can be described as plane waves and assuming that the wave function of nucleus A can be described by means of a cluster configuration, it is possible to describe the QF mechanism in Plane Wave Impulse Approximation (PWIA) [66] and to factorize the cross section for the three-body process into different terms, each one describing the two poles of the pseudo-diagram reported in Fig. 3.1, and given by the relation [64]:

$$\frac{d^3\sigma}{d\Omega_c d\Omega_C dE_c} \propto KF \cdot |\Phi(p_s)|^2 \left(\frac{d\sigma_{ax}}{d\Omega}\right)^{HOES}_{c.m.} \tag{3.5}$$

being:

- $(\frac{d\sigma_{ax}}{d\Omega})^{HOES}_{c.m.}$ the Half Off Energy Shell (HOES) differential cross section for the two body a(x,c)C reaction induced at energy $E_{c.m.}$ in the center of mass:

  $$E_{c.m.} = E_{Cc} - Q_{2body} \tag{3.6}$$

  where Q_{2body} is the Q_{value} for the virtual two body reaction and E_{Cc} is the relative energy between the outgoing particles. The cross section is "half off-energy shell" since the participant in the reaction x is a virtual particle. This means that, due to the presence of the binding energy in the Trojan Horse nucleus, its energy and momentum are not related by the mass-shell equation: $E_x = p^2/2m_x$ [57]. Under QF conditions, the relative $a-x$ energy is then determined by relation $E_{ax} = p^2_{ax}/2m_{ax}$ - ϵ_{sx}, with ϵ_{sx} being the binding energy of the Trojan Horse nucleus. In the exit channel, the relation is restored because the emitted c–C particles are real [58]. In particular, in the hypothesis of applicability of the THM, this value of the cross section for the virtual two-body reaction represents only the nuclear part, as there are no contributions from the Coulomb and centrifugal barriers [61]. The $(\frac{d\sigma_{ax}}{d\Omega})^{HOES}_{c.m.}$ is expressed in arbitrary units and for this reason it must be normalised to the values of the same cross section deduced from direct measurements carried out at appropriate energies.

- KF is the kinematic factor resulting from the development of the QF breakup reactions in plane waves, where it is assumed that the spectator cluster s maintains in the final channel the same momentum distribution it had in the initial channel. This factor can be expressed through [64]:

  $$KF = \frac{k_c k_C^2 E_s E^2_{c.m.}}{k_a E_x k_c E_s + E_c[k_c - k_a \cos\theta_c + k_C \cos(\theta_C - \theta_c)]} \tag{3.7}$$

  where k_i and E_i are, respectively, the wave numbers and the energy of the $i-th$ particle involved in the reaction, while θ_i indicates the respective angles.

- $|\Phi p_s|^2$ represents the distribution of impulses, that is the Fourier transform of the wave function $\varphi(\vec{r})$ of the relative motion of the clusters in A:

  $$|\Phi(\vec{p_s})| = (2\pi)^{-\frac{2}{3}} \int_{-\infty}^{+\infty} \psi(\vec{r}) \exp(-i\vec{K_s})\vec{r}d\vec{r} \tag{3.8}$$

  It must be underlined that, if the energy of the projectile is greater than the height of the Coulomb barrier in the entrance channel of the three-body reaction $a + A \rightarrow C + c + s$, the two-body reaction $a + x \rightarrow C + c$ takes place directly in the region of nuclear interaction, leading to the determination of the nuclear part of the cross section $\frac{d\sigma_{ax}}{d\Omega}$. In order to be able to compare this differential cross section with that deduced from direct measurements it is necessary to introduce the transmission coefficient across the Coulomb and/or centrifugal barriers.

Then we obtain the relation:

$$\left(\frac{d\sigma}{d\Omega}\right)^{THM} \propto \sum W_l P_l \left(\frac{d\sigma_{ax}}{d\Omega}\right)^{HOES} \tag{3.9}$$

where W_l and P_l are respectively the weights and the transition coefficients through the barriers. However, given the proportionality relation expressed by Eq. 3.9, the cross section obtained with the THM is in relative units. It is therefore necessary to normalize the data to the direct measurements available in the literature. In this sense the THM is not a substitute for the direct methods but rather complementary to them.

3.7 Application of the Trojan Horse Method to the ^{2}H(^{7}Be,$\alpha\alpha$)p reaction

In the present work, I am going to present a new cross section measurement for the ^{7}Be(n,α)^{4}He performed via the THM applied to the QF 2H + ^{7}Be reaction. In the following, the details about the method, the experiment, and the data analysis will be given together with the implications for BBN.

According to the theoretical description of the THM, the investigation of the relevant ^{7}Be(n,α)^{4}He two-body reaction was performed by selecting the QF contribution of the ^{2}H(^{7}Be,$\alpha\alpha$)p three-body reaction, using the deuteron target as Trojan Horse nucleus. In Fig. 3.4 the associated pseudo-Feynman diagram is reported: the upper pole represents the deuteron breakup while the lower pole represents the virtual two-body reaction of interest. In the IA framework, this representation leads to the factorization of the three-body cross section reported in the previous section. Performing an experiment where is possible to measure the QF-contribution of the three-body reaction and to know both the kinematical factor and the momentum distribution for the relative $p-n$ motion inside the Trojan Horse nucleus, makes it possible to extract the ^{7}Be(n,α)^{4}He cross section by using the relation:

$$\left(\frac{d\sigma}{d\Omega}\right)^{N}_{^7Be-n} \propto \frac{d^3\sigma}{d\Omega_\alpha d\Omega_{^7Be} dE_\alpha}[(KF)|\Phi(\vec{p_s})|^2]^{-1} \tag{3.10}$$

The choice of the deuteron as "standard" Trojan Horse nucleus [61; 62; 67] was made since the low binding energy of the $p-n$ system ($B_{pn} = 2.2$ MeV) and the momentum distribution for the intercluster motion is known from independent experiments (e.g. [68]). In particular the intercluster motion occurs mainly in s-wave [51] and its analytical form is given by the Hulthén function as expressed by equation:

$$\psi(\vec{r}) \propto \frac{e^{-ar} - e^{-br}}{e} \Longrightarrow F[\psi] \Longrightarrow \Psi(\vec{p}) \propto \left[\frac{1}{a^2 + p_s^2} - \frac{1}{b^2 + p_s^2}\right] \tag{3.11}$$

where $a = 0.2317$ fm^{-1} and $b = 1.202$ fm^{-1} are fixed [68]. The shape of the $p-n$ relative motion momentum distribution is sketched, in arbitrary units, in Fig. 3.5. Since the motion occurs mainly in s-wave, it is evident the maximum around relative momentum p_n=0 MeV/c.

Applying THM to the reaction ^{7}Be(n,α)^{4}He it is possible to extract the bare two-body cross section at energies of astrophysical interest using a three-body reaction. As previously mentioned, it must be underlined that the THM does not allow to obtain cross sections in absolute units, a normalization procedure on the direct data is therefore needed, making the THM a complementary instruments to direct measurements for the investigation of nuclear reactions involved in astrophysics. Therefore it is necessary to make a comparison between the data obtained from the direct measurements and the data extracted by the THM. In this work, the direct data used for the comparison between the direct and indirect data are provided by two previous works:

- Hou et. al in 2015 [44] used the ^{4}He(α,n)^{7}Be and ^{4}He(α,p)^{7}Li reactions in order to derive the direct ^{7}Be(n,α)^{4}He cross section by applying the charge symmetry and the principle of detailed balance (see Fig. 3.6);

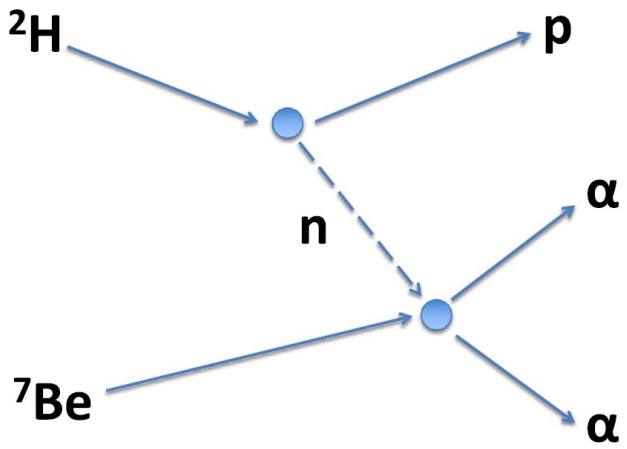

Figure 3.4: Pole diagram for the QF ^{2}H(^{7}Be,$\alpha\alpha$)p reaction. Nucleus ^{2}H represents the adopted Trojan Horse nucleus that undergoes QF breakup interacting with the ^{7}Be beam. The neutron acts as the participant of the ^{7}Be(n,α)^{4}He binary process, while the proton is the spectator.

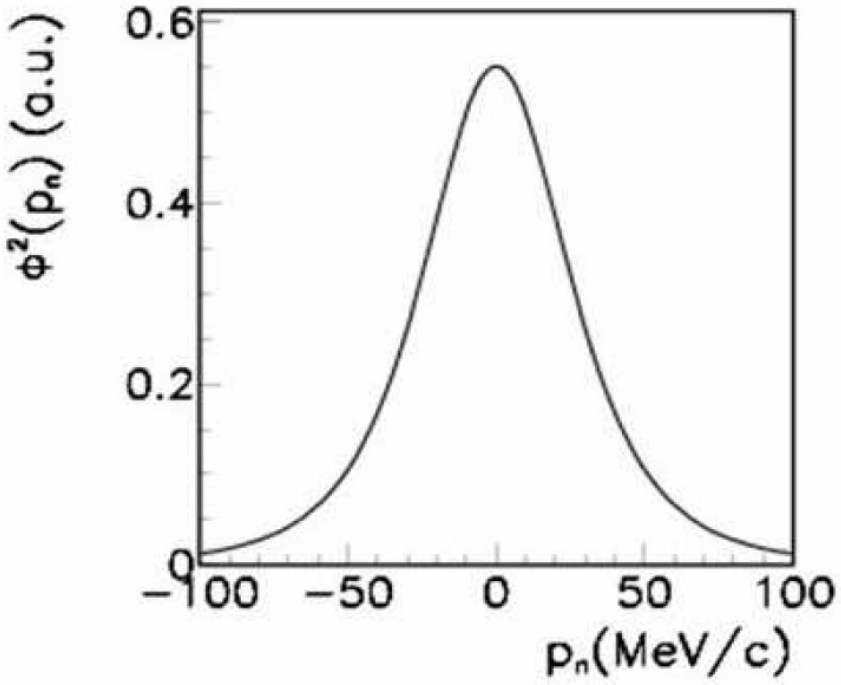

Figure 3.5: Momentum distribution for the $p-n$ relative motion inside the deuteron. The shape of such function is described by the Hulthén function, expressed in equation 5.12.

- Kawabata et. al in 2017 [50] performed a time reversal measurement of the p-wave cross section for the ^{7}Be(n,α)^{4}He reaction. In particular they first measured the cross section for the ^{4}He(α,n)^{7}Be reaction and then, thanks to the detailed balance principle, they obtained for the first time the cross sections for the ^{7}Be(n,α)^{4}He reaction at $E_{c.m.}$= 0.20–0.81 MeV, slightly above the BBN energy window (see Fig. 3.6).

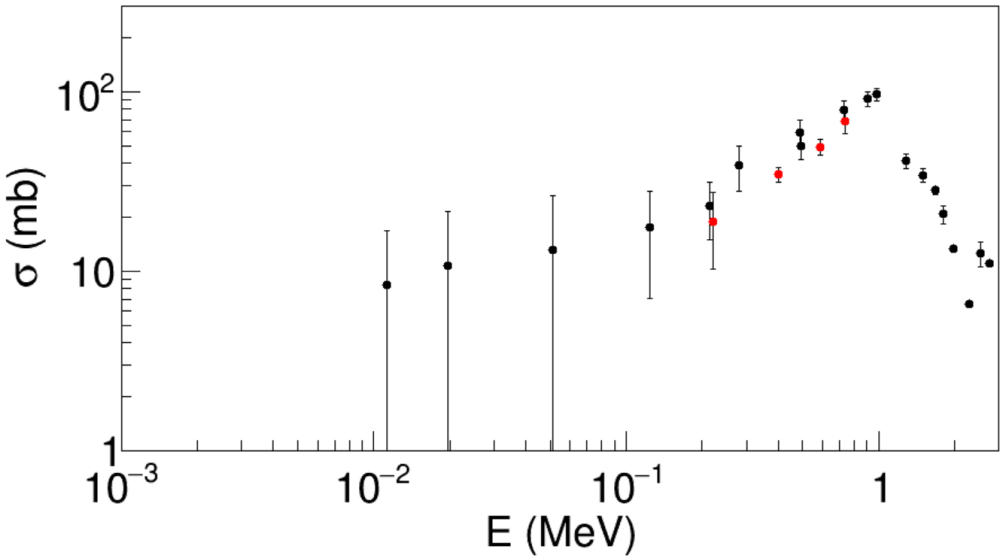

Figure 3.6: Cross section direct measurements for the ^{4}He(α,n)^{7}Be reaction of Kawabata et al. [50] (red points) and Hou et al. [48] (black points).

3.8 Recent results of the Trojan Horse Method

In recent years, several experiment were performed with the implementation of the THM analysis. In particular, I am going to give an overview of different experiment performed with charged particles, radioactive beams, neutrons and with neutrons and radioactive beams at the same time.

The first relevant experiment is the indirect measurement of the ^{19}F(p,α)^{16}O [69]. This reaction is the main destruction channel of fluorine at the bottom of the convective envelope in Asymptotic Giant Branch (AGB) stars, In this paper the THM was used to extract the S-factor in the energy range of astrophysical interest ($E_{c.m.}$ = 0–1 MeV) (see Fig. 3.7). The measurement was performed at the Laboratori Nazionali di Legnaro (LNL, Italy) with the Tandem-XTU accelerator.

Another relevant THM experiment was performed at Riken, Japan aimed at the study of the ^{18}F(p,α)^{15}O reaction [70; 71; 72], using a radioactive beam of ^{18}F produced with CNS Radioactive Ion Beam facilty (a sort of twin facility of EXOTIC at LNL), to derive important information about the phenomenon of ^{18}F abundances in novae explosion.

Finally, the reaction ^{17}O(n,α)^{14}C [73; 74] was studied at energies from $E_{c.m.}$ = 0 to $E_{c.m.}$ = 350 keV with the implementation of the QF deuteron breakup in the three-body reaction ^{17}O + d → α + ^{14}C + p, which extended the THM to neutron-induced reactions.

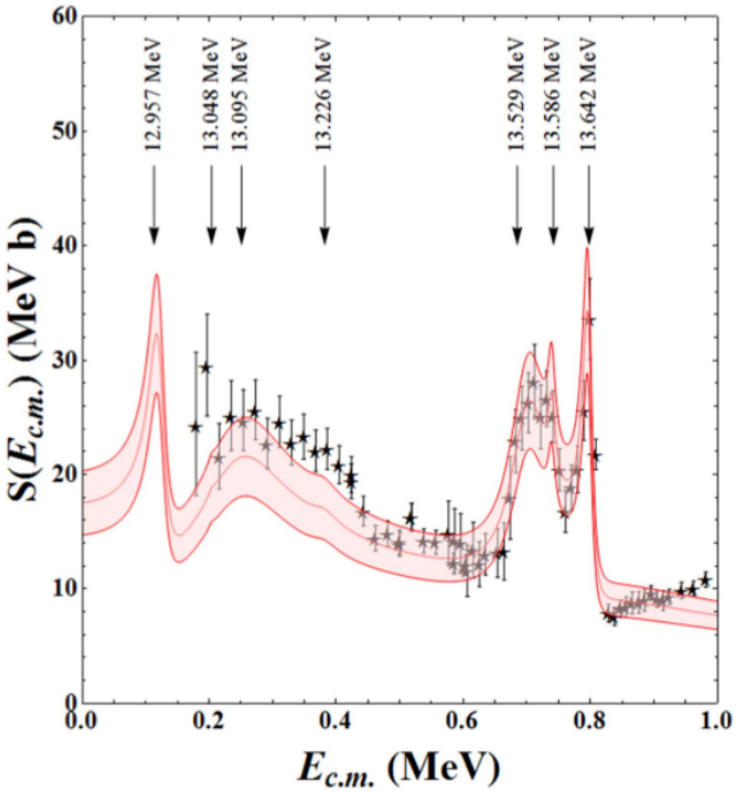

Figure 3.7: Comparison of the THM S-factor of the ^{19}F$(p,\alpha)^{16}$O [69] with direct data. The THM result is shown as a red band.

CHAPTER 4

Experimental study of the ^{2}H(^{7}Be,$\alpha\alpha$)p reaction

4.1 Radioactive Ion Beams

Experiments carried out with Radioactive Ion Beams (RIBs) are characterised by low statistics and during the RIB production, we have to take into account several technical and physical obstacles, in particular the weak interaction that lets radioactive nuclei slide along isobaric chains towards the bottom of the stability valley. The situation becomes more and more complicated as we move away from the stability valley, since the average decay lifetimes become shorter and shorter. In a rather general RIB production scheme, we have to consider the following aspects:

- the production should be fast, because of the very short average lifetime of the nuclear species involved;
- the chosen reaction mechanism should guarantee the highest possible production cross section. This task is achieved by optimising the projectile-target combination, incident energy, intensity of the primary beam and the power dissipated in the target;
- production should be selective since the contamination of unwanted nuclear species may be several orders of magnitude larger.

The EXOTIC [27; 75] facility uses the "in flight" technique for the production of light, weakly bound RIBs. The production mechanism employs inverse kinematics reactions induced by heavy ion beams on gaseous targets. The main features of the in-flight separation technique are:

- the reaction products are kinematically focused into small kinematic cones around the direction of the primary beam;
- the separation time of the primary beam and other possible contaminating reaction products is rather fast, in the order of a few μs, and is independent of the chemical properties of the RIB;
- the RIB retains a large fraction of the initial velocity of the projectile, so there is essentially no need for an additional (and expensive) re-acceleration stage;
- the selection of the RIB is carried out by means of an appropriate combinations of electromagnetic fields and/or atomic interactions;
- the production target must dissipate only a small part of the primary beam power;
- all optical elements, in particular those closest to the production target or to the areas where the the primary beam is stopped, shall be designed to operate correctly in a high radiation

environment.

4.1.1 ^{7}Be beam production

The ^{2}H(^{7}Be,$\alpha\alpha$)p experiment was performed at the INFN-LNL. The ^{7}Be beam was produced with the EXOTIC facility (Fig. 4.1). The facility has been operational since 2004 and has already delivered secondary beams of ^{7}Be, ^{8}Li, ^{8}B, ^{10,11}C, ^{15}O and ^{17}F with energies in the range 2-6 MeV and intensities ranging from about 10^3 pps (for ^{8}B) to 10^6 pps (for ^{7}Be).

The RIB production scheme uses two-body reactions in inverse kinematics. The reaction is induced by a heavy ion beam, generated by the Van de Graaff LNL-XTU tandem accelerator, which impinges on a light gas target. In the present case, the production reaction was ^{1}H(^{7}Li,^{7}Be)n (Q_{value} = -1.64 MeV).

The experiment started with a 48.8 MeV primary beam of $^7Li^{+3}$ with an intensity of about 150-200 pnA hitting a gaseous target of H_2 to induce the ^{7}Li(p,n)^{7}Be reaction. The gas was contained in a 5 cm long cell. The inlet and outlet windows were composed of 2.2 μm thick Havar foils. The target gas had a pressure of 1 bar and was cooled to the temperature of liquid nitrogen (90 K). The beam of light radioactive ions of ^{7}Be was selected and separated from the ^{7}Li scattered beam and other contaminants by means of the 30° bending magnet, the Wien filter, slit and collimation sets located at suitable positions along the beam line [76]. At the end of the beam line, an energy of $\sim$ 20 MeV, an intensity of (5–8) $\cdot 10^5$ pps, a purity of about 99%, a beam spot of about 9 mm (FWHM) and an energy spread of about 1 MeV (FWHM) were measured.

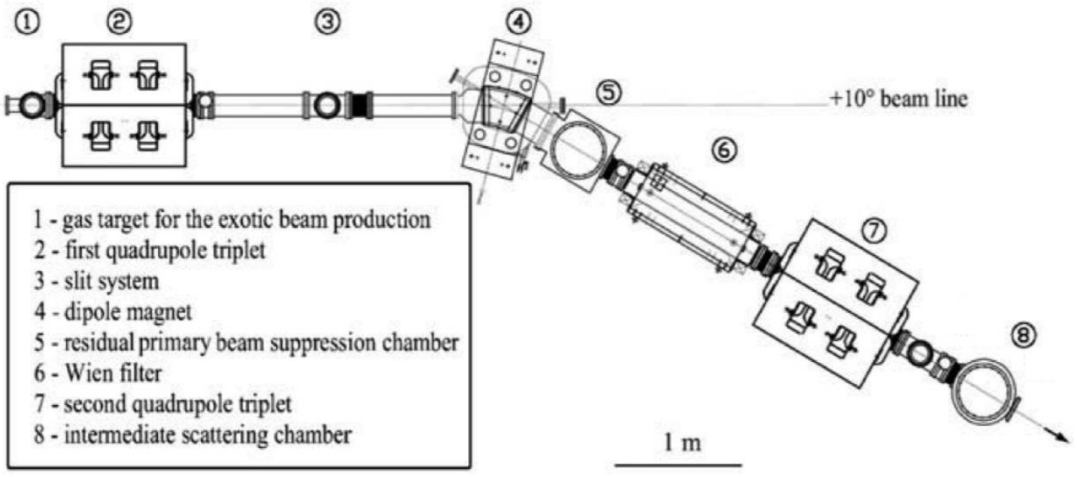

Figure 4.1: Schematic drawing of the EXOTIC radioactive beam production line at LNL.

4.1.2 ^{7}Be beam energy determination

In order for the reaction to be induced at astrophysical energies, it is necessary to choose properly the energy of the ^{7}Be beam. Here we briefly summarize the concepts that guided the choice of the secondary beam energy. The energy in the center-of-mass reference frame $E_{c.m.}$ can be calculated,

with the condition p_s=0 MeV/c, from the relation:

$$E_{c.m.} = E_{ax} - B_{xs}, \tag{4.1}$$

where E_{ax} is the the beam energy in the center of mass of the two-body reaction $a + x$ and B_{xs} represents the binding energy of the deuteron. Considering then an energy close to zero ($E_{c.m.} \approx 200$ keV) was chosen, we obtain:

$$E_{c.m.} + B_{xs} = E_{ax} \approx 2.45MeV = E_{beam}\frac{m_n}{m_n + m_{^7Be}} \tag{4.2}$$

from which, being m_n and $m_{^7Be}$ respectively the mass of the neutron and of ^{7}Be expressed in atomic mass units, we obtain for the energy of the beam:

$$E_{beam} = 20.4MeV \tag{4.3}$$

This energy turns out to be well above the Coulomb barrier between ^{7}Be and ^{2}H ($\sim$ 2.3 MeV), thus ensuring that the process occurs directly in the nuclear interaction region.

4.2 Determination of the ^{2}H(^{7}Be,$\alpha\alpha$)p kinematical region

The detectors were placed at angles such that the products of reaction (i.e. the α particles in coincidence) could be detected in a large kinematic region where the contribution of the QF mechanism is expected to be dominant. The choice of the angles where to place the detectors is related to the so-called QF angular conditions. In general, in the final state of a three-body reaction it is possible to determine the kinematic properties of the third particle by revealing only the energy and the emission angle of the other two. In addition, in the case of a QF mechanism, there is a further condition, i.e. the third particle (the spectator s) keeps unchanged in the output channel the momentum distribution p_s, as a result of the interaction between the projectile nucleus a and the participant p. Applying then the principles of conservation of energy and momentum, we can write the following system of equations:

$$\begin{cases} E_a + Q = E_c + E_C + E_s \\ \vec{P_a} = \vec{P_c} + \vec{P_C} + \vec{P_s} \end{cases} \tag{4.4}$$

where E_a and P_a represent energy and momentum of the incident particle, respectively. Imposing the condition of QF breakup, namely that the relative motion of the spectator s inside the cluster A occurs in s-wave ($l = 0$), we will have $P_s = 0$, i.e. $E_s = 0$, and then it will be possible to rewrite the system in the form:

$$\begin{cases} E_a + Q = E_c + E_C \\ P_a = P_c \cos\theta_c + P_C \cos\theta_C \\ 0 = P_c \sin\theta_c + P_C \sin\theta_C \end{cases} \tag{4.5}$$

This is a system of three equations with four unknowns. Since the energies, and therefore the impulses, of the particles are revealed, once one of the two angles is fixed, the other remains uniquely defined. The angular pair (θ_c,θ_C) thus obtained represents the pair where is maximum the probability of detecting the particles arising from the process of QF breakup.

A Monte Carlo simulation was performed to establish which were the QF angles for the reaction under consideration, allowing a suitable choice for the positioning of the detectors and also an estimate for the expected energy ranges (Fig. 4.2). In particular, in the figure are reported the results obtained with the simulation by inserting a cutoff in the distribution of the momentum of the spectator equal to $|p_s| < 100$ MeV/c (black points), a more stringent one equal to $|p_s| < 30$ MeV/c (red dots) and even a more stringent one with $|p_s| < 10$ MeV/c (blue dots). The yellow boxes indicate the angular

regions where the detector setup was placed. The corresponding kinematical locus, i.e. the scatter plot between the simulated α energies, is reported on the lower panel of Fig. 4.2, together with the events corresponding to the $|p_p| < 30$ MeV/c and $|p_p| < 10$ MeV/c conditions. In summary, the kinematical calculations suggested us to detect the α particles emitted in coincidence at $\theta_{\alpha 1} = 27° \pm 7°$ and $\theta_{\alpha 2} = 63° \pm 7°$. Fig. 4.2 displays that the detector setup should be tailored to detect and identify QF α particles in the energy ranges 24-34 MeV (horizontal axis of the lower panel of Fig. 4.2) and 4-14 MeV (vertical axis of the lower panel of Fig. 4.2) in the angular range $27° \pm 7°$ and $63° \pm 7°$, respectively.

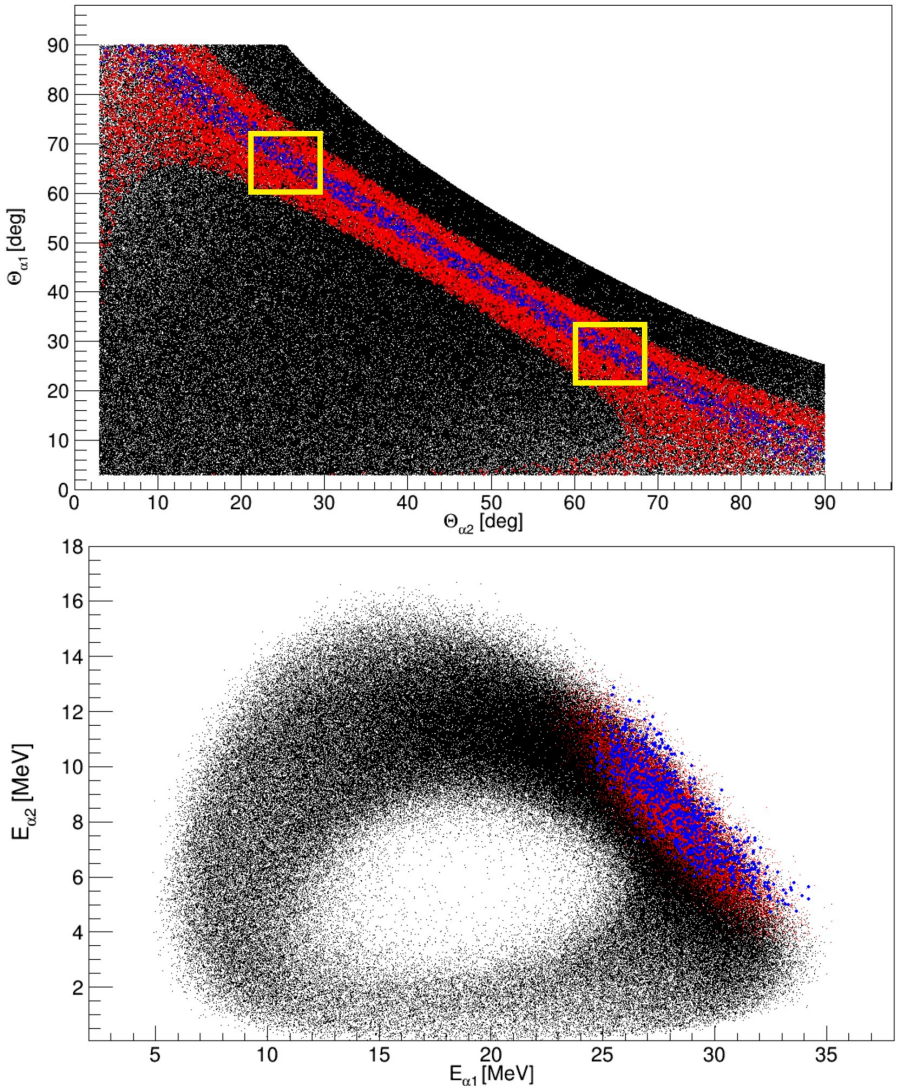

Figure 4.2: Upper panel: Emission angles for the emerging α particles in the ^{2}H(^{7}Be,$\alpha\alpha$)p reaction induced at 22 MeV. Black points refer to events with $|p_s| < 100$ MeV/c, while red and blue points refer to $|p_s| < 30$ MeV/c and $|p_s| < 10$ MeV/c respectively. The yellow boxes refer to the displacement of our detector setup for the two emitted α particles. The QF angular region falls inside the adopted setup. Lower panel: kinematical locus of the α energies together with the events corresponding to the $|p_p| < 30$ MeV/c and $|p_p| < 10$ MeV/c conditions.

4.3 Experimental set-up

Since the typical intensity of RIBs is about 10^4-10^6 pps, the layout of a high performance detector needs the following prerequisites:

- identification of the charge and mass of all reaction products with the highest achievable energy resolution;
- wide solid angle coverage to compensate for the low intensities of the RIBs and to allow coincident detection of simultaneously emitted particles at large relative angles;

- high segmentation to increase the angular resolution of the detected particles;

Since the energy deposition of a particle passing through a thin layer of material is highly dependent on the material of the layer and strongly depends on its charge and mass, the first requirement can be fulfilled by using (at least) two-stage telescopes to detect the particles. The second and third requirement can be achieved by using the Double Side Silicon Strip Detectors (DSSSD) in a very compact configuration around the target.

4.3.1 EXPADES

For this experiment, four modules of the EXotic PArticles DEtection System (EXPADES) [75] were used. This detector array, in full configuration, consists of eight telescopes arranged in a cylindrical configuration around the reaction target. The telescope structure was composed of an Ionization Chamber (IC) and a DSSSD. An additional DSSSD (with all the strips short-circuited at the entrance of the preamplifiers, later called PAD) was added to the two telescopes at the most forward angles.

$\Delta E - E$ identification technique

It is possible to exploit the assembly of an IC and a silicon detector of a given thickness is a so-called telescope configuration for the light charged particle identification using the ΔE-E technique (see Fig. 4.3). In the IC the particle releases just a fraction of its kinetic energy (ΔE), while it is entirely stopped in the second layer. If one plots the energy released in the two detectors, an identification in charge and, possibly, mass (in case of good energy resolution) of the incoming particles is possible from the different hyperboles in the (E,ΔE) correlation plot. The Bethe-Bloch formula describes the average amount of energy lost of a particle due to ionization per unit of distance (dE/dx, stopping power) in the medium as a function of its atomic number and mass. In the non-relativistic approximation, we have:

$$\frac{dE}{dx} = C_1 \frac{Mz^2}{E} ln\Big(C_2 \frac{E}{M}\Big) \tag{4.6}$$

and for a finite thickness:

$$\Delta E = \Delta x \frac{dE}{dx} \propto \frac{Mz^2}{E} \tag{4.7}$$

The same situation applies considering a telescope made up two silicon detectors, as it is the case,

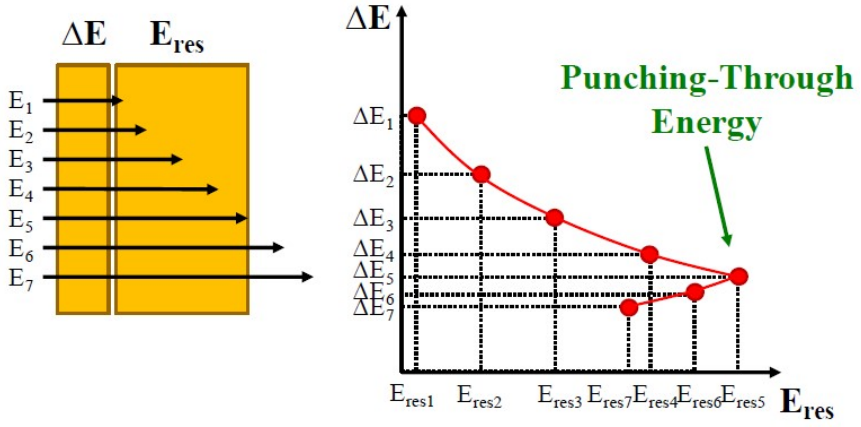

Figure 4.3: Schematic representation of the operating principle of a telescope and the visualization of the punching-trough energy concept.

for instance in our experiment, of the DSSSD-PAD configuration of the modules located at the most forward angles. According to the Bethe-Bloch formula, different isotopes occupy different locations in the ΔE-E_{res} plots. In particular, the isotopes with low A are located on the bottom left part of the chart. These curves do not intersect each other, even if a certain spread of the points could be present due to the detector energy resolution. However, with this method we can identify the nuclear species involved in the exit channel of the reaction.

The T1 and T4 telescopes (see Fig. 4.5) were placed at θ_{lab} = [56°–70°]. The two telescopes were made up by an IC followed by the 300 μm silicon strip detector without the PAD detector because low-energy α-particles were expected (i.e., with energies lower than 20 MeV). The PAD detector was added for the most forward telescopes in the angular range θ_{lab} = [20°–34°] (T2 and T3 in Fig. 4.5) because α-particles with energy up to $\sim$ 34 MeV were expected. The use of ICs guaranteed a lower threshold for α particle identification.

4.4 Detectors and readout electronics

The ^{2}H(^{7}Be,$\alpha\alpha$)p experiment was performed using a 20.4 MeV ^{7}Be beam impinging on a CD_2 target with a thickness of 400 μg cm^2. The QF ^{2}H(^{7}Be,$\alpha\alpha$)p process is represented by the pole diagram of Fig. 4.4, where the deuteron undergoes breakup in a neutron (participant) and a proton (spectator). The detection setup was laid out with the aim of detecting the two emerging α particles while the kinematical quantities of the undetected proton were reconstructed via momentum-energy conservation laws. In addition, since only QF events were considered for the THM analysis, the setup covered the kinematical region corresponding to the QF-angular pairs, i.e., the angular pairs where the spectator maintains the same momentum distribution it had inside the deuteron before the breakup [58].

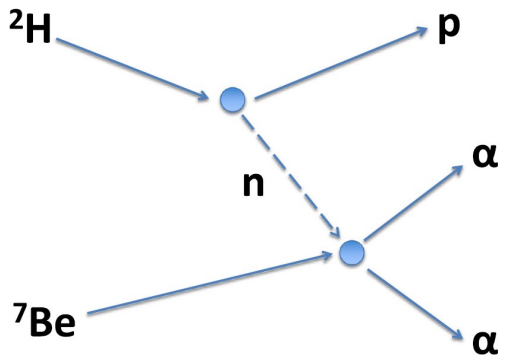

Figure 4.4: Pole diagram for the QF ^{2}H(^{7}Be,$\alpha\alpha$)p reaction. Nucleus ^{2}H represents the adopted Trojan Horse nucleus that undergoes QF breakup interacting with the ^{7}Be beam. The neutron acts as the participant of the ^{7}Be(n,α)^{4}He binary process, while the proton is the spectator.

A schematic drawing of the adopted experimental setup is given in the upper part of Fig. 4.5, while the lower part shows the experimental apparatus inside the scattering chamber at INFN-LNL. According to the kinematic calculations, four modules of the detector array EXPADES arranged around the QF angular pairs were used. In order to double the statistics, a symmetrical configuration was chosen.

In the following, a brief description of the electronic chain and the detectors making up the EXPADES telescopes is given.

Ionization Chamber

The first stage of an EXPADES telescope consists in a Frisch Grdid Ionization Chamber. An ionization chamber measures the charge from the number of ion pairs created within a gas caused by incident radiation. It consists of a gas-filled chamber with two electrodes (anode and cathode). A voltage potential is applied between the electrodes to create an electric field in the gas. When the gas between the electrodes is ionized by incident ionizing radiation, ion-pairs are created and the resulting positive ions and dissociated electrons move to the electrodes of the opposite polarity under the influence of the electric field. This generates an ionization current which is measured by an electrometer circuit. The pairs of positive ions and electrons are created in numbers proportional to the deposited energy.

Each ion pair created deposits or removes a small electric charge to or from an electrode, such that the accumulated charge is proportional to the number of ion pairs created, and hence the radiation

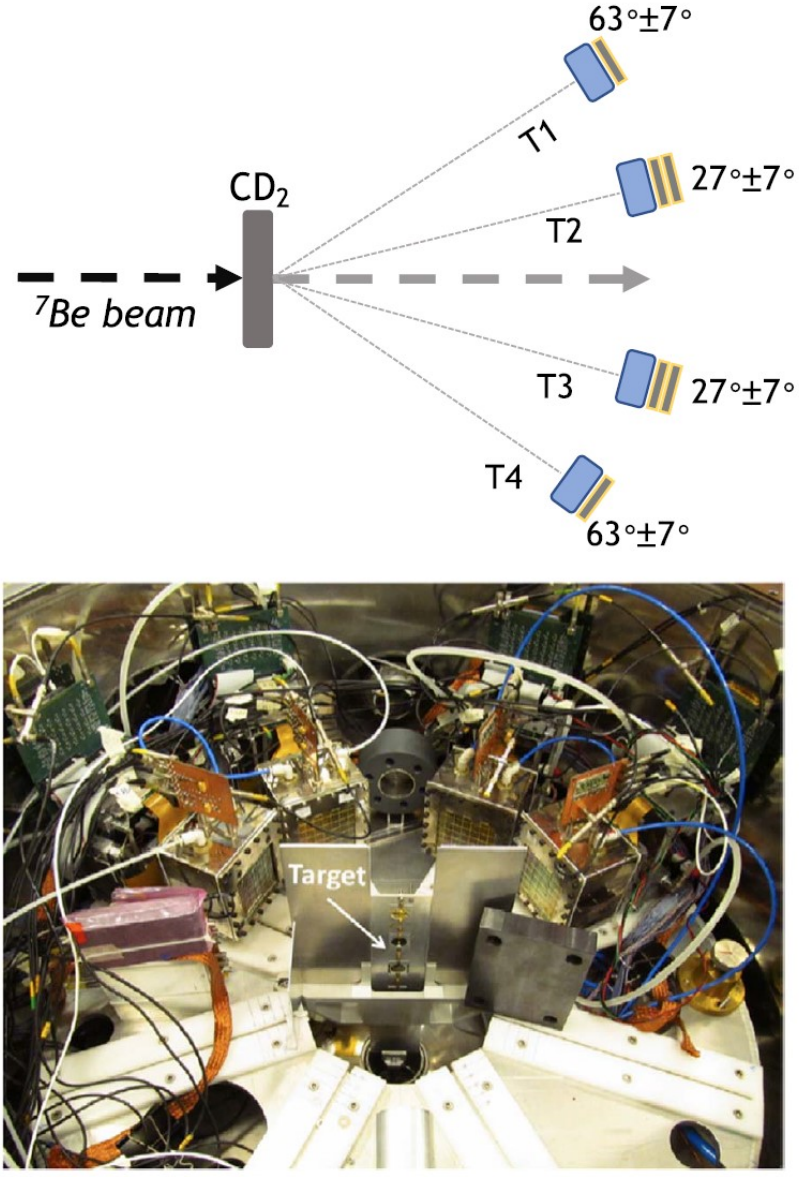

Figure 4.5: Upper part: Schematic drawing of the experimental apparatus adopted for the ^{2}H(^{7}Be,$\alpha\alpha$)p experiment. The light blue rectangles mark the position of the ionization chambers (IC), while the yellow ones mark those of the DSSSDs. Lower part: Displacement of the detection system inside the scattering chamber at the final focal plane of the facility EXOTIC at INFN-LNL.

dose. This continuum generation of charge produces an ionization current, which is a measure of the total ionizing radiation entering the chamber.

Frisch Grid Ionization Chamber [77] are characterized by a counting gas volume and three parallel electrodes: cathode, anode and grid. The grid is positioned between cathode and anode, in order to electrically separate the gas volume in two parts. The grid removes the pulse-amplitude dependence on position of the interaction. it is maintained to intermediate potential and is transparent to electrons. In this way, the incident radiation is directed only into active volume between the cathode and the grid. The signal derives from electrons drift only, so there is not dependence on slow ion motion.

The main advantage in the use of the IC as ΔE stage is that can be handled easily. Moreover, it presents thickness uniformity, the possibility to tune the effective thickness by changing the gas pressure, offers the chance of a large detection surface and does not present radiation damage problems.

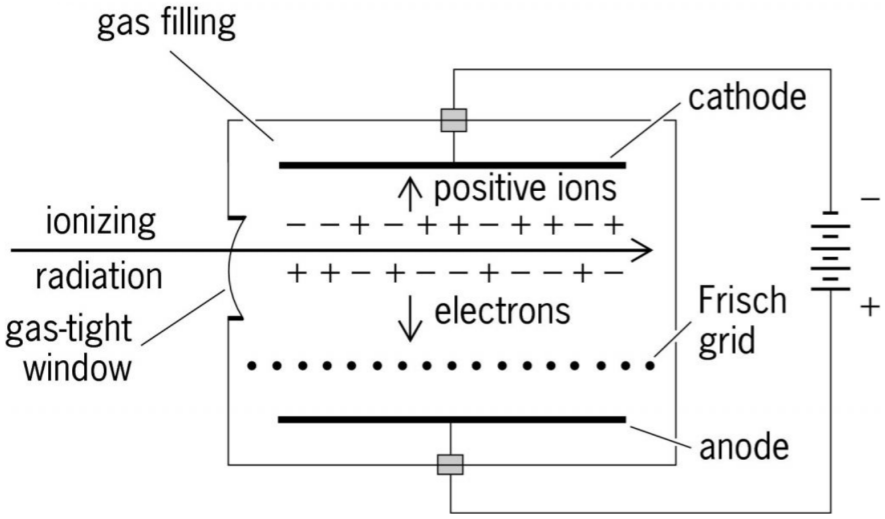

Figure 4.6: Conceptual representation of the operation of an ionization chamber with the Frisch grid.

Each IC is housed in a 100 × 100 × 68 mm^3 chromium-plated brass vessel (see left panel of Fig. 4.7). A 1.5 μm-thick mylar foil, glued on a 1.6 mm-thick fiberglass frame (element 2 in Fig. 4.7, left panel), is used for the 65 × 65 mm^2 entrance and exit windows. The mylar foil is supported by a chromium-plated brass frame on which stretched nylon wires (0.14 mm diameter and 10 mm spacing) are mounted in both the x and y directions (Fig. 4.7 left panel). The wires define an overall geometrical transparency of about 95% (97.5% being the geometrical transparency of each window). The vacuum seal of the IC is made of a 1 mm-thick teflon frame sandwiched between the fiberglass frame, where the mylar foil is glued, and the IC vessel. The IC active depth along the ion direction is 61.5 mm. The active height, i.e. the distance between the cathode and the anode, is 68 mm, 64 mm being the distance between the cathode and the Frisch grid placed in between (right panel of Fig. 4.7). The electrodes are made of 2 mm thick gold-plated copper-coated (40 μm) fiberglass frame and have a surface of 59 × 61.5 mm^2.

The Frisch grid is made of a 50 μm gold-plated tungsten wire mesh with a 4 mm-spacing (both in x and y directions). In order to have a uniform electric field in the active volume, 8 field-shaping guard rings (made of 50 μm-thick gold-plated tungsten wire) at a distance of 8 mm from each other are added while the field uniformity along the incident particle direction is maintained by gold plated copper-coated strips (with 8 mm spacing) on fiberglass frame. The guard rings are connected to a voltage divider chain of 5.6 MΩ resistors. During the experiment, the cathode (anode) bias was -300 (+100) V, while the Frisch grid was at ground. The ICs is filled with isobutane gas continuously maintained at the pressure of about 100 mbar. The gas was chosen for its high electronic stopping power, because it can work with a relatively low gas pressure and for the high electron drift velocity. 1.5 μm thick mylar foils were used as entrance and exit windows. The threshold of $\sim$ 3 MeV introduced by the ICs did not affected the α particle detection at the most backward angles of our detector set-up, and

it did not introduce any threshold for the α particles detected by the telescope at the most forward angles, because kinematical calculations predicted energies higher than 4 MeV.

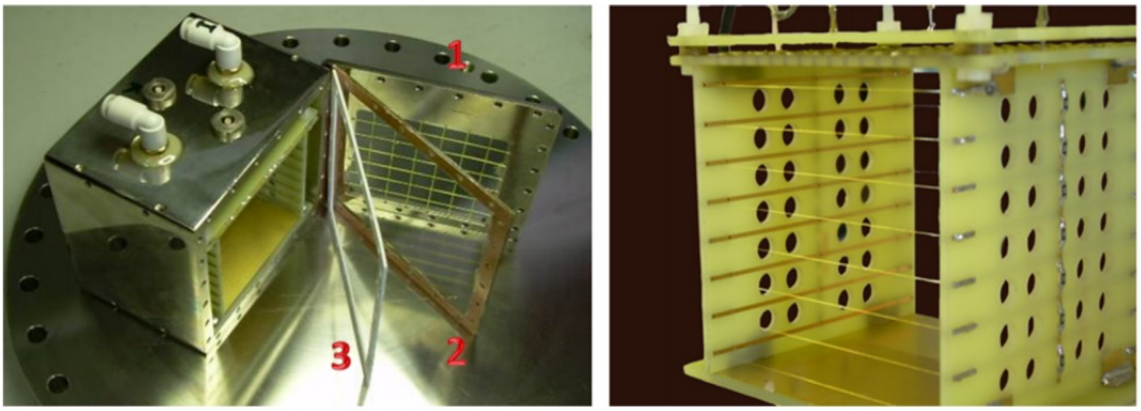

Figure 4.7: Left-hand side: IC and exploded view of the entrance window in order to distinguish the different components. Right-hand side: Electrodes, Frisch grid, field-shaping guard rings and field-shaping guard strips to ensure uniformity of the electric field.

Double Sided Silicon Strip Detector

The DSSSD belongs to the large class of semiconductor detectors. In the following, a brief description of the properties of these detectors will be given. A semiconductor detector (Fig. 4.8) is basically an inversely polarized $p-n$ junction, where the depletion layer around the junction, the zone without intrinsic charge carriers, represents the active volume of the detector. When the radiation impinges on the detector, there is a promotion of the lattice electrons from the valence band to the conduction band, resulting in the creation of electron-hole pairs. Those pairs then drift toward the electrodes thanks to the presence of an electric field inside the junction. During their motion they induce a current on the electrodes, whose expression can be calculated for each time instant via Ramo's theorem, generating the final signal.

Each side of the DSSSD has 32 strips, it is placed at a distance of about 24 cm from the target and have an active area of 64 $\times$ 64 mm^2. The strips of the front (y) side are oriented orthogonally to the ohmic strips of the back (x) side, defining thus a 4 $\times$ 4 mm^2 pixel structure thus introducing an angular resolution of about 0.9° (FWHM). The strips are 64 mm long, with 2 mm pitch size and 40 μm inter-strip separation. In Fig. 4.8 (right panel) it is possible to observe a DSSSD with the connecting cables.

A standard three-peak (^{239}Pu–^{241}Am–^{244}Cm) α source was used for the energy calibration of the DSSSD as well as devoted run measurements using a 10 MeV and 24 MeV ^{7}Li beam impinging on carbon and CH_2 targets to induce the α-producing reactions ^{12}C(^{7}Li,α)^{15}N, ^{1}H(^{7}Li,α)^{4}He.

PAD

The PAD detector consists of a DSSSD described above, with the difference that all the strips are short-circuited at the entrance of the preamplification stage, so that only one signal in output from the detector is read. We just recall the detector thickness of 300 μm and the active area of 64 mm $\times$ 64 mm.

4.4.1 Electronic chain

In this paragraph we briefly present the electronics readout employed for the treatment of the signals collected by the different detectors. We remark that essentially all modules were home-made, developed, designed, built and commissioned by the collaboration EXOTIC over several years. We describe here only the main features of the electronic boards and modules. For more details please refer to [78].

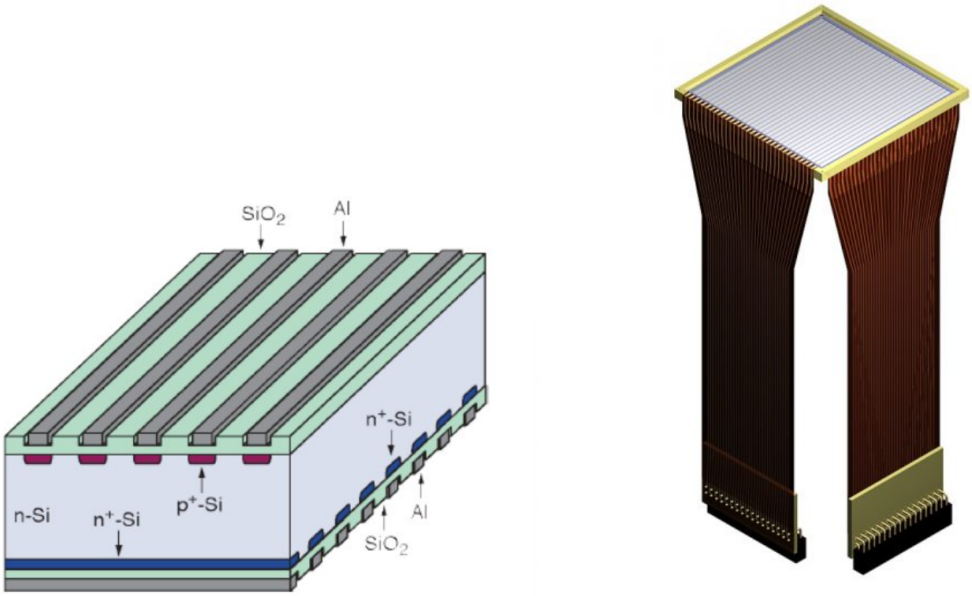

Figure 4.8: Conceptual drawing of a semiconductor detector (left panel) and a representation of a DSSSD with the connecting cables in the right panel.

Preamplifiers

The IC anode signal is sent to a custom low-noise charge-sensitive preamplifier (see Fig. 4.9), mounted directly on the IC vessel under vacuum in order to reduce background sources, thus increasing the signal-to-noise ratio.

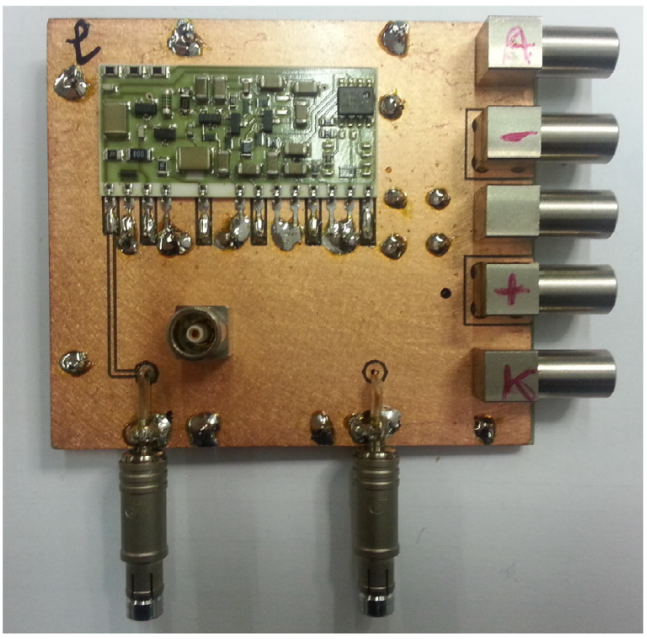

Figure 4.9: Low-noise charge sensitive preamplifier for the IC detector.

Regarding the DSSSD, a 16-channel custom low-noise charge sensitive preamplifier was used (Fig. 4.10). The detector front and back sides are connected to the electronic boards with kapton cables that are flexible and designed in order to have a low capacitance and ground shielding. The kapton cable ends with a finger that plugs directly into the connector on the preamplifier board. To maintain low the cost of the electronics, the 32 strips of each DSSSD side were reduced to 16 by short-circuiting two-by-two adjacent strips. The outputs of the preamplifiers were then connected to the flange of the

reaction chamber to the signals outside for further processing.

Figure 4.10: Low-noise charge sensitive preamplifier for the DSSSD detector.

As said before, the PAD is essentially a DSSSD detector, whose strips were short-circuited at the entrance of an additional home-made preamplifier, located under vacuum in the proximity of the detector. Then, the preamplifier output signals are taken outside the reaction chamber for an additional amplification stage.

MEGAMP

The 16 differential output signals coming from the preamplifier boards of the DSSSD modules, ICs and PADs are processed by a specifically designed amplifier module called MEGAMP [78]. This module provides information such as the energy, timing and the pulse shape analysis. The MEGAMP is a single NIM module were 16 channels are housed. Each channel can be divided in two sections related to the energy and the time parameters. The energy section is composed essentially of a spectroscopy amplifier that accepts differential input signals. The timing section provides both time and pulse shape information. It consists of two Constant Fraction Discriminators (CFDs) that are set to give an output signal at 30% and 80% of the signal leading edge and a Time-to-Amplitude Converter (TAC) circuit. . 4.11 shows a MEGAMP and the block diagram of one channel of the module. The differential receiver in the first stage transforms the differential input signal into a single ended one. From the figure it is possible to notice that the timing stage is composed of a circuit for the time shaping and of a fast amplifier with two selectable gains. The 30% CFD is used to provide a good time information while, the 80% CFD is used for the pulse shape discrimination. The energy stage starts with two circuits able to handle the input signals from different type of detectors. The first circuit is optimized for signals coming from charge-sensitive preamplifiers. The circuit is composed of two CR circuits giving the signal derivative with a pole zero compensation. The second circuit, for fast unipolar signal, consists of an approximate integrator without a pole zero compensation.

ADC

A custom single-slot VME card has been developed to digitize the multiplexed analog signals coming out from the MEGAMP modules. The ADC card consists of 8 analog differential signal receivers and 8 12-bit ADC-chip converters that sample the input signal with a 50 MHz frequency. The use of a high sampling rate enables the determination of when the multiplexed signal is stable enough to be acquired. With the arrival of an external trigger, the control logic starts the conversion sequence. After a programmable delay time the hold signals are sent to the MEGAMP modules in order to capture the maximum of a Gaussian peak. At this point, the ADC card generates the logic signal to

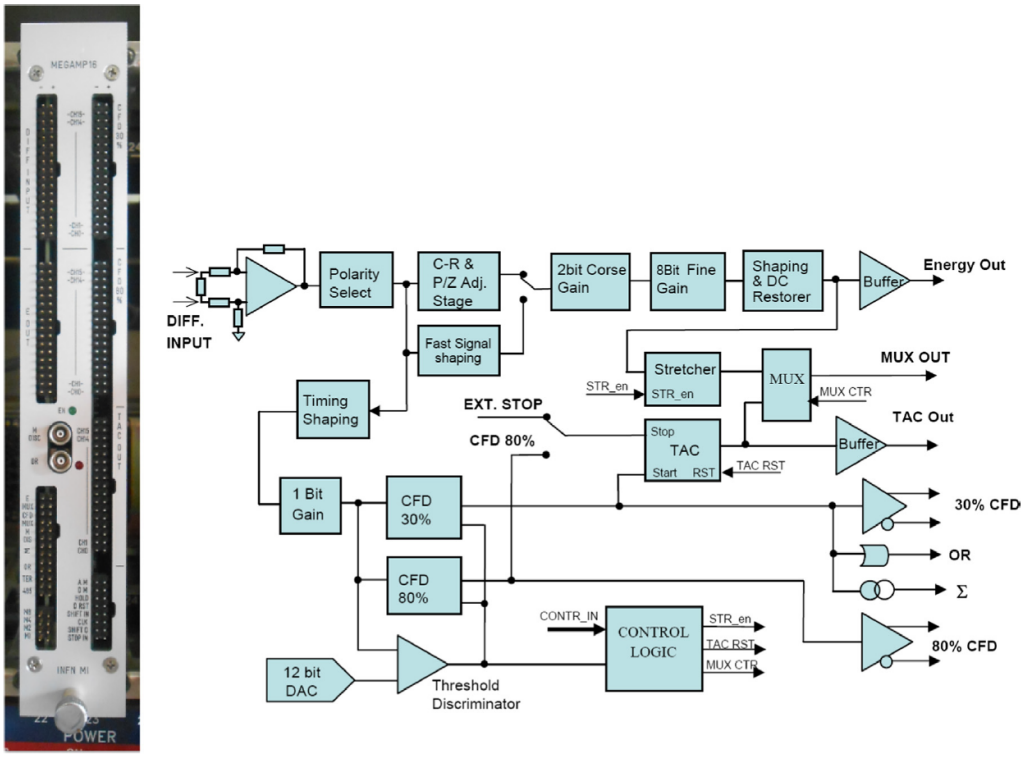

Figure 4.11: MEGAMP (left) and block diagram of a single channel of the MEGAMP (right).

bring out in sequence the 32 amplitudes captured by the hold circuit and acquires them by means of an ADC-chip with a sampling rate of 50 MHz. A FPGA is then used to handle the card with the 8 ADC-chips.

TSB

The Trigger Supervisor Board (TSB) is a general purpose custom VME-standard card. It accepts up to 64 differential input channels for the proposed trigger signals originating from the different detectors and handles the trigger logic of the whole experimental set-up. The width and delay of each proposed trigger signal in the input can be modified to compensate for the different ToF of the detected particles, the different time response of the detectors and the different cable delays. The trigger of our experiment was provided by the OR signal of the DSSSD modules of the various telescopes, whereas the IC and PAD modules acted as slave channels.

CHAPTER 5

Data analysis

In this section, I will illustrate all the steps taken, applying the THM, in order to derive the cross section for the reaction ^{7}Be$(n,\alpha)^{4}$He. In particular, I will explain in detail the procedures, the ROOT C++ macros [79] developed to analyze the data and the results, giving a clear overview of the logical and computational processes that were necessary to reach the final result. Below, a summary list of the various steps carried out, which will be discussed in more detail in the appropriate sections, is reported:

- Energy calibration;
- Selection of the events from ^{7}Be$(n,\alpha)^{4}$He;
- Q_{value} determination;
- Evidence of the QF mechanism and discrimination of the sequential mechanism using the impulse distribution;
- Extraction of the differential cross section using the kinematical factor and the impulse distribution;
- Interpretation of the results obtained and conclusions.

Four telescopes were used during the experiment in order to have a double chance to intercept $\alpha - \alpha$ coincidences and thus double the gathered statistics. The data analysis of the coincidences detected by telescopes T2(B) and T4(D) has been already discussed and published in the work of L. Lamia et al. [80]. My work, on the other hand, concerns the data analysis of the pair of homologous telescopes T1(A) and T3(C), in the following simply called A and C, respectively. The ultimate goal will be to sum up the statistics collected by both pairs of telescope to decrease the statistical uncertainty.

5.1 Energy calibration

The first step of data analysis was the energy calibration of telescopes A and C. The calibration was performed for each individual horizontal and vertical strip for both telescopes. Different α sources and reactions were used to calibrate the telescope strips in combination with different experimental set-up configurations. In particular, the following situations were considered:

- three peak α-source with a 5.16 MeV (^{241}Am), 5.48 MeV (^{244}Cm) and 5.80 MeV (^{239}Pu) on all telescopes without the IC (3 calibration points, Fig. 5.1),

- three peak α-source with a 5.16 MeV (^{241}Am), 5.48 MeV (^{244}Cm) and 5.80 MeV (^{239}Pu) on all telescopes with the IC installed but without any gas pressure inside (3 additional calibration points),
- three peak α-source with a 5.16 MeV (^{241}Am), 5.48 MeV (^{244}Cm) and 5.80 MeV (^{239}Pu) on all telescopes with the IC filled with a gas pressure of $\sim$ 90mb (3 more calibration points),
- Beam of ^{7}Li^{++} at 10 MeV on ^{197}Au (200 μg/cm^2) (1 further calibration point from the elastic scattering process),
- Beam of ^{7}Li^{++} at 24 MeV on ^{197}Au (200 μg/cm^2) (1 final calibration point again from the the elastic scattering process).

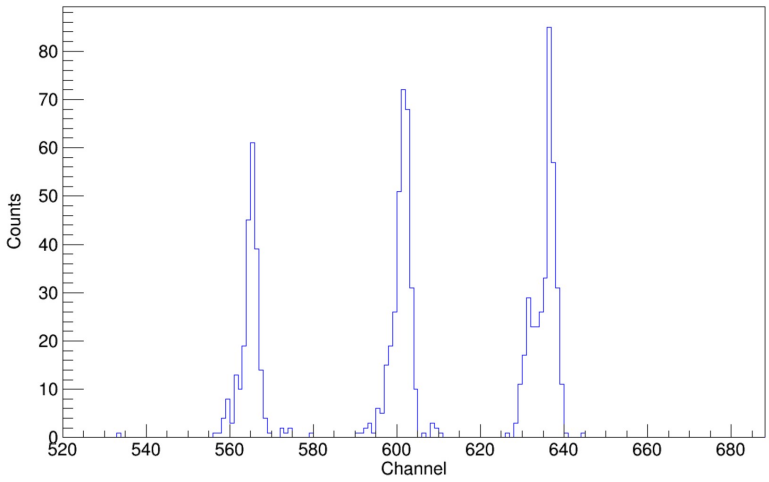

Figure 5.1: Example of calibration peaks for a C-telescope strip. A three peak α-source with a 5.16 MeV (^{241}Am), 5.48 MeV (^{244}Cm) and 5.80 MeV (^{239}Pu) was employed in this example. These peaks were then fitted with a Gaussian function and from the calculation of the centroids the calibration line was derived.

In particular, due to the high beam energies, elastic scattering events of ^{7}Li ions on ^{197}Au at 10 and 24 MeV provide very useful reference points for the calibration of the high energy region of our spectra. In this way, 11 calibration points were obtained for each vertical and horizontal strip (Fig. 5.2). Assuming that the existing proportionality between the height of the signal produced by the incident particle on the detector and the number of channels of the ADC associated with, it is not disturbed by non-linear effects introduced by the acquisition electronics, for each strip then, a linear fit was performed with equation

$$E(MeV) = m * E(ch) + q \tag{5.1}$$

with the experimental energies (in channels) on the x-axis and the estimated energies (in MeV) on the y-axis.

Knowing the width of the peak (σ_x) and m, the energy resolution (FWHM) can be obtained in this way:

$$\sigma_E = m\sigma_x 2\sqrt{2ln2} \tag{5.2}$$

In our case, a typical energy resolution of about 55 keV for the 5.16 MeV α particles (^{241}Am) was obtained for the DSSSD modules.

The expected energies to be associated to the calibration point obtained from elastic scattering measurements were estimated from the kinematics and were derived (using the software LISE++ [81]) subtracting the energy lost by the beam in half of the target thickness (i.e., assuming the reaction to occur at mid-target position). It follows that the effective beam energy (from now on called initial energy) will be $E_{eff} = E_{beam} - \Delta$E, where ΔE indicates the loss of energy at half target and E_{beam} the incident beam energy. During the measurement, runs with the ^{7}Be beam impinging on a thin gold target at deep sub-barrier energy were performed to monitor the energy beam, which remained basically constant throughout the entire experiment.

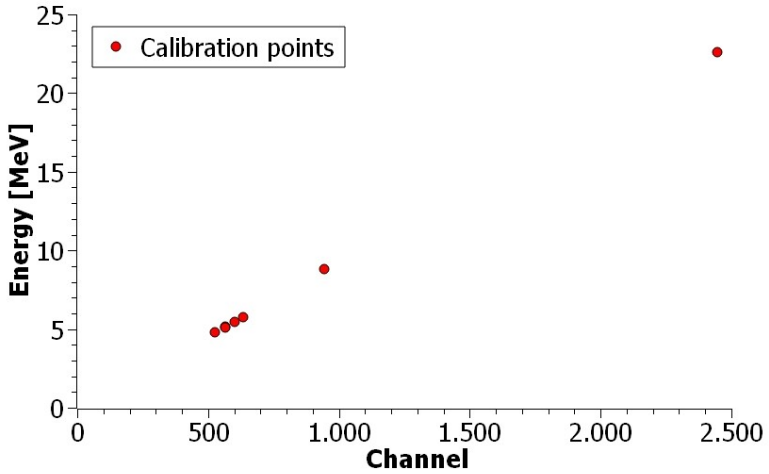

Figure 5.2: Example of the calibration points for a single horizontal strip of the telescope C. The points are associated to a three peak α-source with a 5.16 MeV (^{241}Am), 5.48 MeV (^{244}Cm) and 5.80 MeV (^{239}Pu) respectively without the use of the IC in the experimental set-up 5.1; the same source but with the IC without gas; the three peak α-source with the IC filed with gas at $\sim$ 90 mbar; the points of the scattering ^{7}Li on ^{197}Au target (E_{beam} = 10 MeV and 24 MeV). In total 11 calibration points were therefore obtained.

A C++ macro was developed in order to calibrate the energies and to obtain, from the raw data, the necessary kinematical variables for the subsequent data analysis.

In order to verify the goodness of the whole calibration procedure, we considered the kinematic locii for the ^{7}Li + ^{197}Au and the ^{7}Li + ^{12}C reactions. In particular, E$-\theta_{lab}$ 2D-correlation plot for the two telescopes A and C were created. These plots are characterised by the presence of a clearly visible and intense line corresponding to elastic scattering events and in the figure for the ^{7}Li + ^{12}C reaction it is possible also to distinguish several other lines corresponding to the inelastic scattering process with the population of different exited states, as reported in fig 5.3. The coloured lines superimposed on the plots were obtained using the program LISE++ [81]. In the calculations, we also accounted for the energy lost by the emerging particles, due to the variation of the target thickness crossed by the reaction products according to emission angle, in the two mylar windows of the ionization chambers and in the gas region of the chambers themselves.

Fig. 5.3 shows the good superposition between the experimental and estimated kinematic lines in all the situations. In particular, it can be seen that the calibration was carried out correctly and therefore, once this aspect was verified, it was possible to continue with the subsequent steps of data analysis.

5.2 Event selection

After calibration, the next step in the typical Trojan Horse analysis is to select the particular reaction channel of interest, i.e. to select the events associated with the three-body reaction ^{2}H(^{7}Be,$\alpha\alpha$)p in the final state. For this purpose, the events characterised by the presence of two coincident α particles must at first be selected. After this, all kinematic variables of interest obtained from the macro were compared with the simulated ones.

The selection of the events of interest was performed using the $\Delta E - E$ identification method, already introduced in Sec. 4.3.1.From the study of the ΔE–E correlations plot of interest (see, for instance, Fig. 5.4), it was possible to identify the revealed particles according to their charge, and later by means of graphical cuts performed with ROOT [79] the events corresponding to $Z = 2$ were selected. Fig. 5.5 shows a few typical examples of the graphical selections and give an idea about the degree of separation between locii corresponding to different atomic numbers.

Fig. 5.4 illustrates that ΔE–E plots were constructed for both telescope A (right panel) and C (left

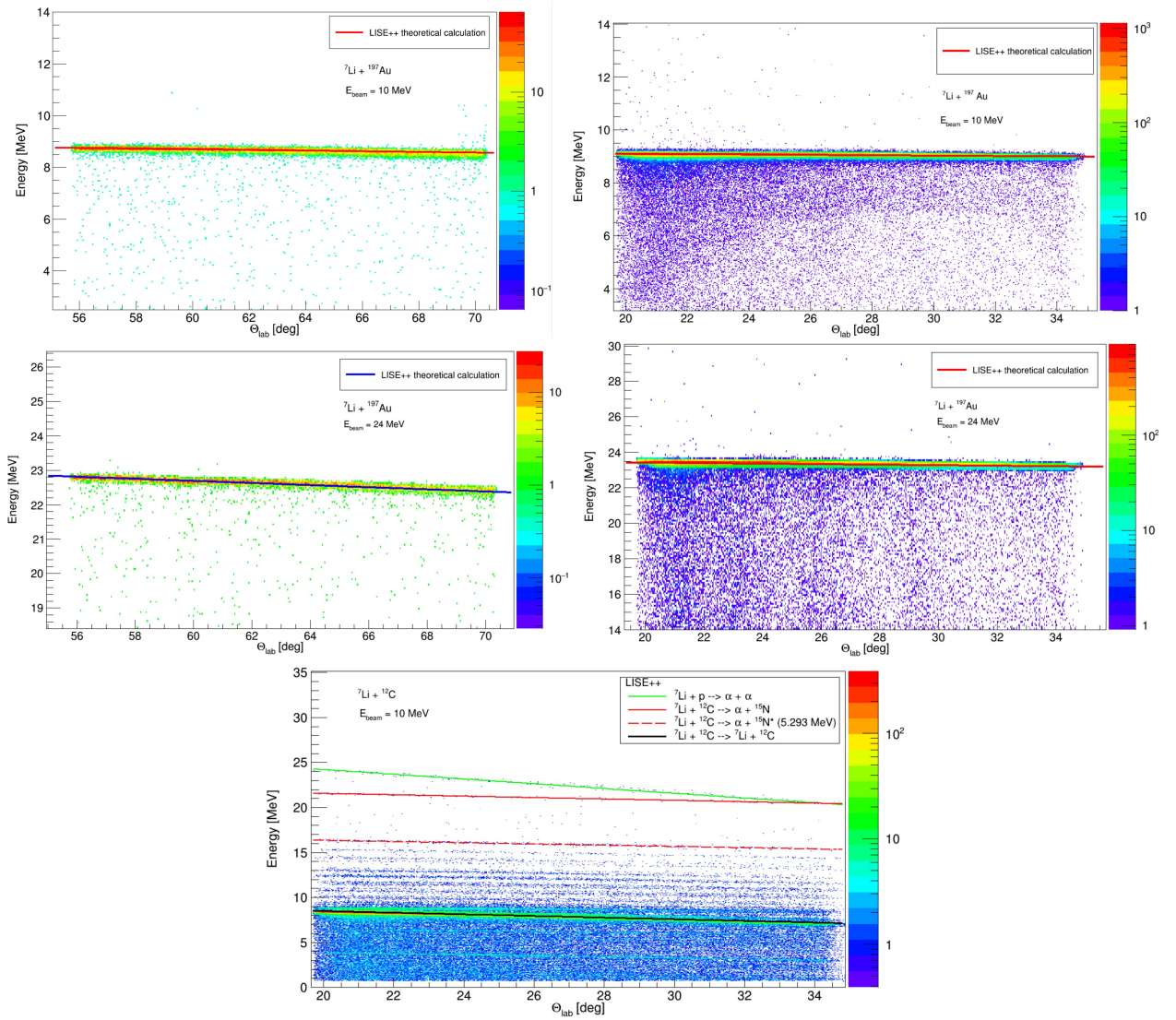

Figure 5.3: Comparison between the kinematic lines obtained from the reactions ^{7}Li + ^{197}Au and the ^{7}Li + ^{12}C for telescopes A and C and those calculated using the LISE++ [81] for the following processes: elastic scattering (black line) inelastic scattering (red lines) and for the transfer (green line).

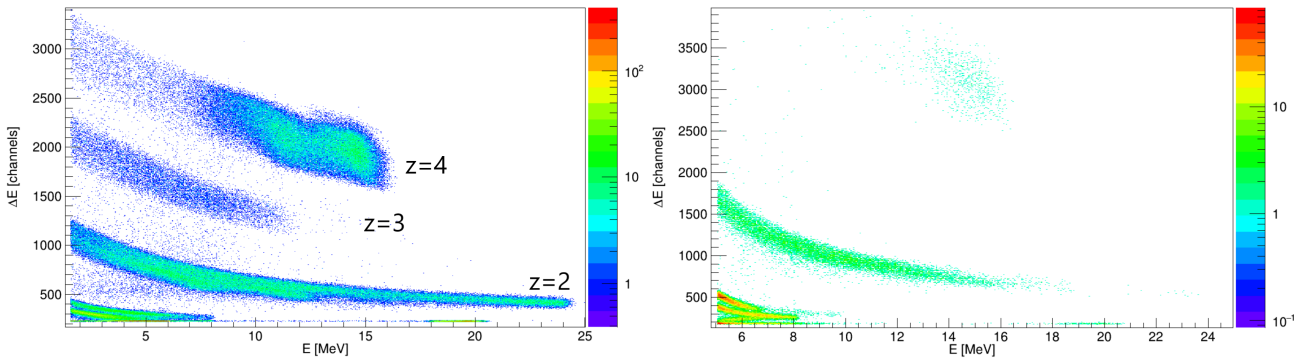

Figure 5.4: Experimental ΔE–E plots for telescope C (left panel) and A (right panel). The $Z = 2$ locus corresponds essentially two α particles. The $Z = 4$ locus represents the scattered beam on the CD_2 target.

panel) using the IC as ΔE stage and the DSSSD as residual energy stage. In this way it was possible to select all α particles stopping in the DSSSD layer, i.e. approximately up to an α kinetic energy of 25 MeV. Moreover, being C a triple telescope, it was possible to construct an additional ΔE–E plot (shown in the lower panel of Fig. 5.5) using the DSSSD as ΔE stage and the PAD as residual energy stage. This further plot was helpful to discriminate more energetic (energy larger than 25 MeV) α particles, crossing entirely the DSSSD and stopping in the PAD. Moreover, Fig. 5.5 clearly shows that, being both the DSSSD and the PAD solid-state detectors, their corresponding ΔE–E plot (lower panel) is characterized by a much better energy resolution and therefore separation quality than the plots in the upper panels, which make use of the IC as ΔE stage.

As mentioned before, we selected events corresponding to $Z = 2$. These events are made up by both ^{4}He and ^{3}He particles. As a consequence, at this point of the analysis, we cannot be sure that we are going to select only α particle. However, this will not be a problem because, in the subsequent data analysis, we will impose much more stringent conditions: only events in coincidence between the two telescopes will be considered and, in addition, a condition on the overall Q_{value} will also be imposed. For these reasons, at the end the possible pollution due to ^{3}He into the data of interest will be at most negligible.

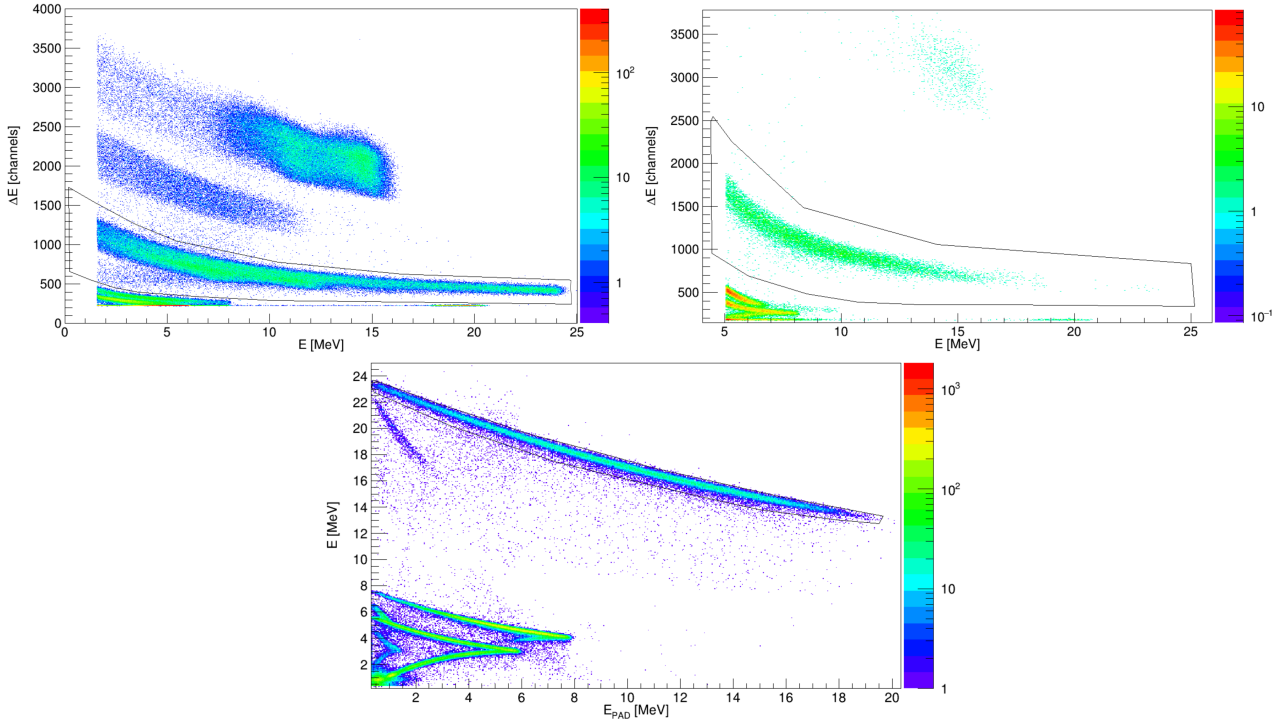

Figure 5.5: Graphical selection on the Experimental ΔE–E plots constructed for both telescope A (right panel) and C (left panel) using the IC as ΔE stage and the DSSSD as residual energy stage. While, for the telescope C, the DSSSD was used as ΔE stage and the PAD as residual energy stage (lower panel). The graphical cuts adopted for the selection of the $Z = 2$ locus have been highlighted in all plots.

After selecting the events of interest, we checked the correctness of the data sorted by the macro and also verified the right correlation between the energy information registered by the strips of the x-side and y-side of the two DSSSDs. For this purpose, we created the correlation plots E_y *vs* E_x, where E_x and E_y are the sum of all the energies detected by horizontal (x) and vertical (y) strips of each DSSSD, respectively. These plots are shown in Fig. 5.6.

Once these plots were created, we graphically selected the events along the diagonals. These events correspond to those where we have an unambiguous matching between the energies recorded by the x-side and the y-side and are those the will be considered in the further steps of the analysis to derive the kinematical variables and the cross sections. By visualising the left panel of Fig. 5.6, it is possible to notice that the DSSSD of the telescope A is characterized by a shift of 200 keV between the energy measured by the x-side with respect to the correspondent on the y-side. This effect is associated only

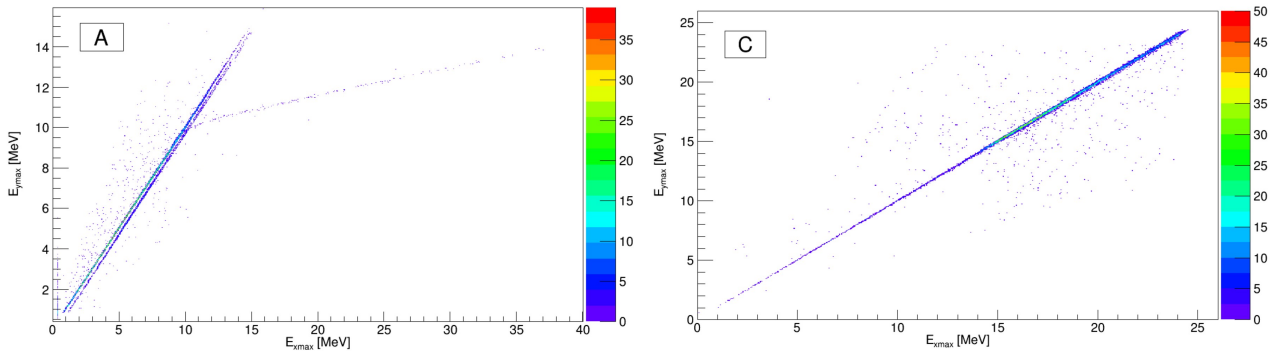

Figure 5.6: Correlation plots E_y *vs* E_x for the DSSSD of telescope A (left panel) and C (right panel). E_x and E_y are the sum of all the energies detected by horizontal (x) and vertical (y) strips of each DSSSD, respectively. It is possible to appreciate two features in the plot for telescope A: (i) the x strips 0, 2 and 4 are characterized by a shift of $\sim$ 200 keV between the energy of the x-side with respected for corresponding of the y-side; (ii) a deviation from the diagonal for strip $x = 4$. See text for additional details.

to the x strips 0, 2, 4. In this case, we considered the average of the energies E_x and E_y for the subsequent data analysis. Additionally, a deviation from the diagonal can be appreciated in the left panel of Fig. 5.6. After a careful investigation of the problem, we realized that only the strip $x = 4$ was responsible for this anomalous behavior. In this case, instead of averaging the two energies E_x and E_y, only the energy of the corresponding strip E_y was considered. The telescope C did not manifest any particular problems and, after a graphical selection of the events along the diagonal line, we performed an average of the energies E_x and E_y.

5.2.1 Q_{value}

After selecting the events characterized by the presence of the two α particles in coincidence in the output channel of the reaction and once the energies and the angles of the detected α particles were determined, a complete reconstructed of the three-body kinematics was performed by adopting the energy-momentum conservation laws. This allowed us to completely reconstruct the kinematical properties of the undetected proton.

For the selected events, at first the experimental Q_{value} was derived, showing an isolated peak reported in Fig. 5.7.

$$Q_{value} = E_{\alpha 1} + E_{\alpha 2} + E_p - E_{beam} \tag{5.3}$$

where E_p is reconstructed from energy and momenta conservation laws.

Fig. 5.7 shows the experimental spectrum of the Q_{value}. A Gaussian fit of the experimental data led to the value of 16.66 $\pm$ 0.01 MeV in agreement with the expected Q_{value} for the three-body reaction of interest, i.e. ^{2}H(^{7}Be,$\alpha\alpha$)p (Q_{value}= 16.76 MeV). The FWHM of the Q_{value} spectrum ($\sim$ 2 MeV) reflects the straggling due to the target thickness, the energy spread due to the secondary beam production and the angular resolution of the detector setup.

Since the Q_{value} is independent from the kinematic variables of the reaction, a further verification of the Q_{value} was performed in order to cross-check the accuracy of the energy calibration procedure. We tested whether there are any correlations between the Q_{value} itself and any kinematic variable, for example the particle emission angles θ. The $\theta - Q_{value}$ correlation plot shown in Fig. 5.8 for all the pairs of detectors displays that there is no correlation between the Q_{value} and the kinematic variables and that, once again, the events are distributed around the experimental value of $\sim$ 16.7 MeV.

As mentioned, the experimental setup allows the detection of two of the three emitted particles. Therefore, the energy and the emission angle of the undetected particle were reconstructed event by event by applying the conservation principles, under the assumption that its mass is 1 (in this case a proton). The experimental verification of this hypothesis was performed by studying the so-called

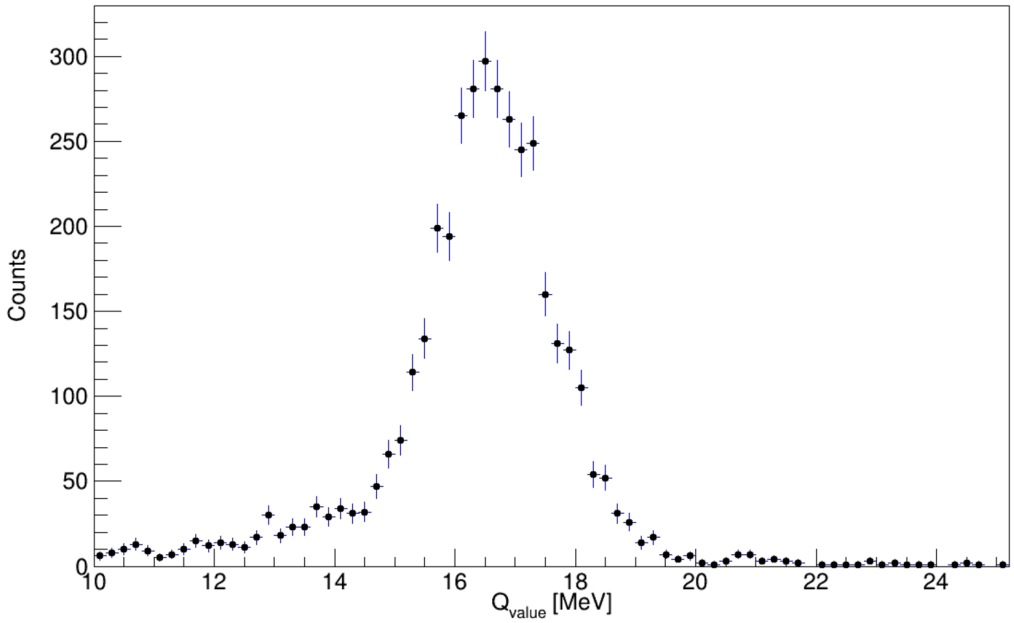

Figure 5.7: Experimental Q_{value} spectrum for the ^{2}H(^{7}Be,$\alpha\alpha$)p selected events, with the corresponding statistical error bars. The spectrum is centered at 16.66 MeV with a FWHM of $\sim$ 2 MeV.

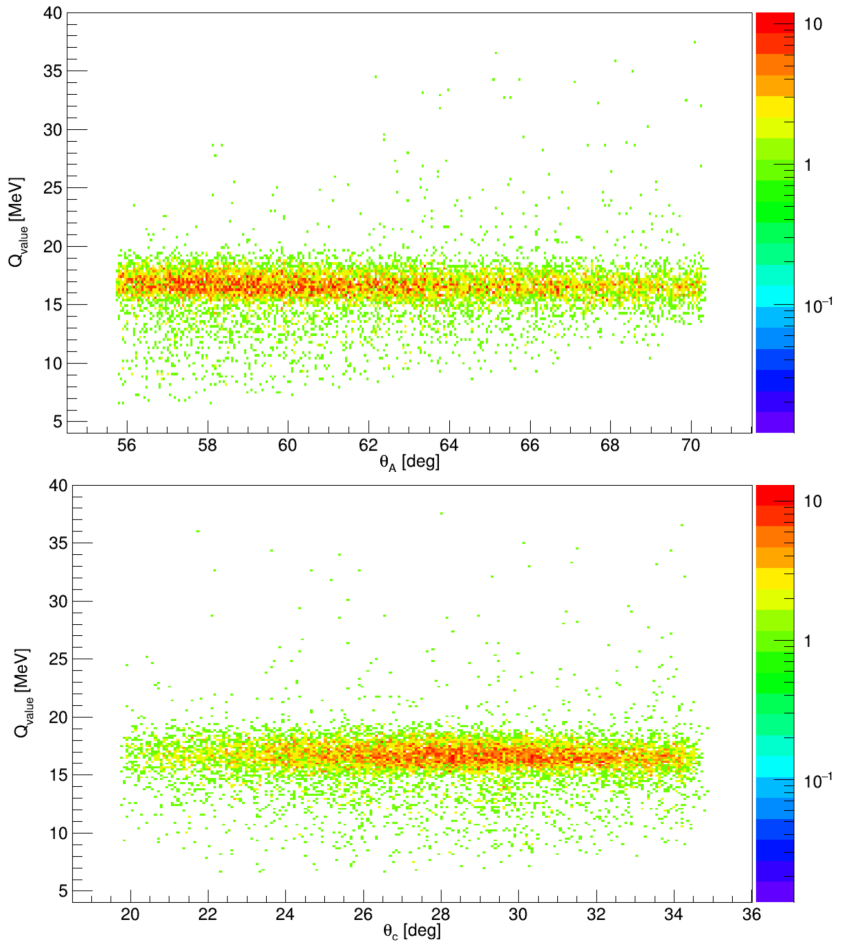

Figure 5.8: $\theta - Q_{value}$ correlation plot for the telescope A (upper panel) and B (lower panel). It is possible to clearly appreciate the expected independence between the two variables.

"Romano $x - y$ plot"[1] defined in Ref. [82] as:

$$y = E_{beam} - E_{\alpha 1} - E_{\alpha 2}; \qquad x = \frac{p_p^2}{2u} \tag{5.4}$$

where u is the atomic mass unit expressed in MeV/c^2. A plot of the data using these parameters is shown in Fig. 5.9. It is immediately noticeable how the events are arranged along a straight line that can be parametrized as [82]:

$$Y = \frac{1}{A_p} X - Q_{value} \tag{5.5}$$

where A_p is the mass of the third particle (proton). The intercept of this line corresponds to the experimental Q_{value}, ~ 16.7 MeV. This outcome suggests that the calculation of the kinematic variables and the reconstruction of proton kinematics were successfully performed.

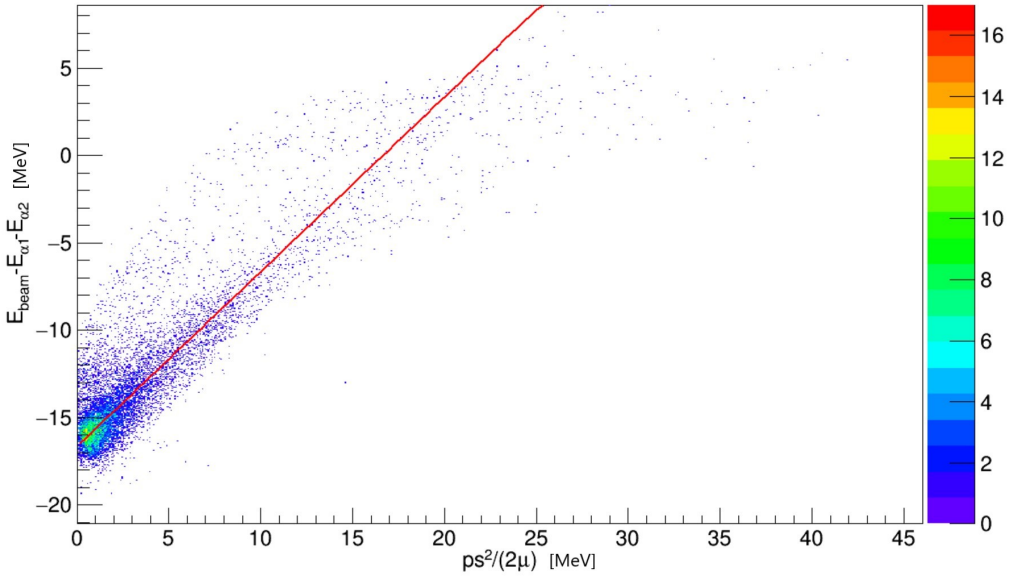

Figure 5.9: Identification of the spectator particle in accordance with the procedure described in Ref. [82]. The intercept of this line ($x = 0$) corresponds to the experimental Q_{value}, 16.67 MeV. See text for additional details.

To further constrain the selection of the reaction channel, the experimental energies, $E_{\alpha 1}$ and $E_{\alpha 2}$, of the two α particles detected in coincidence were compared with those obtained from a dedicated simulation for the angular window $\theta_{\alpha 1} = 27° \pm 1°$ and $\theta_{\alpha 2} = 63° \pm 1°$. The comparison was performed by relating the two energies, $E_{\alpha 1}$ *vs* $E_{\alpha 2}$,and applying also an additional window of $\pm 1\sigma$ around the mean value of the Q_{value} spectrum. Fig. 5.10 shows the comparison between the experimental energy values (red points) and the simulated ones (black points). The comparison, strongly confirms the reaction channel selection, as well the absence of contaminations from other reaction channels.

An additional proof that we are selecting the proper channel is presented in Fig. 5.11, where we considered an angular range different from the condition of QF angles. In particular, it is evident that as we move away from the condition of QF angles by an ever-increasing amount, the experimental points become in disagreement with the simulated ones. This is a strong evidence that we correctly selected the channel of interest.

Fig. 5.12 shows the correlation plot $E_{\alpha\alpha} - p_s$ between the α particles relative energy and the proton momentum distribution. The experimental events (red points) are compared with the simulated one (black points). This plot is of fundamental importance for the subsequent data analysis process. The good agreement between experimental and simulated events and the presence of a thickening of events

[1] Named after the eminent nuclear astrophysicist of the University of Catania Prof. Stefano Romano.

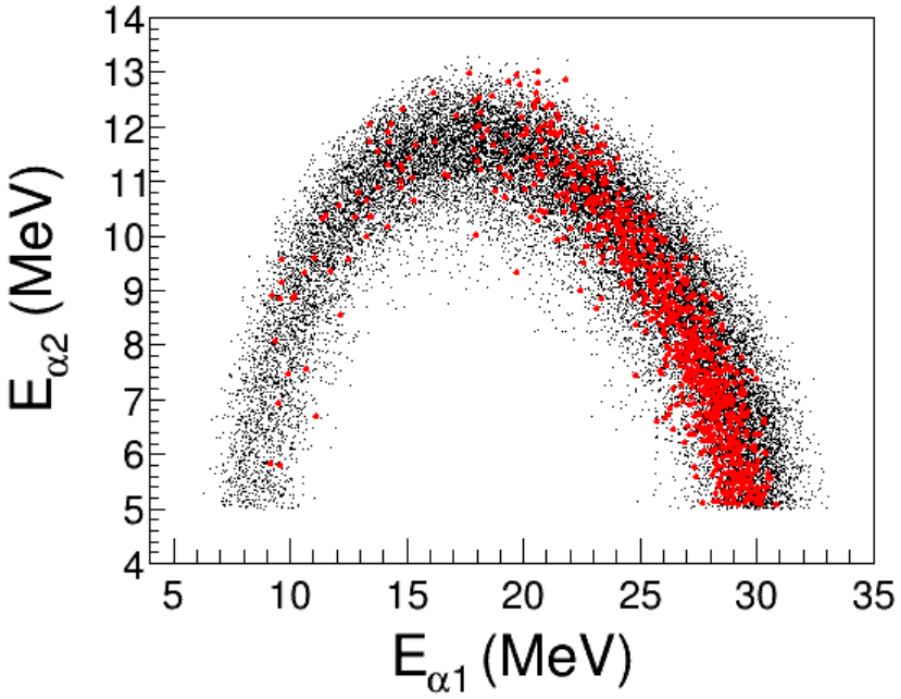

Figure 5.10: Experimental kinematical locus for the ^{2}H(^{7}Be,$\alpha\alpha$)p events (red points) compared with the simulated one(black points). We selected a QF angular range of $\theta_{\alpha 1} = 27° \pm 1°$ (horizontal axis) and $\theta_{\alpha 2} = 63° \pm 1°$ (vertical axis).

at about $\sim$ 17 MeV (^{8}Be excitation energy) is indicative of the right selection of the channel of interest. In particular, the structure at $\sim$ 17 MeV is a clear signature that we are feeding the ^{8}Be exited states associated to the QF process. In the next section the meaning and importance of this plot will be explained in more details. The asymmetry of the relative energy events distribution shown in Fig. 5.12 is given by the arrangements of the two detectors A and C inside the reaction chamber. For example, in the case of α particles detected by the telescopes B and D, the same correlation plot would have shown a mirror situation. The sum of the two components would restore the symmetry and improve the comparison between experimental and simulated data.

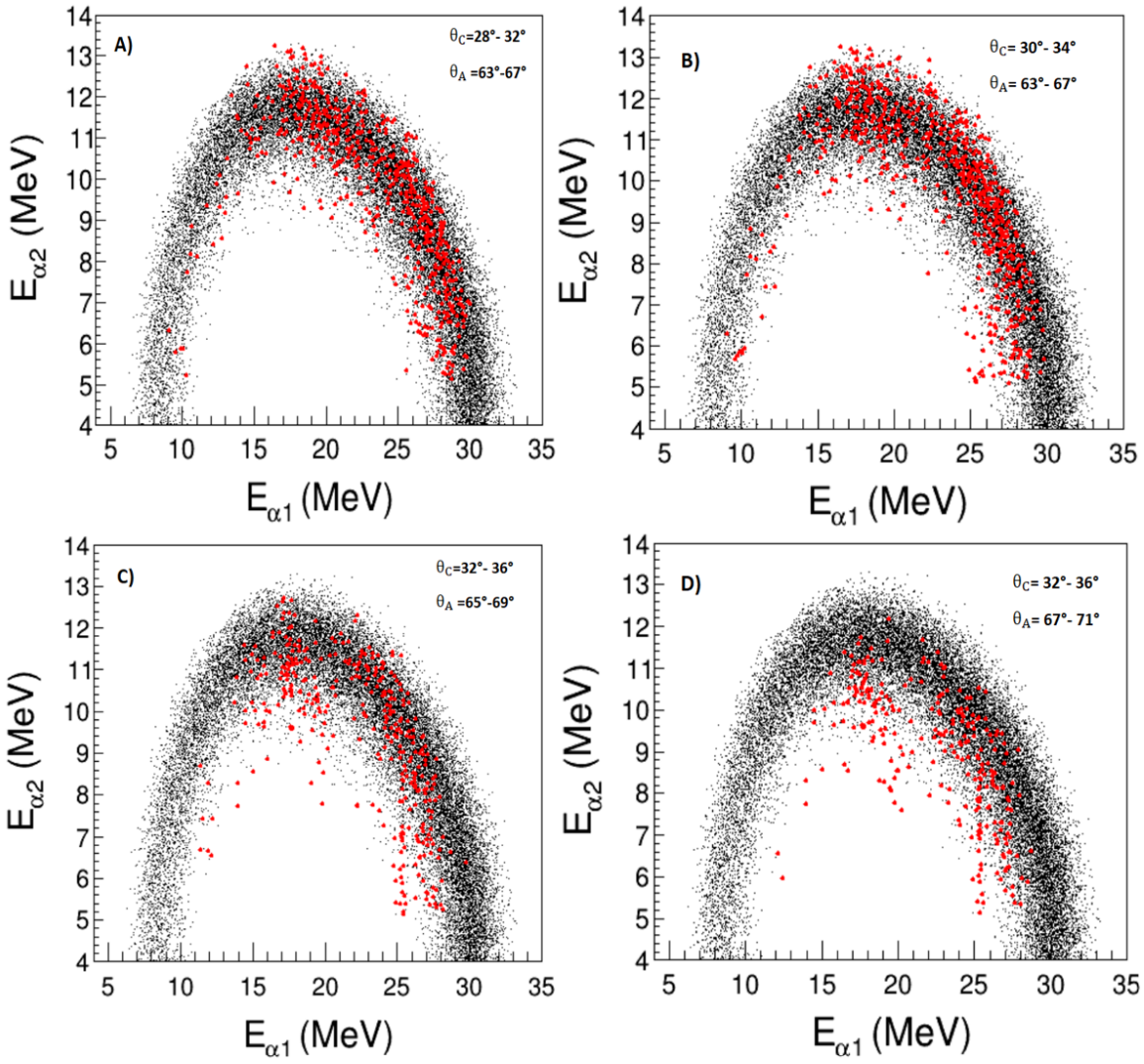

Figure 5.11: Kinematic locus of the telescope pair A-C as the angles subtended by the detectors vary. The black dots represent the simulation corresponding to the QF angles, and the red dots are the experimental points obtained for angles other than the QF condition. Panel A refers to an angular range of the two detectors of θ_C = 28° - 32° and θ_A = 63° - 67°. Panel B of θ_C = 30° - 34° and θ_A = 63° - 67°. The Panel C angular range is θ_C = 32° - 36° and θ_A = 65° - 69° while panel D is defined for θ_C = 32° - 36° and θ_A = 67° - 71°. As we move from panel A to D the angular range deviates more and more from the QF range and, consequently, the difference between experimental and simulated data gets larger and larger.

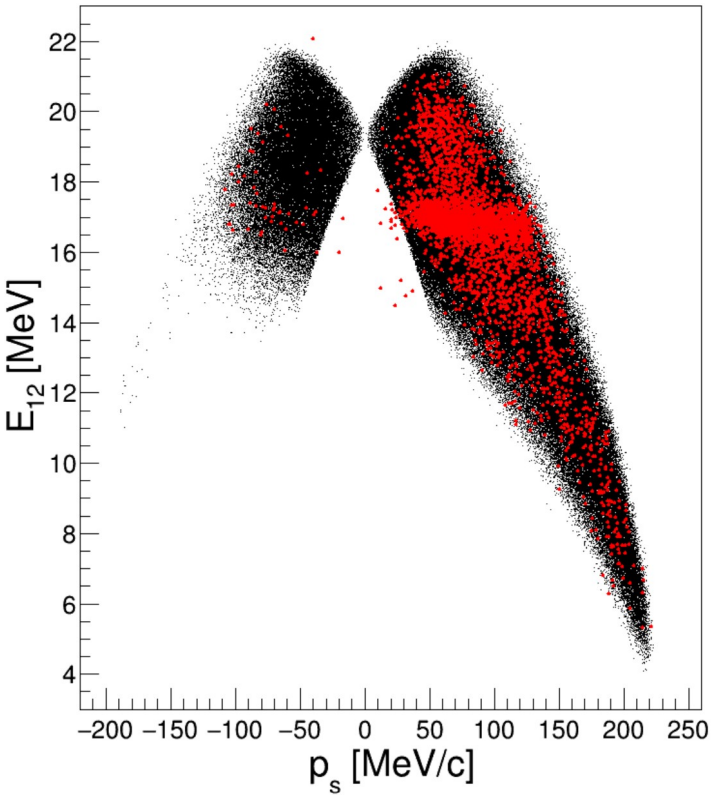

Figure 5.12: Correlation plot $E_{\alpha\alpha} - p_s$ between the α particle relative energy and the proton momentum distribution. The experimental events (red points) are compared with the simulated one (black points).

5.3 Quasi-free breakup mechanism

The THM is based on the theory of QF breakup mechanisms. This means that, in order to apply the method to the selected experimental data, it is necessary to establish whether, in the energy range where the three-body reaction has been studied, the reaction products derive from QF breakup or sequential processes. For this reason, a crucial aspect of the data analysis is to make sure that, in the selected kinematic region, the contribution of QF mechanisms is evident and distinguishable from sequential processes. In the next paragraphs I will describe the experimental approach adopted for the discrimination of QF breakup processes in the study of the reaction ^{2}H(^{7}Be,$\alpha\alpha$)p and the modalities adopted for the extraction of the cross section.

5.3.1 Discrimination of the sequential mechanisms

Once the three-body reaction of interest has been selected, the next step of the Trojan Horse analysis is the discrimination and selection of the QF contribution in the selected channel. This type of procedure is fundamental for the subsequent application of the THM: the extraction of the cross section of the two-body reaction of interest is, in fact, possible only after an accurate selection of the kinematic conditions where the QF contribution is dominant and well separable from the other contributions (sequential decay mechanism, direct breakups, and so on).

Since the particles ^{4}He and p in the reaction output channel could be produced by many different mechanisms, as shown for instance in Fig. 5.13, it is necessary to discriminate between the QF process of interest and possible sequential mechanisms, with the production of an "intermediate" nuclear structure. For this purpose, the following correlation plots with the relative energies between the two α particles, $E_{\alpha\alpha}$, between the first α and the proton, $E_{\alpha 1p}$, and between the second α and the proton, $E_{\alpha 2p}$, were drawn: $E_{\alpha\alpha} - E_{\alpha 1p}$, $E_{\alpha\alpha} - E_{\alpha 2p}$ and $E_{\alpha 1p} - E_{\alpha 2p}$ (see Fig. 5.14). In case two particles detected in coincidence have a common origin, e.g. the decay from an excited state or from the ground state of an unstable (intermediate) nucleus, straight lines are expected to be populated in the correlation plots among relative energies.

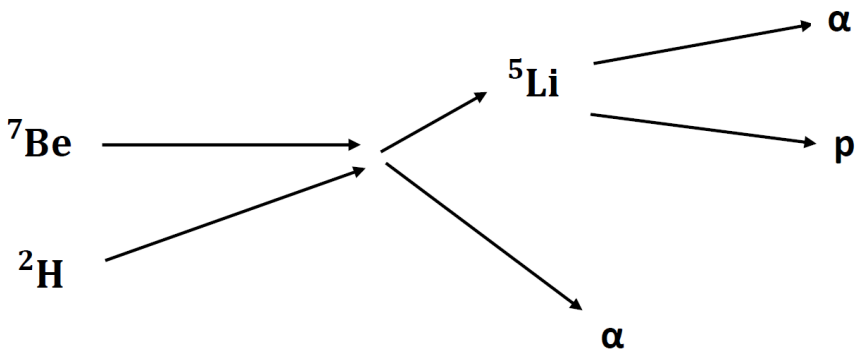

Figure 5.13: Example of a sequential mechanism that produces the same reaction products in the exit channel, but characterized by the intermediate production of ^{5}Li, that later breaks up into ^{4}He and a proton.

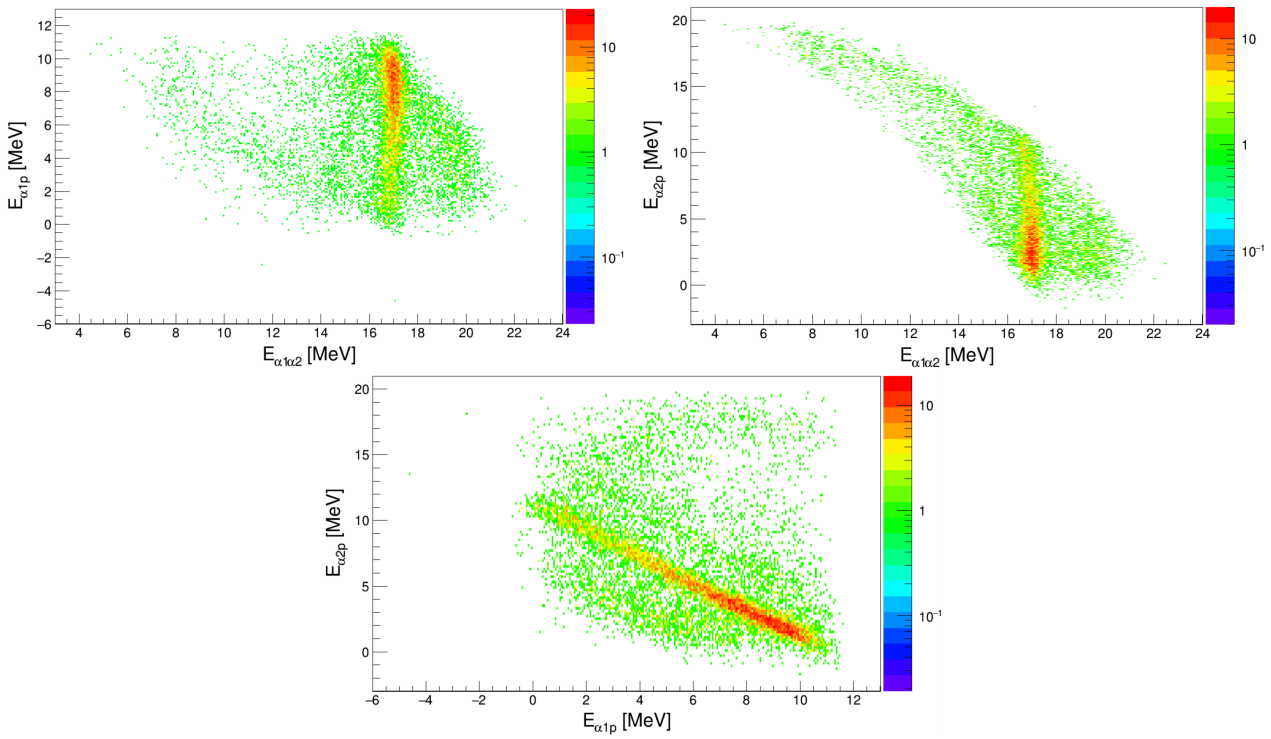

Figure 5.14: Experimental correlations plots among the relative energies of the particles detected in coincidence $E_{\alpha\alpha} - E_{\alpha 1p}$ (top left), $E_{\alpha\alpha} - E_{\alpha 2p}$ (top right), $E_{\alpha 1p} - E_{\alpha 2p}$ (bottom). The red line is associated with the 16.626 MeV and 16.922 MeV (J^{π}=2^{+}, Fig. 5.15) ^{8}Be excited states. Due to the limited detector energy resolution, it was not possible to separate the two states and only a single structure appears.

The relative energy between particles 1 and 2 E_{12} is a very important quantity because provides insight on the projectile-like excitation.

$$E_{12} = \frac{m_2 E_1 + m_1 E_2 - 2\sqrt{m_1 E_1 m_2 E_2} cos\theta_{12}}{m_1 + m_2} \tag{5.6}$$

The relative energy of the two α particles gives information related to the population of ^{8}Be exited states, associate with the QF process. On the other side, the relative energy of an α particle and a proton gives information regarding the possible population of ^{5}Li, associated a the sequential mechanism process (see Fig. 5.13).

The relative energy spectra in Fig. 5.14 represent the excitation energy spectra for ^{8}Be ($E_{\alpha\alpha}$) and ^{5}Li ($E_{\alpha p}$), respectively, except a constant term (i.e. the breakup threshold). These correlation plots allow us to identify the presence of possible excited states of ^{8}Be and ^{5}Li (resulting from the interaction between the beryllium beam and the deuteron target), thus giving important information about the possible presence of sequential mechanisms. If any state in such compound systems has been fed in the investigated phase-space region, a bump in the relative energy spectrum should be developed at the energy corresponding to the populated excited level. As shown in the correlation plot 5.14 between $E_{\alpha p}$ (y-axis) and $E_{\alpha\alpha}$ (x-axis), it is evident the absence of any horizontal line, possibly associated to the population of ^{5}Li exited states. On the contrary, it is possible to notice the marked presence of vertical line in the correlation plots $E_{\alpha\alpha}$-$E_{\alpha 2p}$ and $E_{\alpha\alpha}$-$E_{\alpha 1p}$ corresponding to the excited levels of ^{8}Be, populated by the QF breakup process.

The selected QF data are shown in Fig. 5.16 as black filled circles, with the corresponding statistical uncertainty, as a function of the kinematic quantity $E_{\alpha\alpha}$ representing the relative energy for the detected α particles. The prominent peak at $\sim$ 17 MeV corresponds to the contribution of the 16.626 MeV and 16.922 MeV (J^π=2^+, Fig. 5.15) ^{8}Be excited states.

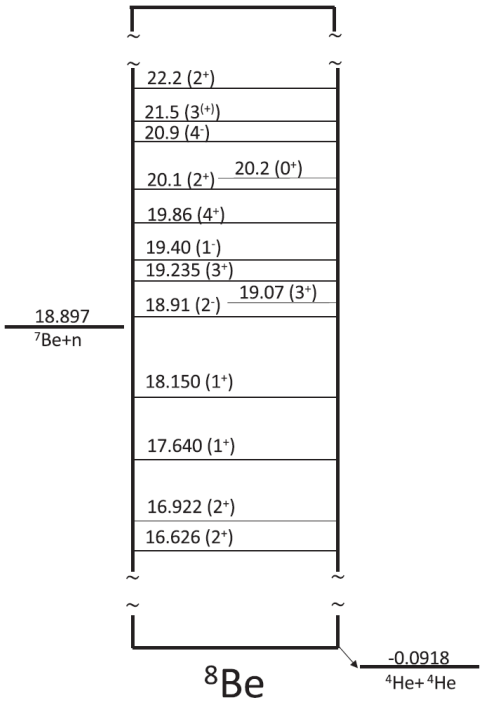

Figure 5.15: ^{8}Be energy level scheme, extracted from Kelley et al. (2012) [83], showing the levels of interest for the present investigation.

The mere presence of some excited levels is not enough, in fact, to discriminate between sequential mechanisms and QF processes. To obtain further information on the nature of the population of the energy levels, the behaviour of the coincidence yield of the reaction ^{2}H(^{7}Be,$\alpha\alpha$)p was further investigated.

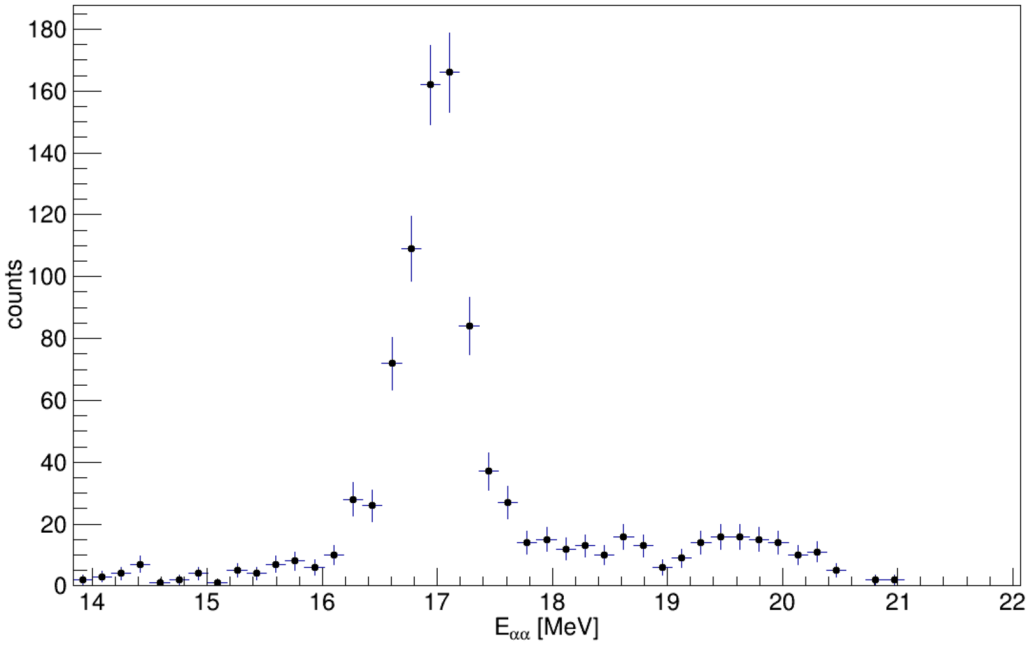

Figure 5.16: Experimental relative energy yield in the range of interest for the THM analysis, with the corresponding statistical error bars. The prominent peak at ∼17 MeV corresponds to the contribution of the 16.626 MeV and 16.922 MeV ($J^{\pi}=2^{+}$) ^{8}Be excited states (see Fig. 5.15).

Standing the relation:

$$E_{c.m.} = E_{\alpha\alpha} - Q_{2bodies} \tag{5.7}$$

where $Q_{2bodies} = 18.99$ MeV, it is important to establish if the population of the above mentioned levels occurred through a sequential mechanism or by a QF mechanism, considering the variable $E_{\alpha\alpha}$ as the momentum distribution $|p_s|$ of the unrevealed proton varies (see Fig. 5.17)

Recalling the factorization provided by the PWIA formulation for the QF processes 3.5, we have:

$$\frac{d^3\sigma}{d\Omega_c d\Omega_C dE_c} \propto KF \cdot |\Phi(p_s)|^2 \left(\frac{d\sigma_{ax}}{d\Omega}\right)_{c.m.}^{HOES} \tag{5.8}$$

that can be rewritten as:

$$\frac{d^3\sigma}{d\Omega_c d\Omega_C dE_c} \cdot \frac{1}{KF} \propto |\Phi(p_s)|^2 \left(\frac{d\sigma_{ax}}{d\Omega}\right)_{c.m.}^{HOES} \tag{5.9}$$

This means that, in the presence of a QF process, the yield of coincidence must vary following the trend of the momentum distribution $|(p_s)|$[2]. Since the QF process is correlated with this momentum distribution, the variation of the yield itself in an energy level for different values of the spectator impulse is indicative of a correlation between the values of $E_{\alpha\alpha}$ and $|(p_s)|$ and therefore of the possible presence of an QF contribution. The correlation plot shown in Fig. 5.17, obtained reporting $E_{\alpha\alpha}$ as a function of $|(p_s)|$, displays the population of levels in correspondence with the different values of the spectator proton momentum distribution.

[2]The analysis of the spectator proton momentum is of fundamental importance to test the hypotheses of applicability of PWIA in the description of QF breakup process. The crucial assumption of QF mechanisms is that the incident nucleus interacts only with one of the two nucleons in the deuteron (e.g. the neutron) leaving the proton as a spectator of the process. This hypothesis is even more verified when the De Broglie wavelength λ_B associated to the incident nucleus is shorter than the size of the target nucleus (a few fm).

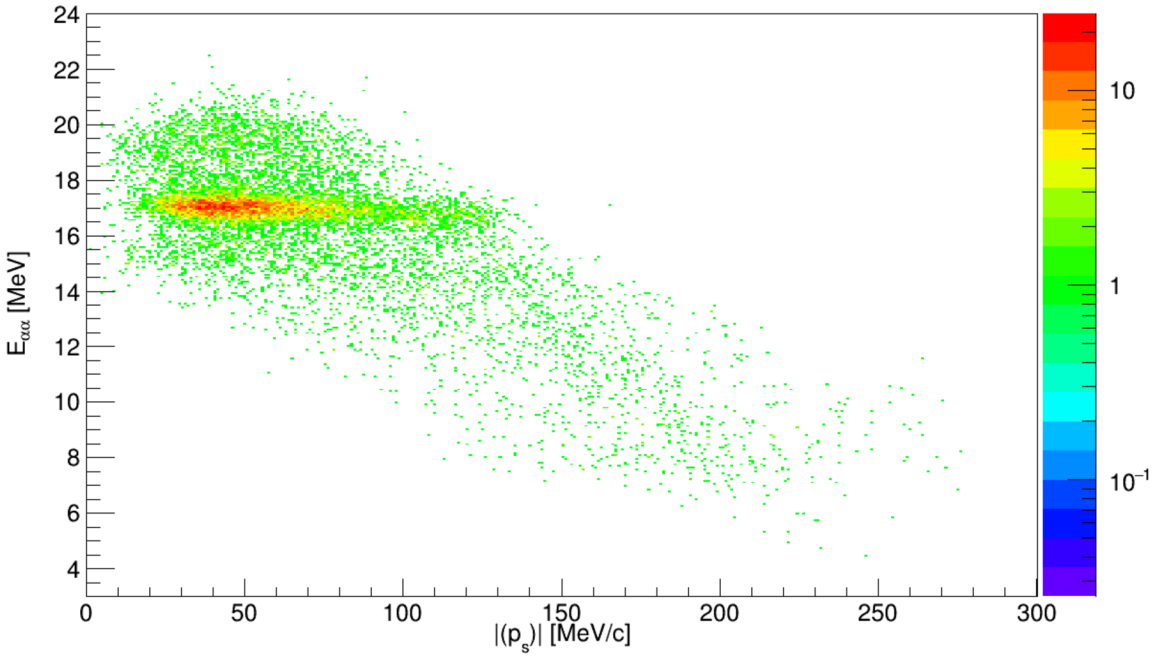

Figure 5.17: $E_{\alpha\alpha}$ as a function of the spectator particle momentum. The level structure at $\sim$ 17 MeV is the only one present in the $E_{c.m.}$ of interest.

5.4 Evidence of the quasi-free mechanism

5.4.1 Theoretical and experimental impulse distribution

As already mentioned, the peculiarity and strong aspect of the THM is that the cross section of the two-body reaction of interest can be extracted through the measurement of the cross section for a suitable three-body reaction in the final state using the equation:

$$\frac{d^3\sigma}{d\Omega_c d\Omega_C dE_c} \propto KF \cdot |\Phi(p_s)|^2 \frac{d^2\sigma}{d\Omega_s dE_{c.m.}} \tag{5.10}$$

This equation is however valid in the hypothesis of PWIA. This hypothesis must, therefore, be verified experimentally analyzing in detail the trend of the momentum distribution of the spectator particle. By suitably rewriting the predicted factorization of the cross section in PWIA, we have:

$$|\Phi(p_s)| \propto \frac{d^3\sigma}{d\Omega_c d\Omega_C dE_c} \left[KF \cdot \frac{d^2\sigma}{d\Omega_s dE_{c.m.}} \right]^{-1} \tag{5.11}$$

Assuming that we consider an energy region where $\frac{d^2\sigma}{d\Omega_s dE_{c.m.}}$ can be considered constant, the ratio between the coincidence yield and KF should reproduce, in the presence of a QF mechanism, the distribution of proton momentum in the deuterium.

For this purpose, we selected a narrow energy window in the $\alpha\alpha$ relative energy distribution, $E_{\alpha\alpha}$, between 18 and 19 MeV and its projection on the $|p_s|$ axis was derived. Once corrected for the kinematic factor and after selecting the proper energy range, this distribution was compared with the theoretically expected one, i.e. the Hulthén function having a maximum for $|p_s| = 0$ MeV/c and a FWHM of about 58 MeV/c [68; 84][3]

[3]The wave function of the $p-n$ relative motion according to the Hulthén function was considered in the data analysis:

$$\psi(\vec{r}) \propto \frac{e^{-ar} - e^{-br}}{e} \Longrightarrow F[\psi] \Longrightarrow \Psi(\vec{p}) \propto \left[\frac{1}{a^2 + p_s^2} - \frac{1}{b^2 + p_s^2} \right] \tag{5.12}$$

with $a = 0.2317$ fm^{-1} and $b = 1.202$ fm^{-1} [68].

Fig. 5.18 shows that the experimental distribution presents a maximum at $|\vec{p_s}| = 0$ MeV/c, as expected since the wave function expressing the $p-n$ relative motion in the deuteron has a dominant contribution from the $l = 0$ state. The obtained FWHM of 56 $\pm$4 MeV/c is also in remarkable agreement with the expectations ($\sim$ 58 Mev/c) [84]. In conclusion, the overall agreement observed, within the statistical errors, between the theoretical and the experimental momentum distribution represents a further necessary step to establish the existence of the QF mechanism.

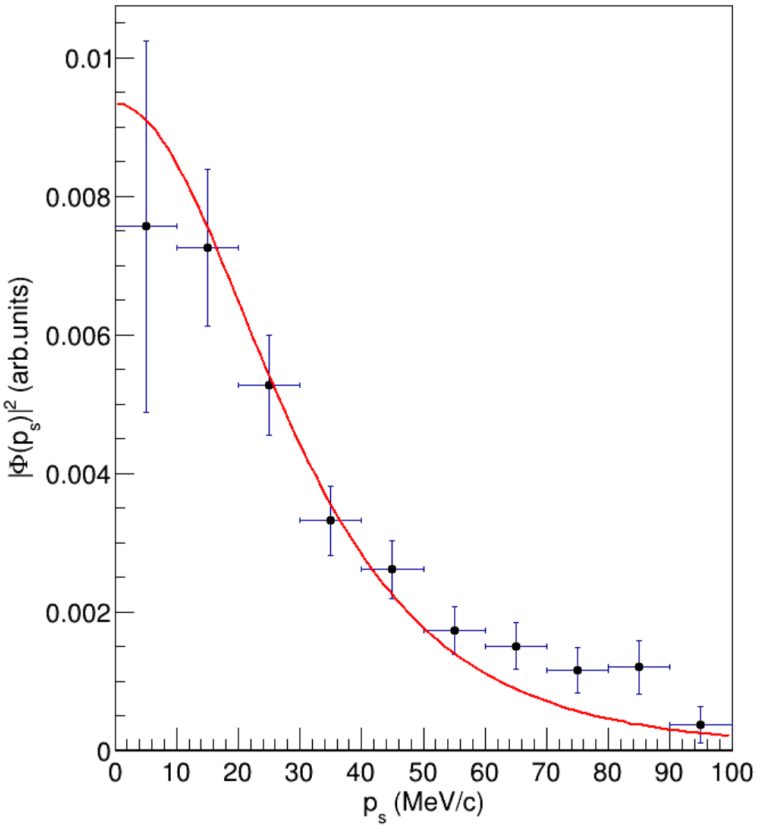

Figure 5.18: Experimental momentum distribution for the emerging proton in the ^{2}H(^{7}Be,$\alpha\alpha$)p reaction (black points), with the corresponding statistical error bars. The experimental data are compared with the squared module of the theoretical Hulthén wavefunction in momentum space. See text for additional details.

5.5 Two-body cross section derivation of the cosmologically relevant ^{7}Be(n,α)^{4}He reaction

5.5.1 Differential cross section for the three-body reaction

As discussed in chapter III, the basic idea of the THM is to extract the cross section for the astrophysically relevant two-body reaction from a measurement of the cross section of a suitable three-body surrogate reaction. In the PWIA, these two quantities are related by formula 3.5:

$$\frac{d^3\sigma}{d\Omega_\alpha d\Omega_\alpha dE_{c.m.}} \propto KF \cdot |\Phi(p_s)|^2 \left(\frac{d\sigma}{d\Omega}\right)^N_{^7Be-n} \tag{5.13}$$

Reversing the equation we obtain:

$$\left(\frac{d\sigma}{d\Omega}\right)^N_{^7Be-n} \propto \frac{d^3\sigma}{d\Omega_\alpha d\Omega_\alpha dE_{c.m.}} [(KF)|\Phi(\vec{p_s})|^2]^{-1} \tag{5.14}$$

Thus, we have at first to establish the trend of the coincidence yield $\frac{d^3\sigma}{d\Omega_\alpha d\Omega_\alpha dE_{c.m.}}$ as a function of the interaction energy between the two α particles measured in the centre of mass and defined by

expression 5.7. To do it, we first considered the trend of the $E_{\alpha\alpha}$ coincidence yield spectrum selecting the events corresponding to the $|\vec{Ps}| < 50$ MeV/c [84] region and fixing the angular range in $\theta_{c.m.}$ (top panel Fig. 5.19) This condition on $|\vec{Ps}|$ makes it possible to select essentially data coming from QF processes, and on the other hand, reduces the possible pollution from sequential mechanisms.

Therefore, from the trend of $E_{\alpha\alpha}$ coincidence yield we derived the experimental $\frac{d^3\sigma}{d\Omega_\alpha d\Omega_\alpha dE_{c.m.}}$ as a function of the energy of the centre of mass by subtracting the $Q_{2bodies}$ from the α relative energy (see the middle panel of Fig. 5.19).

Finally, before proceeding with the calculation of the two-body cross section, it was necessary to determine also the trend of the simulated coincidence yield as a function of the interaction energy between the two α particles measured in the centre of mass (bottom panel Fig. 5.19).

In the derivation process of the experimental and simulated coincidence yield, a binning of 200 keV was chosen. This choice was dictated by the necessity to find a compromise between the statistic and the energy resolution. Moreover, in order to compare our cross section with the one obtained by L. Lamia et al. [80], we needed to use a common binning.

5.5.2 Extraction of the two-body cross section

From the information obtained in the previous section and thanks to Eq. 5.14, it is now possible to derive the HOES two-body cross section. Eq. 5.14 states that $(\frac{d\sigma}{d\Omega})^{HOES}$ is given by the ratio between the $\frac{d^3\sigma}{d\Omega_\alpha d\Omega_\alpha dE_{c.m.}}$ and the quantity $[(KF)|\Phi(\vec{p_s})|^2]$. Fig. 5.20 shows the HOES two-body cross extracted as a function of the centre of mass energy. We remind that the cross section is "half off-energy shell", since the participant in the reaction x is a virtual particle. This means that, due to the presence of the binding energy in the Trojan Horse nucleus, its energy and momentum are not related by the mass-shell equation: $E_x = p^2/2m_x$.

In order to compare our data with those obtained in direct measurements, it is necessary to introduce the penetrability through the centrifugal barrier, which in the case under investigation has a dominant contribution in $l = 1$ wave. Since the THM experiment relies on the coincidence detection of two αs, the parity conservation rule requires a p-wave interaction in the entrance channel of the ^{7}Be(n,α)^{4}He binary process. For this reason, an $l = 1$ angular distribution was assumed. In addition, since our experiment covered a limited range in azimuthal angle, $100° < \phi_{c.m.} < 180°$, and the energy resolution did not allow to perform a detailed study of the angular distribution, the integration over the whole angular range led to a common constant factor in the energy interval measured. This factor was included in the normalization constant.

Therefore, having established the penetrability factor P_l[4] and remembering that

$$\left(\frac{d\sigma}{d\Omega}\right)^{THM} \propto \sum W_l P_l \left(\frac{d\sigma}{d\Omega}\right)^{HOES} \tag{5.16}$$

the THM cross section was extracted as a function of the energy $E_{c.m.}$ (see Fig. 5.21). In the following part, I will explain in details the practical procedure adopted to derive the final two-body cross section.

We first calculated the ratio between the experimental and the simulated coincidence yield $\frac{d^3\sigma}{d\Omega_\alpha d\Omega_\alpha dE_{c.m.}}$ as a function of $E_{c.m.}$. In this way, we obtained the two-body HOES cross-section (See Fig. 5.21). Finally, the HOES cross section was multiplied to the penetrability factor P_l, calculated using a proper program written in Mathematica [85] and needed for the normalization to the direct data.

[4]It is possible to calculate the barrier penetration probability for a free particle (wave function calculated at infinity) by means of the equation (for $l = 1$ case):

$$P_l(E, kr) = \left|\frac{w_l(\infty)}{w_l(r)}\right|^2 = \frac{1}{kr(F_l^2(kr) + G_l^2(kr)} \tag{5.15}$$

where r is the interaction radius calculated via the formula $r = r_0(A_n^{1/3} + A_{^7Be}^{1/3})$, k is the wave number (defined as $p/\hbar$) and F_l and G_l depend on the Bessel ($j_l(kr)$) and Neumann ($n_l(kr)$) spherical functions, respectively.

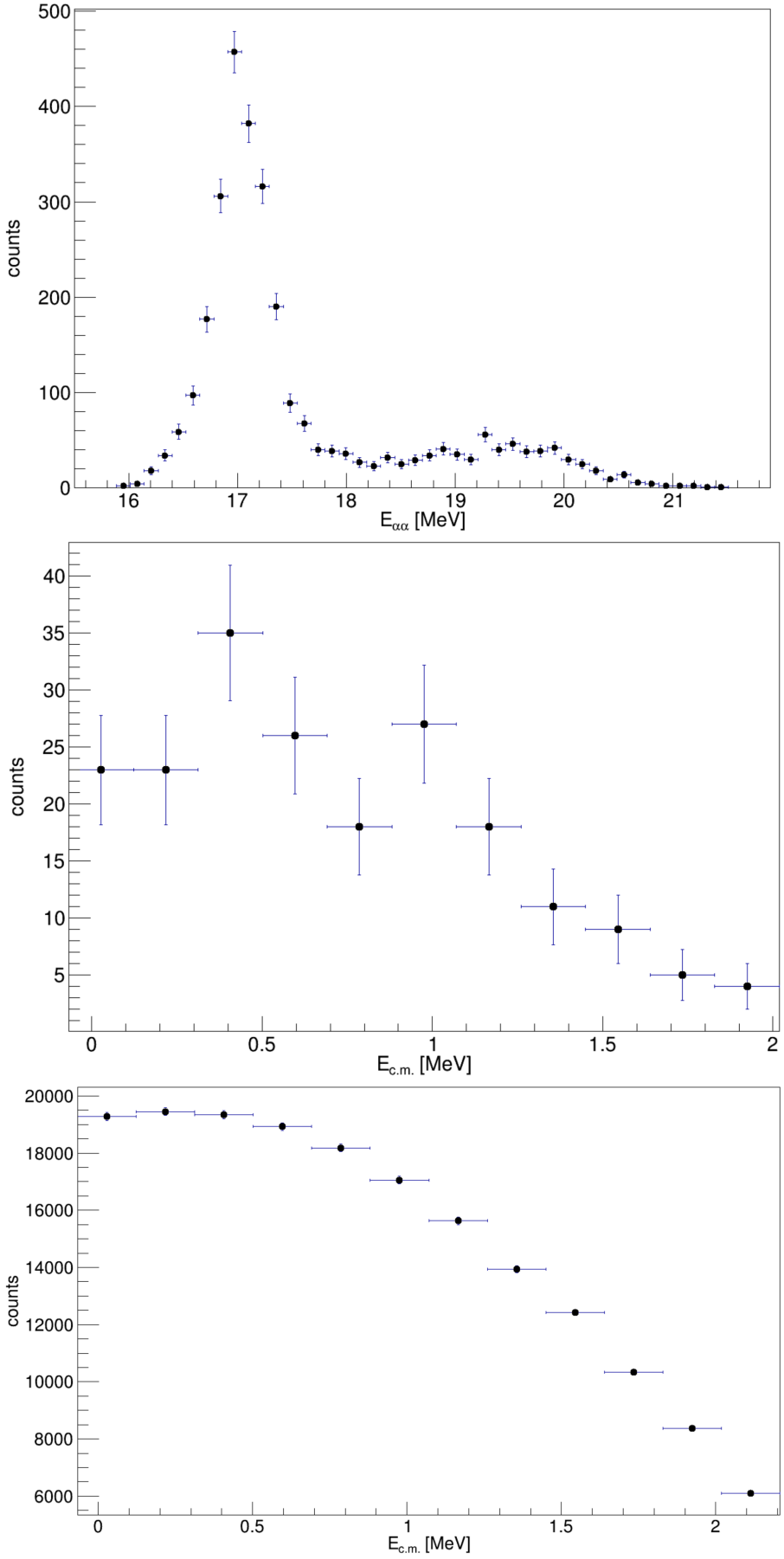

Figure 5.19: Top panel: Coincidence yield in the relative energy range of interest for the THM analysis, once the QF component has been disentangled. Middle panel: trend of $\frac{d^3\sigma}{d\Omega_\alpha d\Omega_\alpha dE_{c.m.}}$ as a function of the interaction energy between the two αs measured in the centre of mass and defined by expression 5.7. Bottom panel: simulated coincidence yield as a function of the interaction energy between the two measured in the centre of mass reference frame.

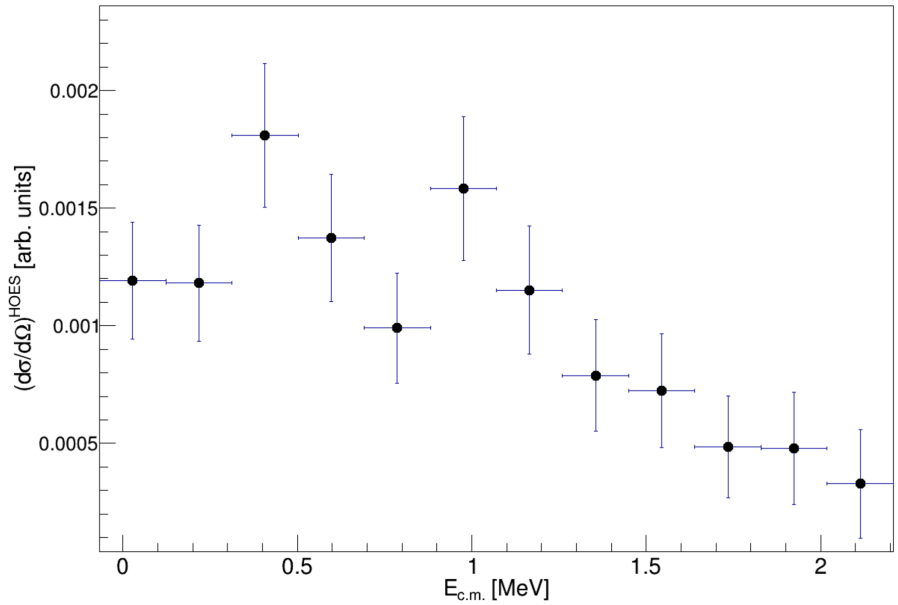

Figure 5.20: HOES cross section (in arbitrary units), $(\frac{d\sigma}{d\Omega})^{HOES}$, extracted as a function of the center of mass energy, $E_{c.m.}$.

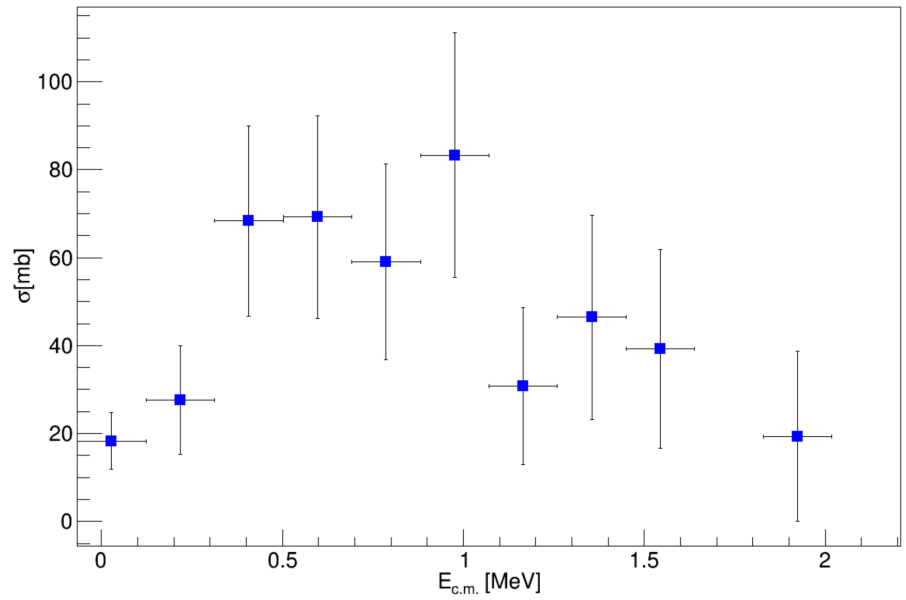

Figure 5.21: THM ^{7}Be(n,α)^{4}He cross-section measurement obtained after the multiplication of the HOES cross section with the penetrability factor P_l and the scaling factor. See text for additional details.

To deduce the THM results in absolute units, a normalization to the measurement of Hou et al. [48] was performed. In more details, the normalization factor was calculated in three different ways:

1. The ratio between the indirect and direct values of the cross-section was calculated for all the overlapping experimental points in the energy range 20 keV - 1.9 MeV , for a total of 10 points, and an average value of 56.4 ± 0.3 was estimated;

2. the data of Hou et al. [48] were first fitted with a Breit-Wigner function with the purpose of deducing an analytical function describing their trend. The obtained function was then spread out for the experimental energy resolution (∼ 300 keV) of the present THM investigation. Finally, the normalization factor was deduced by requiring the integral of the THM cross section data (over the whole energy range) be equal to that for the data of Hou et al. [48]. In this case, a normalization factor of 41.5 ± 0.9 was obtained;

3. the same procedure as the previous point was applied, but considering a Gaussian function instead of a Breit-Wigner curve. A normalization factor of 44.8 ± 8.3 was computed with this approach.

After a careful analysis of the results of the three methods, the normalization factor provided by the second approach, $(41.5 \pm 0.9) \cdot 10^3$, was adopted. The first method, although being characterized by a smaller error, is quite useful to get a first idea about the order of magnitude of the normalization factor, but results to be rather inadequate since it considers all the experimental points but not the overall trend of the distribution. The third approach was only a test of the procedure for future developments and, in any case, the relative error was rather high. We remark that in standard Trojan Horse experiments, the normalization to direct data is routinely performed using the second approach.

The error associated to the cross section contains a statistical component (∼ 13% - ∼ 20%), the uncertainty on the normalization factor (∼ 2%) and a systematic error related to the calculation of the penetrability factor (∼ 10% - ∼ 15%).

Fig. 5.22 shows the comparison of the THM cross section (after normalization) with the direct data of Kawabata et al. [50] (red points) and of Hou et al. [48] (black points) in the center of mass energy region ∼ 20 keV $< E_{c.m.} <\sim$ 2 MeV. It is possible to appreciate the overall good agreement between the results of this work and previous direct measurements. Moreover, a good agreement is also observed comparing the present results with those obtained by Lamia et al. [80], originating from the data analysis of the $\alpha - \alpha$ coincidences detected by telescopes B and D during the same experiment.

The last step of this work was to combine the cross section values obtained in this work with those of Lamia et al. [80] shown in the lower panel of Fig. 5.22. This step was of great importance because it helped to reduce the errors of the cross sections and therefore to obtain a more precise and meaningful result. Fig. 5.23 shows the final THM evaluation of the cross section for the reaction ^{7}Be(n,α)^{4}He in the energy range of astrophysical interest for the BBN.

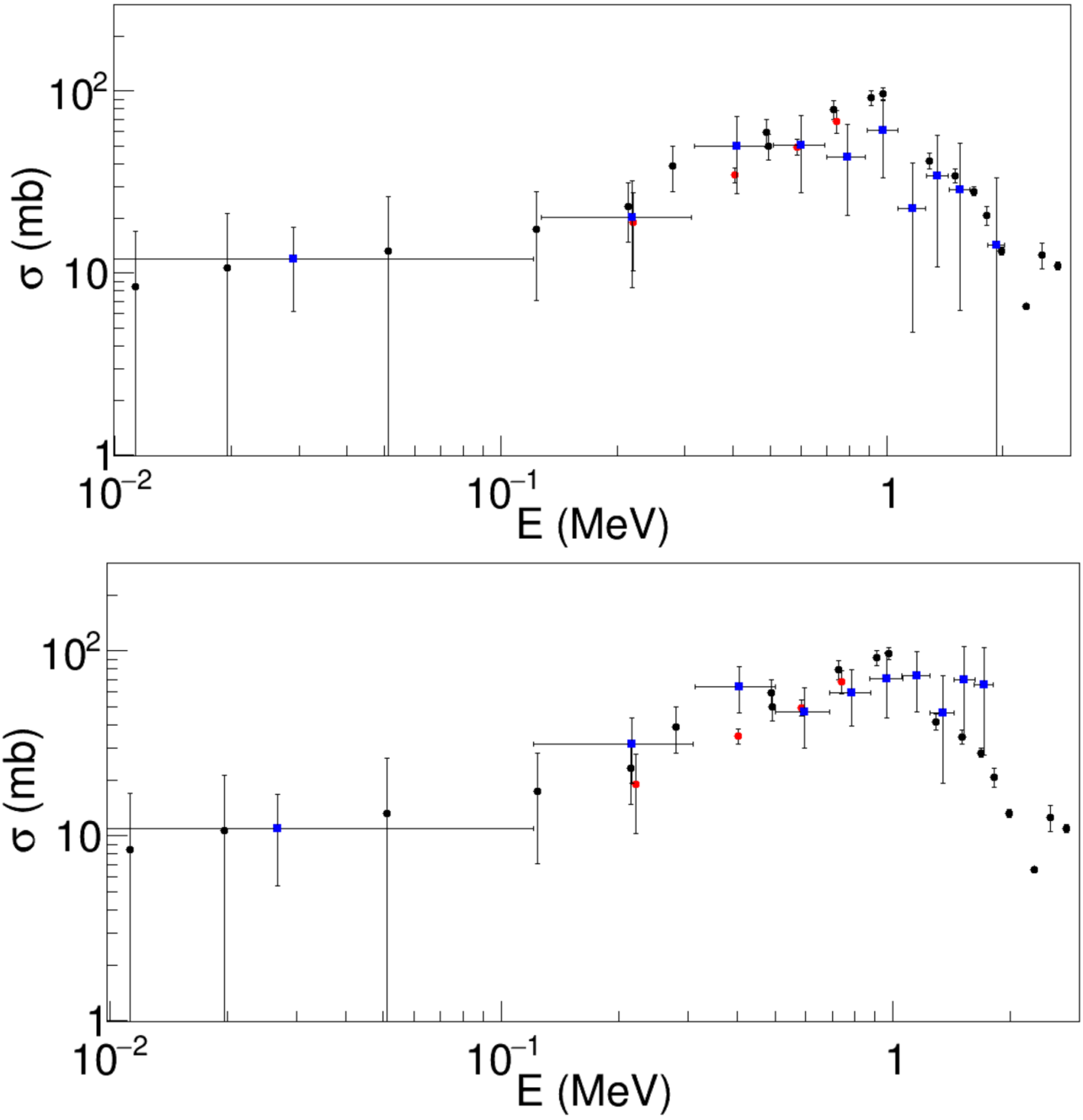

Figure 5.22: Upper panel: THM ^{7}Be(n,α)^{4}He cross-section measurement (blue points with the statistical error) obtained from this work.
Lower panel: THM cross-section measurement (blue points with the statistical error) obtained by the analysis of Lamia and collaborators in 2019 [80].
In both panels the THM cross sections are compared with the direct measurements of Kawabata et al. (red points) [50] and Hou et al. (black points) [48]

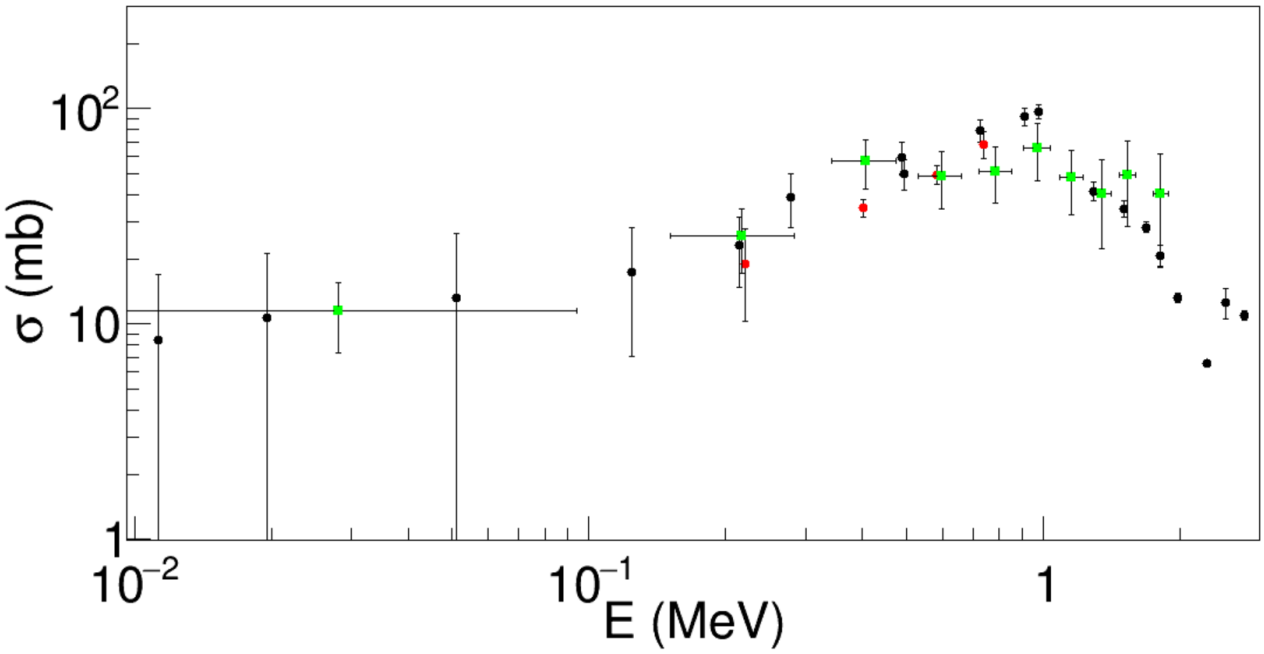

Figure 5.23: Average (green points with the statistical error) of the THM ^{7}Be(n,α)^{4}He cross-section measurements between the results of the present work and those originated from the same experiment and published in Ref. [80], compared to the direct measurements of Kawabata et al. [50] (red points) and Hou et al. [48] (black points).

Outlook

5.6 Conclusions

The result obtained in this thesis work represents an additional ^{7}Be(n,α)^{4}He cross section measurement of interest for cosmology. The ^{7}Be-n reaction was investigated by means of the THM applied to the QF ^{2}H(^{7}Be,$\alpha\alpha$)p reaction, once the QF reaction mechanism was selected properly. The binary cross section extracted allowed us to span a wide range in energy in a single experiment overlapping both the high-energy region and the one of interest for BBN. Our result is in remarkable agreement with direct measurements currently available in literature and with the more recent ^{7}Be(n,α)^{4}He measurements discussed in Hayakawa et al. [86].

The values of the ^{7}Be(n,α)^{4}He cross section are in good agreement with those obtained by Lamia et al. [80] analyzing a complementary set of data collected during the same experiment. Combining both data sets will help in the next future to reduce the uncertainties in the evaluation of the reaction rates in the energy range of interest for the BBN, thus allowing for an overall better characterisation of this reaction. Nevertheless, we foresee that the conclusions on the possible impact of the reaction rate to solve the cosmological lithium problem might be similar to those withdrawn in [80]. In particular, we expect a final lithium abundances very close to 4.26 $\cdot 10^{-10}$ [80], that remain larger then the one deduced by Sbordone et al. (2010) [10] for halo-star observations, i.e., $(1.58^{+0.35}_{-0.28})\cdot 10^{-10}$.
In conclusion, from the experimental investigation of the ^{7}Li cosmological problem by means of the THM applied to the ^{7}Be(n,α)^{4}He, we expect that its contribution will not allow to solve the issue. As a consequence, other solutions must be found in the study of other relevant nuclear processes or in phenomena unrelated to Nuclear Physics [87].

5.7 Future perspectives

From the point of view of nuclear physics, the only remaining uncertainty in the investigation of the ^{7}Li cosmological problem is the study of the ^{7}Be(n,p)^{7}Li reaction. Qualitatively, in order for this reaction to have a significant impact on understanding the theoretical and experimental difference of the ^{7}Li primordial abundance, its cross section must be four times larger than that obtained by L. Damone et al. (2018) [88].

This aspect, besides being very unlikely, has been disproved by recent measurements of the cross section, which agree with values calculated in the past [88], suggesting that this reaction also does not play an important role in solving the ^{7}Li cosmological problem. The recent work of Hayakawa et al. [86] highlighted the role of the ^{7}Be(n,p)^{7}Li reaction. The results show a decrease of about 10% on the theoretical abundances of ^{7}Li, thus slightly alleviating the cosmological lithium problem.

These nuclear astrophysics studies show that the ^{7}Li cosmological problem is not confined to nuclear

physics, but that other solutions must be sought in other areas. However, the present study represents an important step in the application of THM to reactions between RIBs and neutrons and opens up new windows on many possible future applications, as for instance the future study of the reaction between ^{26}Al and neutrons, which might be performed with the SPES [89] facility at LNL.

Appendix

As an example, a few ROOT macros, written in the programming language C++, developed and implemented for the data analysis are presented below.

5.8 Macro for the kinematical analysis

```
  Double_t sdx[4] = {62.3, 62.3, 62.3, 62.3};
  Double_t sdy[4] = {62.3, 62.3, 62.3, 62.3};
  // Offsets in (x,y,z) (mm)
  Double_t crdx[4] = {0., 0., 0., 0.};
  Double_t crdy[4] = {0., 0., 0., 0.};
  Double_t crdz[4] = {0., 0., 0., 0.};
  // Distance between rotation center and PSD (mm)
  Double_t dcr2d[4] = {244.2, 239.5, 243.5, 241.7};
  // Rotation angle in x-z plane (deg)
  Double_t rot_xz[4] = {-63., -27., 27., 63.};

  Double_t pi = 3.141592;
  Double_t d2r = pi/180.;

      Double_t     u=931.49432/1000.;    // unita' di massa (rif. 12C)

////////// reazione 7Be(d,a)a,p --> 7Be(n,a)a ////////////////////////////
    Double_t     mp=7.016929;  // massa proiettile             //
//    Double_t     ep=20.576; // energia proiettile 7Be half target da 412ug/cm2//
Double_t     ep=19.96; // energia proiettile 7Be calibrata
da Livio su stripB dopo half target da 412ug/cm2//
    Double_t     mt=2.014101;    // massa target                 //
    Double_t     m1=4.002603;      // massa prima part. uscente    //
    Double_t     m2=4.002603;      // massa seconda part. uscente  //
    Double_t     m3=1.007825;      // massa terza part. uscente    //
    Double_t     mx=1.008664;  // massa part. trasferita //
    Double_t     q2=18.99; // Q della reazione 2->2 //


    A_xcal[0]=  A_x[0]*0.009572479-0,280398692;
```

```
A_xcal[2]=  A_x[2]*0.009920627-0.306813597;
A_xcal[4]=  A_x[4]*0.00999382-0,331342409;
A_xcal[6]=  A_x[6]*0.00999382-0.353509094;
A_xcal[8]=  A_x[8]*0.009572479-0.280398692;
A_xcal[10]= A_x[10]*0.009602245-0.348229809;
A_xcal[12]= A_x[12]*0.00965026-0.370876129;
A_xcal[14]= A_x[14]*0.010069399-0.389995516;
A_xcal[16]= A_x[16]*0.009666525-0.392838554;
A_xcal[18]= A_x[18]*0.009882249-0.411868056;
A_xcal[20]= A_x[20]*0.009808795-0.410633194;
A_xcal[22]= A_x[22]*0.009987399-0.439084839;
A_xcal[24]= A_x[24]*0.010058427-0.437208553;
A_xcal[26]= A_x[26]*0.009835707-0.440902862;
A_xcal[28]= A_x[28]*0.010026297-0.451819412;
A_xcal[30]= A_x[30]*0.009762267-0.423774318;


A_ycal[0]=  A_y[0]*0.009053274-0.077069979;
A_ycal[2]=  A_y[2]*0.009477447-0.092115664;
A_ycal[4]=  A_y[4]*0.009315825-0.091390967;
A_ycal[6]=  A_y[6]*0.009393442-0.113774635;
A_ycal[8]=  A_y[8]*0.009516276-0.110984578;
A_ycal[10]= A_y[10]*0.009360438-0.121948243;
A_ycal[12]= A_y[12]*0.009488897-0.117697396;
A_ycal[14]= A_y[14]*0.009307366-0.119872672;
A_ycal[16]= A_y[16]*0.009472388-0.128898873;
A_ycal[18]= A_y[18]*0.009517501-0.135896922;
A_ycal[20]= A_y[20]*0.009446876-0.134898589;
A_ycal[22]= A_y[22]*0.009579143-0.13113443;
A_ycal[24]= A_y[24]*0.009483351-0.138899963;
A_ycal[26]= A_y[26]*0.009459273-0.167598836;
A_ycal[28]= A_y[28]*0.009474767-0.145618314;
A_ycal[30]= A_y[30]*0.009469653-0.155166401;


C_xcal[0]= C_x[0]*0.009608577-0.23473077;
C_xcal[2]= C_x[2]*0.00944208-0.237369996;
C_xcal[4]= C_x[4]*0.009605912-0.262786465;
C_xcal[6]= C_x[6]*0.009675686-0.268584358;
C_xcal[8]= C_x[8]*0.009639804-0.255181719;
C_xcal[10]= C_x[10]*0.009756147-0.239799886;
C_xcal[12]= C_x[12]*0.009331901-0.241183247;
C_xcal[14]= C_x[14]*0.009392907-0.290661442;
C_xcal[16]= C_x[16]*0.009801069-0.299988622;
C_xcal[18]= C_x[18]*0.009640605-0.256868352;
C_xcal[20]= C_x[20]*0.009655402-0.251450243;
C_xcal[22]= C_x[22]*0.009473766-0.261725991;
C_xcal[24]= C_x[24]*0.009683659-0.225672238;
C_xcal[26]= C_x[26]*0.009632291-0.274268961;
C_xcal[28]= C_x[28]*0.00975161-0.27107341;
C_xcal[30]= C_x[30]*0.009731427-0.230552425;
```

```
C_ycal[0]= C_y[0]*0.009508694-0.249587922;
C_ycal[2]= C_y[2]*0.009403852-0.270324111;
C_ycal[4]= C_y[4]*0.009366002-0.266194062;
C_ycal[6]= C_y[6]*0.009366002-0.266194062;
C_ycal[8]= C_y[8]*0.009528814-0.277208139;
C_ycal[10]= C_y[10]*0.009487812-0.270113481;
C_ycal[12]= C_y[12]*0.009511019-0.29595658;
C_ycal[14]= C_y[14]*0.009649572-0.339378308;
C_ycal[16]= C_y[16]*0.009486403-0.319396741;
C_ycal[18]= C_y[18]*0.009530117-0.312144219;
C_ycal[20]= C_y[20]*0.009427753-0.317416152;
C_ycal[22]= C_y[22]*0.009487287-0.343450234;
C_ycal[24]= C_y[24]*0.009651352-0.32554861;
C_ycal[26]= C_y[26]*0.0096087-0.332632354;
C_ycal[28]= C_y[28]*0.009614193-0.303282318;
C_ycal[30]= C_y[30]*0.009652882-0.351787896;



////////kinematical variabiles calculation

      //TLorentzVector p12=*p1+*p2;
      //TLorentzVector p13=*p1+*p3;
      //TLorentzVector p23=*p2+*p3;
      TLorentzVector p12=p1+p2;
      TLorentzVector p13=p1+p3;
      TLorentzVector p23=p2+p3;
      TLorentzVector p12b2=p1b2+p2;
      TLorentzVector p13b2=p1b2+p3b2;
      TLorentzVector p23b2=p2+p3b2;

      TVector3 v0 = pow(u*mp,-1)*(beam.Vect());
      TVector3 v1 = pow(u*m1,-1)*pp1;
      TVector3 v1b2 = pow(u*m1,-1)*pp1b2;
      TVector3 v2 = pow(u*m2,-1)*pp2;
      TVector3 v3 = pow(u*m3,-1)*pp3;
      TVector3 v3b2 = pow(u*m3,-1)*pp3b2;
      TVector3 ki=-(m3/mx)*v3-v0;
      TVector3 kf= v1-v2;
      TVector3 kib2=-(m3/mx)*v3b2-v0;
      TVector3 kfb2= v1b2-v2;

      e1=(pp1*pp1/(2*m1*u))*1000.;
      e1b2=(pp1b2*pp1b2/(2*m1*u))*1000.;
      e2=(pp2*pp2/(2*m2*u))*1000.;
      e3=(pp3*pp3/(2*m3*u))*1000.;
      e3b2=(pp3b2*pp3b2/(2*m3*u))*1000.;

      Double_t t1=(p1.Theta())/d2r;
      Double_t t1b2=(p1b2.Theta())/d2r;
      Double_t t2=(p2.Theta())/d2r;
      Double_t t3=(p3.Theta())/d2r;
```

```
    Double_t t3b2=(p3b2.Theta())/d2r;

    Double_t theta_3=t3;
    Double_t theta_3b2=t3b2;
    e12= (p12.M()-u*(m1+m2))*1000.;
    e13= (p13.M()-u*(m1+m3))*1000.;
    e23= (p23.M()-u*(m2+m3))*1000.;
    e12b2= (p12b2.M()-u*(m1+m2))*1000.;
    e13b2= (p13b2.M()-u*(m1+m3))*1000.;
    e23b2= (p23b2.M()-u*(m2+m3))*1000.;

    ecm= e12-q2;
    ecmb2= e12b2-q2;
    tcm= (ki.Angle(kf))/d2r;
    tcmb2= (kib2.Angle(kfb2))/d2r;

    Double_t scp;
    if(cos(pp3.Phi())>0)
    scp=1;
    else if (cos(pp3.Phi())<0)
    scp=-1.;
    else
    scp=0.;
    ps=(pp3.Mag())*scp*1000.;

    Double_t scpb2;
    if(cos(pp3b2.Phi())>0)
    scpb2=1;
    else if (cos(pp3b2.Phi())<0)
    scpb2=-1.;
    else
    scpb2=0.;
    psb2=(pp3b2.Mag())*scpb2*1000.;


    q3=e1+e2+e3-ep;
    q3bis=Etot_C1+Etot_A+e3-ep;
    q3b2=e1b2+e2+e3b2-ep;
    q3bisb2=Etot_C2newC+Etot_A+e3b2-ep;

    if(E_C<0.35){
     e12new=e12;
     e13new=e13;
     e23new=e23;
     ecmnew=ecm;
     tcmnew=tcm;
     psnew=ps;
     theta_3new=theta_3;
     e1new=e1;
     e3new=e3;
     q3new=q3;
     q3bisnew=q3bis;
} else {
```

```
   e12new=e12b2;
       e13new=e13b2;
       e23new=e23b2;
       ecmnew=ecmb2;
       tcmnew=tcmb2;
       psnew=psb2;
       theta_3new=theta_3b2;
       e1new=e1b2;
       e3new=e3b2;
   q3new=q3b2;
   q3bisnew=q3bisb2;
  }
```

5.9 Macro for the derivation of the momentum distribution

```
TFile hh("fileA3_EC25055_random_ACmaxnew_riletto_r4000-thintarget.root");
TFile ff("sim_3d_belicos_res_no_mod1.root");
TH1F *pssim=new TH1F ("pssim","pssim",10,0,100);
//TH1F *pssim1=new TH1F ("pssim1","pssim1",10,0,100);
sim->Draw("abs(ps)>>pssim","TDd>20 && TDd<34 && TBd<70
&& TBd>56 && (((180-PDd)>0
&& (180-PDd)<25) || ((180-PDd)>335 && (180-PDd)<365))
&& (180-PBd)>170 && (180-PBd)<190
&& EDs>5 && EBs>5 && e12>19 && e12<21");

hh.cd();
TH1F *psexp=new TH1F ("psexp","psexp",10,0,100);
run2->Draw("abs(psnew)>>psexp","q3bisnew > 15.633
&& q3bisnew< 17.7 && theta_C>20 && theta_C<34 && theta_A<70 && theta_A>56
&& ((phi_C>0 && phi_C<25) || (phi_C>335 && phi_C<365))
&& phi_A>170 && phi_A<190 && multA==1 && multC==1
&& e12new>19 && e12new<21 && nA_y>3 && nA_y<11 && nC_y>3 && nC_y<11");
psexp->Sumw2();
pssim->Sumw2();
TH1F *psdiv=new TH1F ("psdiv","psdiv",10,0,100);
psdiv->Divide(psexp,pssim);
psdiv->Draw("e1");
TF1 *f18a=new
TF1("f18a","0.041e+06*((1/(x^2+(0.2317*197.327)^2)-1/(x^2+(1.202*197.327)^2))^2)",0,100);
f18a->Draw("same");
```

5.10 Macro for the calculation of the two body cross section

```
TFile hh("fileA3_EC25055_random_ACmaxnew_riletto_r4000-thintarget.root");
TFile ff("sim_3d_belicos_res_mod1.root");
TH1F *esim=new TH1F ("esim","esim",20,-0.099,2.2);

sim->Draw("e12-18.99>>esim","TDd>20 && TDd<34 && TBd<70 && TBd>56
&& (((180-PDd)>0 && (180-PDd)<25) || ((180-PDd)>335
&& (180-PDd)<365)) && (180-PBd)>170 && (180-PBd)<190
&& EDs>5 && EBs>5 && e12>18 && abs(ps)<55");
```

```
hh.cd();
TH1F *eexp=new TH1F ("eexp","eexp",20,-0.099,2.2);
run2->Draw("e12new-18.99>>eexp","q3bisnew > 15.633
&& q3bisnew< 17.7 &&  theta_C>20 && theta_C<34
&& theta_A<70 && theta_A>56
&& ((phi_C>0 && phi_C<25) || (phi_C>335 && phi_C<365))
&& phi_A>170 && phi_A<190 && multA==1 && multC==1
&& e12new>18  && nA_y>3 && nA_y<11 && nC_y>3
&& nC_y<11 && abs(ps)<50");
eexp->Sumw2();
esim->Sumw2();
TH1F *ediv=new TH1F ("ediv","ediv",20,-0.099,2.2);
ediv->Divide(eexp,esim);
ediv->Draw("e1");
```

Bibliography

[1] C.A. Bertulani *et al.* Progg. in Part. Nuc. Phys. **89**, 101016 (2016).

[2] A. Coc *et al.* Ap. J **600**, 380121 (2004).

[3] D.N. Schramm *et al.* Rev. of Mod. Phys. **70**, 70303 (1998).

[4] B.D. Fields *et al.* Ann. Rev. of Nuc. Part. Sci. **61**, 47-68, 130445 (2011).

[5] R.H. Cyburt *et al.* Phys. Lett. sec. B **567**, 101016 (2003).

[6] K.A. Olive *et al.* M.N.R.Astrop.Soc. **426**, 21703 (2012).

[7] S.G. Ryan *et al.* Ap. J. **523**, 307769 (1999).

[8] R.H. Cyburt*et al.* J.C.A.P **12**, 101088 (2008).

[9] A. Coc *et al.* Phys. Rev. D **87**, 123530 (2013).

[10] L. Sbordone *et al.* A & A **522**, 26, 200913282 (2010).

[11] A.D. Leva *et al.* Phys. Rev. Lett. **102**, 232502 (2009).

[12] A. Kontos *et al.* Phys. Rev. C **87**, 065804 (2013).

[13] P. E. Koehler *et al.* Phys. Rev. C **37**, 37917 (1988).

[14] A. Hemmendinger *et al* R. Taschek. Phys. Rev. **74**, 101103 (1948).

[15] K.K. Sekharan *et al.* N.I.M **133**, 90617 (1976).

[16] P. Descouvemont *et al* A. Adahchour. J.Phys **29**, 101088 (2003).

[17] P. Bassi *et al.* Il Nuovo Cimento (1955-1965) **28**, 1049–1065, 02782032 (1963).

[18] C. H. King *et al.* Phys. Rev. C **16**, 161712 (1977).

[19] D.J. Mercer *et al.* Phys. Rev. C **55**, 55946 (1997).

[20] L. Canton *et al* C. Broggini. J.Cosm.Ap.Phys **6**, 2012.

[21] P.D. Serpico *et al.* J.C.A.P **10**, 203-282, 101088 (2004).

[22] C.A. Bertulani *et al.* Ap. J. **767**, 2013.

[23] C. Iliadis. "Nuclear Physics of Stars", 672, Wiley-VCH, Chapel Hill (U.S.A.), 2015.

[24] K.S. Krane. "Introductory nuclear physics", 845, Wiley, New York, 1988.

[25] S. Burles *et al*. Phys. Rev. D **61**, 123505 (2000).

[26] M. Kawasaki M. Fukugita. Ap. J. **646**, 505109 (2006).

[27] D. Pierroutsakou *et al*. Nuc. Hab. **63**, 2018.

[28] J. Pradler *et al* M. Pospelov. Ann. Rev. of Nuc. Part. Sci. **60**, 104521 (2010).

[29] A. Coc *et al*. Int. J. Mod. Phys **26**, 1741002 (2017).

[30] K.A. Olive *et al*. Ap. J. **617**, 425170 (2004).

[31] A. Coc *et al* C. Pitrou. Phys. Rep. **754**, 1-66, 2018.

[32] R.W. Wilson A.A. Penzias. Ap. J **142**, 419-421, 148307 (1965).

[33] D.J. Fixsen *et al*. Ap. J. **707**, 7072916 (2009).

[34] D.J. Fixsen *et al*. Ap. J. **420**, 1994.

[35] J. Dunkley *et al*. Ap. J **180**, 101088 (2009).

[36] L. Page *et al*. Ap. J. **148**, 377224 (2003).

[37] R.H. Cyburt *et al*. Astropart. Phys. **23**, 2004.

[38] J.D. Barrow *et al*. Phys. Rev. D **98**, 043534 (2018).

[39] X. Fu *et al*. M.N.R.Astrop.Soc **452**, 1077002 (2015).

[40] A.M. Boesgaard *et al*. Ap. J. **633**, 444607 (2005).

[41] P. Bonifacio *et al*. A & A **462**, 20064834 (2007).

[42] M. Spite F. Spite. A & A **115**, 357-366, 1982.

[43] T. Nordlander *et al*. Mem. S.A.It. Suppl **22**, 110, 2012.

[44] S.Q. Hou *et al*. Ap. J. **834**, 103847 (2017).

[45] D. Bemmerer *et al*. Phys. Rev. Lett. **97**, 122502 (2006).

[46] A. Di Leva *et al*. Phys. Rev. Lett. **103**, 159903 (2009).

[47] C. Angulo *et al*. Ap. J **630**, 491732 (2005).

[48] S. Q. Hou *et al*. *Phys. Rev. C **91**, 055802 (2015).*

[49] M.Barbagallo *et al*. Phys. Rev. Lett. **117**, 152701 (2016).

[50] T. Kawabata *et al*. Phys. Rev. Lett. **118**, 052701 (2017).

[51] C. A. Bertulani *et al* L. Lamia, C. Spitaleri. Ap. J **850**, 175, 103847 (2017).

[52] C.E. Rolfs and W.S. Rodney. "Cauldrons in the cosmos : Nuclear astrophysics", 561, University of Chicago Press, 1988.

[53] W.R. Leo. "Techniques for Nuclear and Particle Physics Experiments", 1-15, Springer Berlin Heidelberg, Berlin, 1994.

[54] G. R. Satchler. "Introduction to Nuclear reactions", 316, Macmillan Press, 1980.

[55] H.J. Assenbaum *et al*. Z.Phys. **327**, 01289572 (1987).

[56] R.G. Pizzone *et al*. Nuc. Phys. A **834**, 2010.

[57] A.M. Mukhamedzhanov *et al*. 2nd Int. Conf. Nuc. Phys. Ap. **540**, 32843 (2006).

[58] M. La Cognata *et al* R.E. Tribble, C.A. Bertulani. Rep. Prog. Phys. **77**, 106901 (2014).

[59] D.Y. Pang *et al*. Phys. Rev. C **90**, 044611 (2014).

[60] G. Baur *et al*. Nuc. Phys. A **458**, 90290 (1986).

[61] C. Spitaleri *et al*. Phys. Rev. C **60**, 0558002 (1999).

[62] A. Tumino *et al* C. Spitaleri, L. Lamia. Phys. Rev. C **69**, 055806 (2004).

[63] G.F. Chew *et al*. *Phys. Rev.* ***85****, 85636 (1952).*

[64] A.K. Jain *et al*. Nuc. Phys. A **142**, 905336 (1970).

[65] P.G. Roos *et al*. Nuc. Phys. A **257**, 906357 (1976).

[66] N.S. Chant *et al*. Phys. Rev. C **15**, 1977.

[67] C. Spitaleri *et al* A. Tumino. Phys. Rev. C **67**, 065803 (2003).

[68] M. Zadro *et al*. Phys. Rev. C **40**, 181, 101103 (1989).

[69] I. Indelicato *et al*. Ap. J. **845**, 103847 (2017).

[70] R.G. Pizzone *et al*. Eur. Phys. J. A **52**, 24, 101140 (2016).

[71] S. Romano *et al*. AIP.C.P **1120**, 13141665 (2009).

[72] A. Caruso *et al*. AIP.C.P. **1645**, 14909591 (2015).

[73] G.L. Guardo *et al*. Phys. Rev. C **95**, 025807 (2017).

[74] A. Oliva *et al*. Nuovo Cimento C Soc. It. Fis. **43**, 201117 (2020).

[75] M. Mazzocco *et al*. EPJ W.S **184**, 01012 (2018).

[76] M. Mazzocco *et al*. N.I.M sec. B **317**, 223-226, 101016 (2013).

[77] R. Bevilacqua *et al*. N.I.M. sec. A **770**, 64-67, 10.1016 (2015).

[78] D. Pierroutsakou *et al*. N.I.M sec A **834**, 2016.

[79] ROOT: analyzing petabytes of data, scientifically, https://root.cern/.

[80] L. Lamia and M. Mazzocco *et al*. Ap. J **879**, 23 (2019).

[81] LISE++ : Rare Isotope Beam Production, http://lise.nscl.msu.edu/lise.html.

[82] S. Romano *et al* E. Costanzo, M. Lattuada. N.I.M sec. A **295**, 373-376, 90715 (1990).

[83] E. Purcell C. G. Sheu H. R. Weller *et al* J. H. Kelley, J. E. Kwan. Nucl. Phys. A **880**, 101016 (2012).

[84] C. Spitaleri *et al*. Phys. At. Nucl. **74**, 1725-1739, 10.1134 (2011).

[85] Wolfram Mathematica: Modern Technical Computing, https://www.wolfram.com/mathematica/.

[86] S. Hayakawa, M. La Cognata, and L. Lamia *et al*. JPS Conf. Proc. **31**, 011036 (2020).

[87] A. Goudelis *et al*. Phys. Rev. Lett. **116**, 211303 (2016).

[88] M. Barbagallo *et al* L.Damone. Phys. Rev. Lett. **121**, 042701 (2018).

[89] SPES Project INFN-LNL, https://web.infn.it/spes/.

List of Figures

Acknowledgments

Thank you!

Hello to everybody reading this section of thanks. After reaching this personal goal, it is right and proper to thank all those who have supported and put up with me during these five years. This moment has a lot of meaning for me. A beautiful cycle of my life has come to an end. In the past five years I have met wonderful people, experienced a sea of emotions and I always had extreme support from my family and friends. In just a few days, however, a new chapter will open. My departure for Paris and the knowledge that I will be away for a long time from my family makes this moment even more special. What I feel is a mixture of euphoria and happiness for what's going to happen but also sadness for what today has come to an end. That's why these thanks are very hard to do without getting emotional and thinking back to all the good things that have happened to me.

The first I would like to thank with all my heart are my supervisor and co-supervisor Marco Mazzocco and Livio Lamia. Marco, we have known each other for five years now, what good memories the tennis match at the end of my first year of the Bachelor's degree, the talks about soccer, the Federer Nadal match at Wimbledon 2019 watched during the Bachelor's thesis period and many other moments. Thank you for always supporting me, believing in me and being there for me during these five years. Thank you for following me with passion and dedication during this thesis work. I know that it has been a challenge for you to help me and support me as much as possible during this period, but in the end you did miracles by following me well during this project. Marco, you are truly an honest, sincere and genuine person, thank you very much for everything. A big thanks also to my co-supervisor Livio. First of all, I would like to apologise again for all the heart attacks I have caused you during this period. I know it has been a challenge to get to the end of this work without losing our mental health. Your help has been of fundamental importance, you have patiently guided me step by step through this thesis and I will never forget the many moments of work and fun spent on video calls. Marco and Livio, this period has been "eccezzziunale... veramente" and I look forward to seeing you both in Paris!

A big thanks to my parents Daniela and Alberto and thanks to my sister Anna and brother Davide. As I wrote at the beginning, this moment is extremely emotional for me and I am sure it is for you too. To get to this point, we went through very anxious and stressful moments but thanks to our union and strength we have always managed to overcome all the obstacles. In a few days I leave. I know that thanks to all the things you have taught me I will be able to face future challenges without fear, and this gives me happiness and hope for the future. Thank you Mum and Dad for your patience and above all for your understanding. I have not always been very present in the family because of my studies and I can only thank you for allowing me to follow the path I wanted, to realise my dreams

and for the love you always show me every day. Thank you for giving me the strength to never give up. Thank you Anna and Davide for always pushing me to give my best, for supporting me in every moment and decision. You are my greatest source of inspiration, I love you so much.

I would like to thanks my grandparents Pina e Angelo, my uncles Luisa, Giuseppe, my cousins Matteo e Nicola for advising me wisely, for supporting me in my choices and for being there for me throughout these five years. This achievement is also thanks to you.

Isabella, Alessandro, Corrado and Lorenzo you are like a second family to me. In these four and a half years, we have shared emotions, joys and even some sadness. I will never forget all the games of Uno, Munchkin, Mario Kart, all the Spritz and the crepes of "La Romana" eaten together, all the cakes made by Isabella. But above all, I will never forget your kindness and positivity. Being with you for all these years has made me a better person and I am really grateful for that. Thank you!

A special thanks to all my friends that accompained me during these wonderful five years. Thank you for supporting me and to have made these five years unforgettable. Even though we have not been able to see each other as much as we would have liked over the last two years you have always managed to make me feel your closeness. The hours spent in the laboratory developing programs and attaching cables, the breakfasts and snacks at "Soranzo", the lunches on the stairs of Paolotti, all the hot chocolates and Ice creams are examples of just a few of the many moments I will always carry with me. Thanks to all of you!

Thanks to all those who love me.

Yours,
Andrea Lagni

"Let everything happen to you
Beauty and terror
Just keep going
No feeling is final"

Rainer Maria Rilke